CFD Study of a Large Buried Tank within a Borehole Field

CFD STUDY OF A LARGE BURIED TANK WITHIN A BOREHOLE FIELD

BY

PARATHY KANDIAH, B.Eng.

A THESIS

SUBMITTED TO THE DEPARTMENT OF MECHANICAL ENGINEERING

AND THE SCHOOL OF GRADUATE STUDIES

OF MCMASTER UNIVERSITY

IN PARTIAL FULFILMENT OF THE REQUIREMENTS

FOR THE DEGREE OF

MASTER OF APPLIED SCIENCE

Master of Applied Science (2014) McMaster University

(Mechanical Engineering) Hamilton, Ontario, Canada

TITLE:	CFD Study of a Large Buried Tank within a Borehole Field
AUTHOR:	Parathy Kandiah B. Eng., (Mechanical Engineering) McMaster University, Hamilton, Canada
SUPERVISOR:	Dr. Lightstone
NUMBER OF PAGES:	xxvii, 192

Abstract

This work explores the impact of burying a short term thermal storage (STTS) tank within a borehole thermal energy storage (BTES, or borehole field). There is motivation to bury tanks in order to save space on ground level, as well as to improve the overall efficiency of the system by reducing heat losses from the tank. This work mainly looks to understand the impact of the lack of boreholes under the buried tank, as well as the thermal interactions between the tank and boreholes.

Computational Fluid Dynamics was used to predict the transient temperature throughout the domain. The long-term performance was assessed by simulation a five year period. Examination of factors that influence the tank-borehole interactions was studied and it was determined that radial stratification of the borehole field as well as the soil properties have the largest influence in terms of increasing the efficiency of the BTES. Other factors, such as tank stratification and tank insulation have little impact and the remainder (tank aspect ratio, and alternate geometries) have some impact.

Acknowledgements

I would like to thank Dr. Marilyn Lightstone for her supervision and guidance throughout this research. I have been very fortunate to have had her as my supervisor as her help as been invaluable.

My thanks also go to Dr. Michel Bernier, of École Polytechnique de Montréal, and Dr. Marc Rosen, of the University of Ontario Institute of Technology (UOIT), for their helpful insight for borehole modelling, as well as Mr. Bruce Sibbitt, of Natural Resources Canada, for providing data of the Drake Landing Solar Community project.

The Smart Net-Zero Energy Buildings Strategic Research Network (SNEBRN) and Natural Sciences and Engineering Research Council (NSERC) are acknowledged for their financial support as well as ANSYS-CFX for providing the software code.

I would also like to thank my colleagues for their help, patience, and advice for getting my computer to obey my whims. Thank you to my friends for sticking with me, even as I brought my research into any and all conversations. My apologies to those who now feel entitled to a credit in heat transfer.

Finally, I thank my family, in particular my mother and brother, for all of their love and support, without which I most certainly would not have finished this work.

Notation and Abbreviations

Nomenclature

A	Area, m^2
C_p	Specific heat capacity, kJ/kg·K
d	Diameter, m or mm
E	Energy, GJ or MJ
h	Height, m
h	Heat transfer coefficient, W/m2·K
k	Thermal conductivity, W/m·K
L	Length, m
M	Mass, kg
$\dot{m}$	Mass flow rate, kg/s
q”	Heat flux, W/m^2
$\dot{Q}$	Heat transfer rate
r	Radius, m or mm
r^*	Non-dimensional radius
R	Thermal resistance

T	Temperature, K or °C
t	Time, s, hr, day
t_c	Characteristic time, day
$\dot{V}$	Volumetric flow rate, l/s
v	Velocity, m/s
x, y, z	Cartesian coordinates
x^*	Non-dimensional length

Greek Symbols

α	Thermal diffusivity, m^2/day
η	Efficiency
θ	Non-dimensional temperature
μ	Dynamic Viscosity, kg/m·s
ρ	Density, kg/m^3

Subscripts

air	Property for air
bh	Borehole
charge	Charging
cold	Cold surface
discharge	Discharging
eff	Effective
extracted	Energy extracted
hot	Hot surface
i or initial	Initial value
injected	Energy injected
L	Length
s	Surface
total	Total value

Dimensionless Groups

Nu	Nusselt number, hL/k
Re	Reynolds number, ρ vL/μ

Abbreviations

ATES	Aquifer Thermal Energy Storage
BTES	Borehole Thermal Energy Storage
CFD	Computational Fluid Dynamics
CHS	Cylindrical Heat Source
COP	Coefficient of Performance
DLSC	Drake Landing Solar Community
FLS	Finite Line Source
HDPE	High Density Polyethylene
ILS	Infinite Line Source
PVC	Polyvinyl chloride
STS	Seasonal Thermal Storage
STTS	Short Term Thermal Storage
TES	Thermal Energy Storage
TIL	Thermal Insulated Leg
XPS	Extruded Polystyrene

Contents

List of Tables

List of Figures

Chapter 1

Introduction and Problem Statement

In a cold climate, such as that in Canada, much of the energy use of an average home goes towards heating. Currently in Toronto heating accounts for 63% of the average energy use in a typical Canadian home [1]. This means even small improvements in the systems and technologies used can have a significant impact on the overall energy use.

Meanwhile, solar radiation on earth is 84 TW/day, compared to the global power need of 12 TW/day, which indicates that some of this energy could be used for heating purposes [2]. As shown in Figure 1.1, there is a mismatch between when the solar radiation is available, and when the heating demand is required.

One method to better utilize the available solar energy is by means of seasonal storage, which would store the excess energy from the summer to be used in the winter months when the heating load peaks. In order for seasonal storage to be more efficient, it can be performed at the community level. These communities see higher

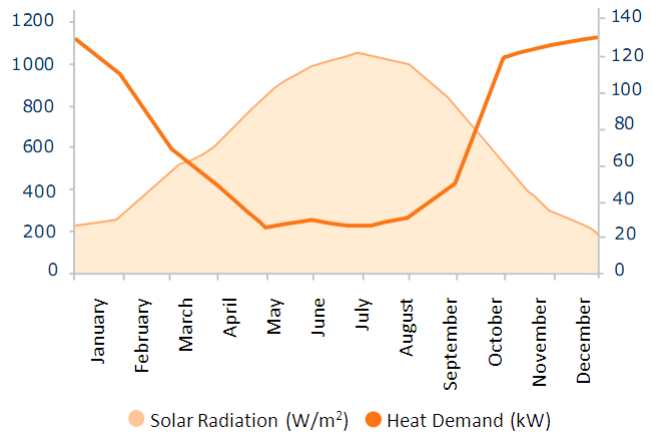

Figure 1.1: Mismatch of solar energy supply and demand [3]

efficiencies and therefore greater savings due to economies of scale [4]. One such community is Drake Landing Solar Community (DLSC), which is located in Okotoks, Alberta. The community of 52 houses was built in 2007, and has reached a solar fraction (percent of heating energy supplied by solar) of 96.7% [5].

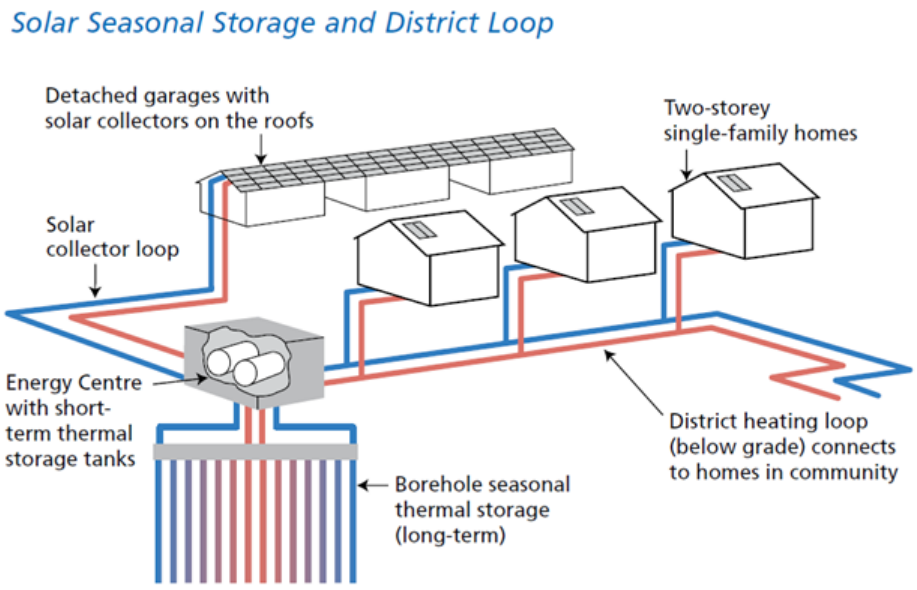

Figure 1.2: Schematic of Drake Landing Solar Community [5]

The system at DLSC consists of three major components and is shown schematically in Figure 1.2. The three components are the solar collectors, which are mounted onto the roofs of the detached garages, two Short Term Thermal Storage (STTS) tanks, and a Borehole Thermal Energy Storage (BTES), otherwise referred to as a borehole field.

The solar collectors are solar-thermal units and operate without the need for a heat pump. This study, which is motivated by DLSC, will focus on inputs from a solar thermal system.

The two STTS tanks have a volume of 120 m^3 each, which is roughly the size of a railway car. They are currently housed in the energy centre, and occupy about 70% of the floor space.

The borehole field consists of 144 boreholes, which are 150 mm in diameter and 35 m deep. These are plumbed with six boreholes in series, called strings, and the entire field is made up of 24 of these strings, which can be seen in Figure 1.3. The efficiency of the borehole field, defined as the energy extracted divided by the energy injected, is 20% in the first year of operation, because the ground needs to be heated from the uncharged conditions [5]. Subsequent years see efficiencies that vary between 35-54% [5].

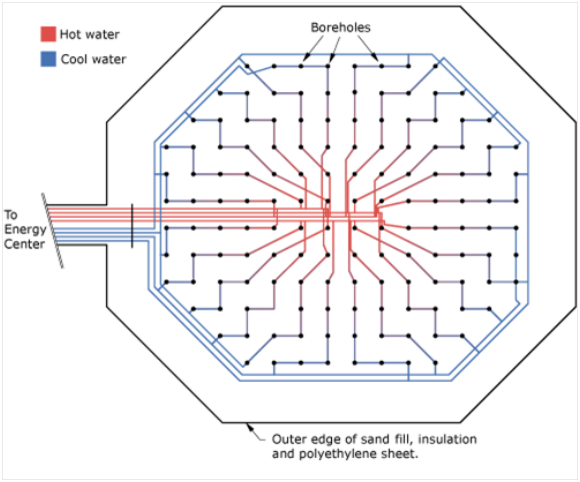

Figure 1.3: Top view of borehole field at Drake Landing Solar Community [5]

The STTS tanks act as a buffer between the solar collector loop, the space heating loop and the borehole field. They are required because the heat transfer rate to the borehole field is much smaller than the rate at which the collector loop gains energy. Based on the volume and flow rates entering the STTS tanks, it is determined that the tank turnover time is around six hours, whereas it takes a full 24 hours to transfer this energy to the borehole field. Without the buffer tanks, the fluid would not be able to exchange heat quickly enough with the ground, and would result in hotter fluid returning to the collectors, which would reduce collector efficiency.

Due to the STTS tanks' sizeable footprint, there is an interest in exploring the implications of burying the tank within the borehole field. A buried STTS tank would allow for additional recreational park space for community use.

This thesis will use computation fluid dynamics to study the impact of a large buried tank within a borehole field. More specifically, the interactions between the tank and boreholes, as well as the lack of boreholes under the tank will be investigated in detail. The geometry and boundary conditions for the borehole field will be similar

to that at DLSC.

The following chapters will focus on certain key aspects found in this research. Chapter 2 is the literature review, which will cover large tanks, the means for seasonal storage (including, but not limited to, borehole fields), control strategies and design considerations, and borehole modelling techniques. Chapter 3 will focus on simple verifications required to carry out current work. This includes tests for steady state and transient heat transfer with a known analytical solution, the effect of borehole, tank and domain shape, the principle of superposition, and verification of borehole modelling against existing literature. Chapter 4 will outline the modelling and methodology (meshing, initial and boundary conditions, soil properties, etc) used for the Base Case. Chapter 5 will present different conditions that influence the tank and boreholes' performance such as geometry, number of rings, radial and tank stratification, tank insulation and aspect ratio and soil type. This chapter also includes an analysis of the results. Finally, chapter 6 will present the conclusions as well as recommendations for future work.

Chapter 2

Literature Review

2.1 Introduction

This literature review provides a summary of existing work that pertains to the modelling of a large buried tank in a borehole field. Various types of borehole tubes, tank geometries, and layouts are reviewed. Additionally, other factors that are important to the thermal performance of large buried tanks are presented: heat, air and moisture transfer, insulation, stratification, control systems and alternative methods of placing tubes. Existing mathematical modelling techniques are also discussed.

2.2 Problem

Solar radiation is an abundant source of energy, but there is a mismatch of high demand in the winter for heating purposes and the low demand for heat in the summer months, whereas the incident solar radiation reaches its peak during the summer and plunges in the winter. It would be useful to collect energy in the summer to use for

heating in the winter by employing seasonal storage of solar energy [6]. These systems have been proven to reduce CO_2 emission significantly [7].

2.3 Methods for Seasonal Storage

Seasonal storage is used to store excess heat/energy in the summer for use in the winter. This is done by storing heat within large volumes of water, soil, gravel, or some combination of the above.

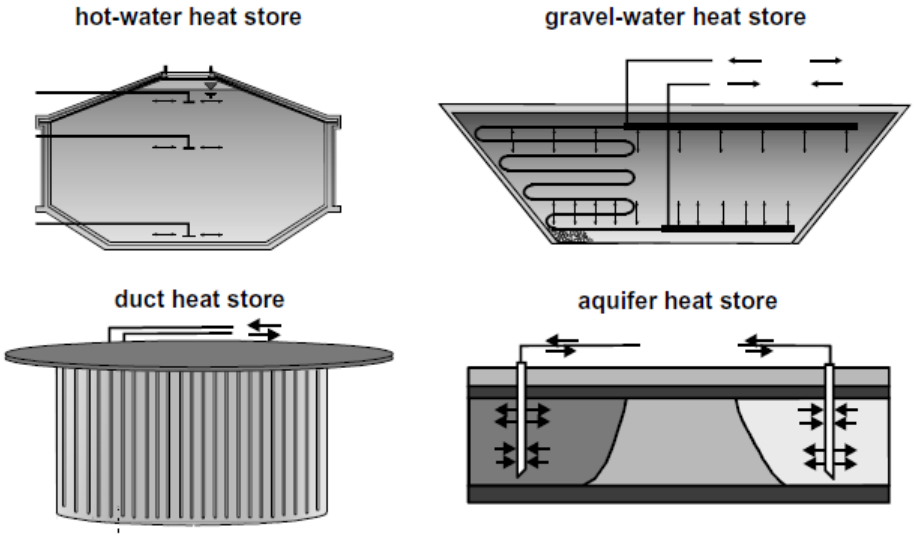

Figure 2.1: Types of Storage [8]

There are four main methods of seasonal storage: hot water, duct (Borehole Thermal Energy Storage or BTES), gravel combined with water and Aquifer Thermal Energy Storage (ATES). While this study will focus on large tank storage and borehole energy fields, an overview of all types is presented below.

2.3.1 Water Based Systems

Hot water heat storage is "the most favourable of the four storage types from the thermodynamic point of view," [8] due to the high heat capacity of water. The tank is usually built out of concrete and can be buried or placed on ground level. It is usually insulated on the top and sides, and sometimes the bottom as well. Often there is a liner inside the tank to prevent moisture transport [8]. They can vary in the range of 100 to 10,000 m^3. These tanks are often used for large buildings or communities to benefit from economies of scale. A compilation of data on existing large tanks is provided in Appendix A.

Insulation

Insulation is used to prevent heat loss from the tank to the surrounding environment. Insulation must be suitable for the proposed application (weather resistant, durable, etc.) [9].

Heat is lost due to lack of insulation at the bottom of the tank, moisture penetration and any changes to material properties (i.e. moisture penetration into the insulation, ground water flow). Insulation must also be able to withstand the damage that may occur during installation and care must be taken to keep the insulation dry. There is also contamination from rain water and construction debris, etc that should be considered. Often, bulk materials are used because they can be blown in relatively quickly. This reduces the potential for damage from water penetration and is more economical [9].

Different bulk materials are used to insulate the tanks. Ochs et al, 2007 have studied thermal conductivity versus moisture penetration. Bulk materials tend to

be porous and can degrade due to water penetration. Inorganic materials are used because organic material is unable to withstand the pressure at the required temperatures [9]. In this study, insulation on the tank is not a major concern because the heat lost from the tank will be gained by the boreholes [10].

Philip and De Vries attempted to study moisture movement by means of case studies, but found that often the boundary conditions were too complex to obtain a simple mathematical model. They also concluded that moisture transfer is negligible in either very wet or very dry materials, and is only of concern under semi-saturated conditions [11].

Stratification

Thermal stratification, the vertical layering of fluid by temperature, is often desirable in tanks to improve the efficiency of the overall system. Stratification enhances the performance of the system because cooler fluid will be supplied to the collector and as a result, the collector efficiency will increase since there will be less heat lost to the environment. An additional benefit of stratification is that the hottest fluid will be at the top of the tank, which results in higher temperature fluid being provided to the user, thus reducing the heat for auxiliary heating [12].

Alternatively, Rezaie et al presented an interesting conclusion, which was that stratification does not improve efficiency very much in a large seasonal storage tank, such as the one at Friedrichshafen. This is due to the fact that there is a relatively small temperature difference (11.5°C on average), which in turn means that the "cold" water at the bottom of the tank is not much different from the fully mixed water temperature [13]. Overall, it was recommended that stratification does not

need to be modelled for a large buried tank with little stratification due to small temperature differences, as the exergy analysis does not show significant improvement for the added degree of complexity for their operating conditions [13]. However, the problem encountered at DLSC should have stratification modelled as the temperature difference across the collectors is around 20°C and there are multiple loops running simultaneously.

Tank Case Studies

Schmidt and Mangold provided a case study of a large seasonal thermal energy storage that was built in 1996. The storage is a large buried concrete tank that was initially charged by solar collectors. The original system was running significantly under the expected designed efficiency (46% actual compared to 89% design), which was due to higher than anticipated thermal losses, groundwater penetration in the insulation (and lack of material properties for wet insulation) and a damaged roof (top of the tank). Some reconstruction was done and an additional layer of insulation was added in order to improve the efficiency before it was connected to a waste heat recovery system in addition to the solar collectors in order to help balance the load better [14].

In order to make tanks for single family dwellings, modifications are sometimes made to the manufacturing process. The tank studied by Steinweg et al is a small experimental tank for a single family home with volume 5.5 m^3 buried next to the house. It is made of concrete and is being buried due to space constraints and difficulties replacing tanks in basements with small doorways and halls. This tank needs to be pre-constructed in order to reduce the cost, as compared to large seasonal storage tanks that are constructed at the location they will be installed at. The

insulation is put on the inside of the tank to reduce possible damages during transport, as opposed to insulating the exterior of the tank on location as for larger tanks. Temperature and moisture sensors were installed to monitor progress and ensure the tank performs as expected. The temperature readings from these sensors show signs of stratification after five hours of idle time [15].

2.3.2 Ground Based Systems or Borehole Thermal Energy Storage

BTES systems consist of multiple PVC pipes buried in the ground, with a water-glycol mixture pumped through them. These pipes act as heat exchangers with the ground, injecting heat in the summer and extracting it in the winter [6]. It is also important to ensure the properties of soil (ρ, k, C_p) used to design the system are representative of the local soil conditions. There is often a layer of insulation at the surface of the borehole field to reduce the heat loss to the ambient [8]. The PVC pipes are typically arranged in some sort of grid pattern. It is recommended to apply a spacing of at least 15 feet (4.6 m) between non-interacting boreholes to minimize thermal interaction. Underestimating the interaction between the tubes or the tubes and tank can result in a slow drift of the ground temperature if there is a heat imbalance in the amount of heat generated compared to the heat needed and used [16].

It is essential that the temperatures at the outer edge and centre of the borehole field are measured in order to determine when to add heat to the system and when it is possible to extract it [6]. It is important that the amount of heat extracted in the winter balance the amount of heat injected in the summer, otherwise the ground will experience a temperature drift and will not result in the necessary steady state

behaviour [17].

Often, the system uses a backup boiler to supply additional heating if BTES cannot meet demand. BTES systems are best used for seasonal energy storage, in small scale applications. The advantage to the system is that is can be used for direct heating and cooling [18]. For systems requiring heat pumps, an auxiliary heater is almost always needed in order to meet the temperature requirement, whereas a BTES system often can reach the required temperature without the use of auxiliary heating, which leads to higher efficiencies.

As the borehole field increases in size, the surface area to volume ratio decreases, which leads to reduced heat losses to the surrounding soil and consequently, higher efficiencies. It is also important to note that radial stratification helps to reduce heat losses. During charging, the hot fluid is run from the centre of the field outwards, and during discharging, the direction is reversed, ensuring the coldest part of the borehole field is on the outer edge. Because the outer edge has the coldest temperature, the heat losses to the surrounding soil (10°C) is minimized, thereby ensuring maximum efficiency.

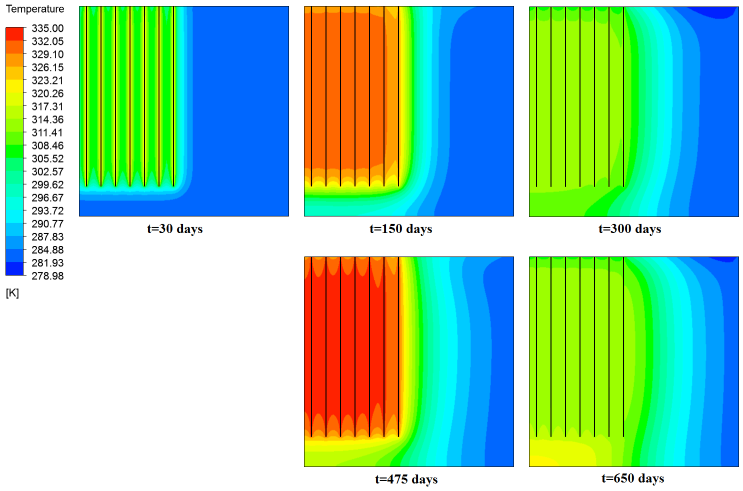

Figure 2.2: Side view of temperature contour plots of a typical borehole field

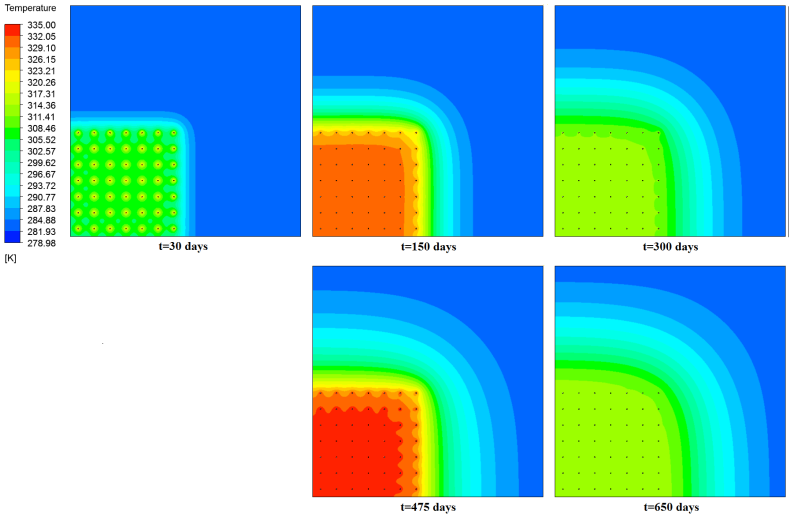

Figure 2.3: Top view of temperature contour plots of a typical borehole field

Figures 2.2 and 2.3 show temperature contour plots of a typical borehole field. The side view contour is taken through a plane containing boreholes, and the top view contour is at the borehole half length. The losses from a borehole field occur at the outer edges of the field. As can be seen in the figures, after the first charging cycle, there is some heat injected to the ground outside the borehole area. When the

field is discharged, this energy is not regained. During the second charging cycle, it can be observed that more heat has spread to the area away from the boreholes.

Tube Depth & Orientation

For heat pump applications, the length of borehole required for heating in the winter will be different from the length required for cooling in the summer. This results in the system being over or undersized depending on the season. Generally, the shorter of the two lengths is chosen for economical reasons, but in some cases the longer is taken so that an additional heating/cooling system does not needed to be installed and the COP can be increased [19].

Horizontal vs Vertical Boreholes

Horizontal boreholes are 35-60 m long per kW of load and can be arranged in parallel lines, coils, or trenches placed about 1-2 m below ground. They have the advantage of being more cost effective than vertical boreholes, but they require a larger area for installation. They are mainly recharged by solar radiation falling on the ground, so there is less concern about temperature drifts, but there is also the potential for higher heat losses. If there is a significant amount of hard rock near the surface, it is difficult or impossible to install these systems [20].

Vertical boreholes are approximately 30-100 m deep [8] and the fluid exchanges heat with the ground as it runs through the tubes. These systems can be installed over smaller areas and rocky soil. Vertical boreholes are usually shorter than horizontal as the earth that deep tends to remain cooler in the summer and hotter in the winter. The deeper earth does not see the temperature fluctuations at the surface,

thus making vertical boreholes more efficient [20]. The current research only considers vertical tubes.

Tube Types

Various geometries for the tubes are available and are shown in Figures 2.4a and 2.5. The boreholes have a typical outer diameter of 4-6 inches, with the PVC tubes inside being roughly 1 inch in diameter. The space between the PVC pipes is filled in with grout which acts to stabilize and centre the pipes correctly.

U-tubes: These are the tubes used at DLSC [6]. There is heat transferred between the upward and downward flow, and exergy is lost [21]. U-tubes can be in single or double configurations, which can be viewed in Figure 2.4a. Often, a thermal resistance diagram like the one in Figure 2.4b is used to determine the outer borehole wall temperature. U-tubes are manufactured as long continuous coils of tubing that are then inserted into the borehole, which is the simplest installation of the tubes types discussed in this section.

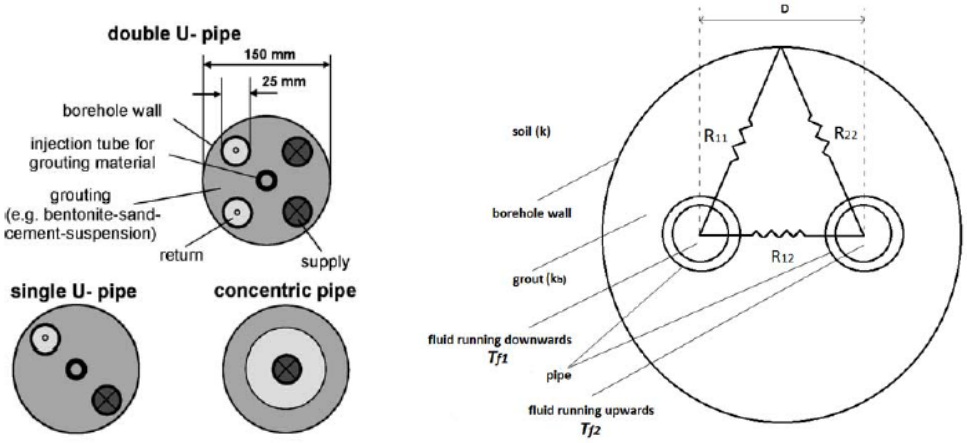

(a) Cross sections of different tube types [8]

(b) Thermal Resistance Diagram of the Interior of a U-tube Borehole [22]

Figure 2.4: U-tube diagrams

Thermal Insulated Leg (TIL): This tube consists of a center pipe that is insulated, and the four outer pipes are not and can be seen in Figure 2.5. This reduces the rate of heat transfer between the legs and can improve thermal performance by factor of 2. The drawback to using these types of tubes is that there is a higher cost than single or double U-tubes [21].

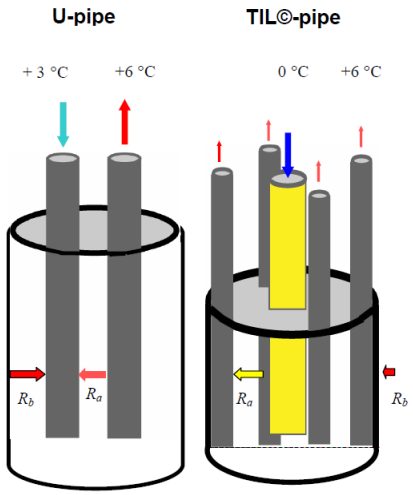

Figure 2.5: U-Tube and TIL Tube [21]

Concentric: Concentric tubes consist of an inner pipe for the fluid to enter, and the outer cylinder for it to exit, as seen in Figure 2.6. These tubes are more efficient than single or double U-tubes. Cruickshanks et al discussed an attempt to seal the concentric tubes with bentonite (clay mineral) and the results showed significant improvement [23]. In general, the concentric tubes have a higher efficiency due to the fact that the liquid is running in direct contact with the outer wall. This means that water can be used without anti-freeze and the length of borehole can be reduced. Concentric tubes are manufactured in lengths of 10 feet (ref!), and need to be connected together on site. They need very good sealing between the connections in order to prevent leaks, which makes them more expensive. It is also difficult to center the inner tubes [23].

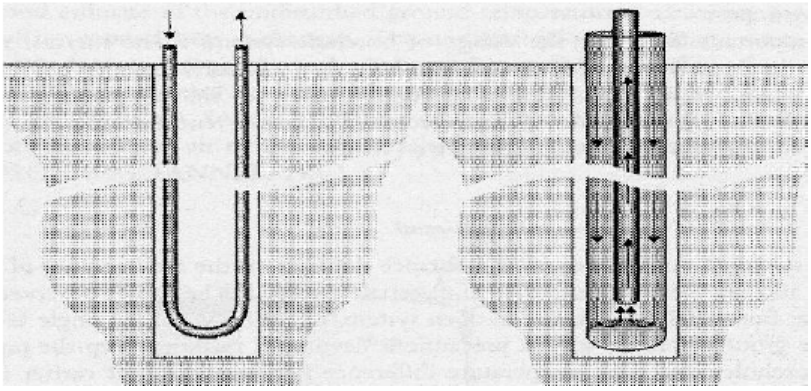

Figure 2.6: U-Tube and Coaxial [23]

Case Studies or Placement of Tubes in Foundation Walls

Research has been performed in Germany on the use of the ground around the foundation walls as a heat exchanger for the geothermal heating system. There are ten buildings which are being studied for operation, energy performance and ground temperatures [17]. Unfortunately, there is occasionally stationary fluid in the pipes, which then gain heat. This reduces efficiency because the fluid then needs to be pumped through the loop again before it can be used.

Tubes are also put in foundations in Japan, due to the fact that drilling long tubes would not result in economical savings over the lifetime of the pipes due to lower energy prices. The system of placing tubes within building foundations is called an energy pile system. The tubes are 27-34 mm in diameter, while the foundation walls are 1500-4000 mm, so the tubes do not compromise structural integrity [24]. This is one possibility for installing vertical boreholes where space is at a premium.

2.3.3 Other Methods for Seasonal Storage

Aquifer Thermal Energy Storage (ATES)

ATES are built using existing water-bearing soil. In order to use an aquifer for a heat store, there needs to be little to no groundwater flow. Heat is injected and extracted from the aquifer by means of pairs of water wells. On one end of the aquifer, there is one or more hot wells, and on the other, one or more cold wells. In the summertime, water is extracted from the cold well(s), heated up through some solar collectors, and injected in the hot well(s). In the wintertime, this process is reversed in order to regain the heat. The main drawback to ATES is that there needs to be an existing suitable aquifer on site [8].

Gravel Based Systems

Another means for seasonal storage can be implemented by means of a gravel-water store. Water-gravel systems often consist of a large lined pit. Heat is injected and extracted either by means of directly exchanging water, or through the installation of pipes, which act as a heat exchanger. Due to the presence of gravel, there is no need to build load bearing walls. However, the drawback to using a gravel-water store is that they need to be up to 50% larger than a water only store [8] in order to store the same capacity of heat since gravel has a lower specific heat than water.

2.4 Control System & Other Considerations

Designing a control system for BTES is complicated due to weather fluctuations. The system must make homes comfortable while still gaining enough energy to be stored

within the BTES [6].

Another factor that must be taken into consideration is the possibility of freezing. The water entering the borehole must be at a higher temperature than the freezing point and must remain that way along the length of the tube. Often, glycol is added to the water to ensure that it does not freeze. The soil near the borehole can freeze if the temperature of the water drops low enough, which has a positive effect due to latent heat. However, this effect is negligible because the area around the borehole is small compared to the overall size of the field [19].

According to Pahud et al, the BTES system temperatures should have a heating and cooling criterion. The heating criterion is to ensure that water stays above 0°C entering the boreholes to avoid freezing and the cooling criterion is met as long as the comfort of the buildings' occupants is met. When designing a borehole energy storage, often 1 year will be simulated to see if it meets the heating and cooling criterion. If it does, the simulation is continued for 50 years to ensure that performance remains at steady state. There is also importance placed on passive temperature control inside the building (external solar protections, insulation, etc) so that the BTES system has a smaller load to contend with [25].

2.5 Solar Energy Systems

Solar energy systems consist of a means to gather solar radiation, and a means to store and extract the energy. Depending on the energy supply and demand, there may be a short term storage (a few hours to a few days) or long term (seasonal), or both.

2.5.1 Drake Landing Solar Community

At Drake Landing, there are 800 flat plate solar collectors, tilted at 45°, with areas of 2.45 m by 1.18 m, which circulate a 50% water, 50% propylene glycol antifreeze. As previously mentioned in Chapter 1, the collectors are mounted on south facing garages. The water-glycol mixture circulates through the collectors, gains heat from solar radiation, and returns the fluid to the Short Term Thermal Storage (STTS) tanks.

The STTS take the the fluid and depending on demand, either send the hot fluid to heat the homes, or to storage within the borehole field. As previously mentioned, they are need to act as a buffer between the solar collectors and the borehole field due to the BTES being unable to store or extract enough heat at peak hours due to the relative time constants [6].

The borehole field consists of 144 boreholes, arranged in 24 parallel circuits with 6 boreholes each. The boreholes have a spacing of 2.25 m in a square grid pattern (ie parallel circuits do not simply extend radially). Water is pumped from the center outwards when storing heat, and in reverse when removing heat [6] in order to radially stratify the field and reduce losses to the surrounding soil. In the summer, excess heat is stored within the borehole field, and in the winter, the heat is extracted and used for space heating purposes.

2.6 Modelling Techniques

Modelling of solar energy systems can be broken down into 3 main types: system simulation methods, borehole field modelling and CFD modelling.

2.6.1 CFD Models

Computational Fluid Dynamics (CFD) uses numerical methods to solve the transient, three dimensional momentum and energy equations. Essentially, a large domain is divided up into smaller control volumes over which the governing equations are discretized. CFD numerically solves the governing equation(s) at each control volume in order to determine the overall solution for the field.

CFD models of fluid flow and heat transfer require information on the geometry of interest, material and fluid properties as well as the initial and boundary conditions. If the inputs to the CFD are not representative of the actual application, then the code predictions will not be in agreement with the physical results. For example, thermal losses from some systems have been higher than predicted [26]. This can be attributed to changes in the design when implemented, inaccurate thermal conductivities due to inaccurate moisture analysis, or inaccuracy of the modelling software, which is why it is important to select material properties, initial and boundary conditions carefully.

If the geometry, material properties, and boundary conditions are known, the CFD has the capability to provide accurate predictions of the heat transfer and temperature distribution throughout the borehole field. The computational cost can be high which may preclude the use of CFD for routine design. As such, other methods which provide approximate solutions are typically used in practice. These are discussed below.

2.6.2 Borehole Modelling-One Dimensional & Two Dimensional Codes

TRNSYS is a commonly used software package when CFD is too computationally expensive. TRNSYS simplifies borehole modelling considerably. Like most codes, it can not account for the gap in the centre of the field due to the tank as the model it uses can only generate a symmetric cylindrical storage only [27]. However, unlike most other codes, TRNSYS can account for radial stratification and is advantageous for modelling systems such as DLSC.

Ochs et al [26] studied heat and moisture transport for a large buried tank using TRNSYS. They found that the easiest way to improve the accuracy of the model is to ensure that the moisture penetration is taken into account carefully and that material used for insulation does not degrade too quickly. They also came to the conclusion that coarse models, such as TRNSYS, over-simplify the system, and as a result, it is not possible to enhance a TES using them. Essentially, there are limited improvements that can be made to such code.

Other options for modelling single boreholes include: Infinite Line Source (ILS), Cylindrical Heat Source (CHS) and Finite Line Source (FLS). These models, while simpler to use than CFD have some significant drawbacks.

ILS is a 1D model that models a borehole as a point source emitting a constant heat flux within an infinite domain at a specified initial temperature and the temperature is solved for using Fourier's Law. ILS can not account for variations along the depth of the borehole, nor can it account for a finite radius of a borehole, which means that a temperature boundary condition can not be applied. It also has problems giving accurate long term predictions because without the finite effects, the ground

temperature does not reach steady state as it should [28]. CHS is another 1D model. It does account for borehole radius by modelling the borehole as a cylindrical rod within an infinite domain. Because it has a finite radius, both a heat flux or a temperature boundary condition can be set. However, it is more complicated than ILS and does not improve the accuracy significantly. The difference between ILS and CHS at far distances or long times is approximately the same and, similarly to ILS, CHS can not give accurate long term predictions. Additionally, CHS is not as numerically stable as ILS. These factors usually result in ILS being used more frequently than CHS [29] [27].

FLS is a 2D model, which means it alone of the three can model axial variations. It consists of a constant heat flux line source with a mirrored line source with opposite sign on the other side of the ground, which is modelled as a fixed temperature surface. The two boreholes with opposite signs ensure that the ground surface does not change temperature, which would affect the rest of the ground temperature. Like the other models, the FLS assumes a uniform set initial ground temperature. Unfortunately, it involves the use of complicated double integrals, which makes it more difficult to use as well as computationally expensive [29] [27].

All three models assume a constant temperature or heat flux, but can use temporal superposition in order to handle changing loads. In order to do so, each term within the equation needs to be recalculated at each timestep, which makes it computationally expensive. Spatial superposition can also be modelled in order to calculate the thermal response of an entire borehole field [27].

2.6.3 G-Functions

G-functions are a simple means to model boreholes and are less computationally expensive than a full CFD simulation. They were first proposed by Eskilson [30], in which he combined a radial and axial simulation with spatial superposition to create the three dimensional model needed to simulate a borehole field. Ultimately, they give the temperature of the wall along the length of the borehole. G-functions are a method of determining the time response of a BTES system, which is used in some popular modelling software (EED and GLHEPRO)[27]. It gives solutions of comparable accuracy to finite line source solutions, provided that the average borehole temperature is used as the reference. The models often take a constant uniform temperature in the soil as the initial condition and a constant surface temperature. There can be some problems with using g-functions for non-uniform heat fluxes, because the heat flux will obviously vary along the length of the borehole [31].

According to Cimmino et al [32], the depth[1] to height ratio, size of the borehole field and the time the simulation is run for will impact how accurate the g-functions are. When g-functions (numerical) are compared to a finite line source (FLS) analytical solution, there is only a small difference in the small borehole fields and short simulation times, but inaccuracies on the order of 19-32% are present for deep or large fields [32]. As the ratio of distance between the boreholes to depth of the tubes increases, the solution approaches that of a single borehole since the boreholes no longer interact. It is important to note that to use a g-function, there must be a constant heat flux at any given time. These heat fluxes can then be temporally superimposed to give a solution [27]. G-functions also can not account for borehole

[1] depth of soil on top of the borehole, distance between top of borehole and ground level

thermal capacity, ie the time taken for the borehole wall to see the changes in entering fluid temperature. This is usually corrected by assuming the wall is at steady state, which takes around 3-6 hours because corrections are a bit tedious [32]. FLS assumes constant heat extraction everywhere through time, which is not true, and as such show that axial conduction is not important. Heat is extracted at center of borehole for FLS/ILS, and at the wall for g-functions.

For Eskilson's g-functions there is one value for the function along the length of the borehole. For the model proposed by Cimmino et al the temperature response is highest at the center of the borehole, and lower at the two ends. Obviously, the time taken for the borehole field to reach steady state will depend on the length of the borehole, as well as the spacing [32].

2.6.4 Other Modelling Techniques

Bouhacina et al studied the effects of the temperature difference between the two legs of the U-tube using finite element/difference methods as well as a long term time response. They came to the conclusion that the grout between the tubes is only needed to keep the tubes in place and that there is energy being stored in the grout as the water flows down the U-tube. The relatively low conductivities of soil and concrete reduce the rate of heat transfer and results in a reduced efficiency. They also mention that fouling on the inside of the U-tubes is often not taken into consideration [33].

The heat transfer between the two legs of the U-tube cannot be treated as radial conduction, as they are exchanging heat with each other, instead of directly with the ground. Beier et al conducted experiments by building a scaled down borehole field

indoors so that they could measure a more accurate temperature profile. The results showed that initially, the energy taken to heat up the grout within the boreholes was significant, but once the system reached steady state, the soil's properties became the dominant factors. They also considered what would happen to the system under a power failure. Once the system was shut down for two hours, the temperature dropped, but upon restarting, the temperature profile approached the profile of a continuous, uninterrupted charge [34]. Figure 2.7 shows the temperature profile of the interrupted test as compared to an uninterrupted control case, and it can be seen that the temperature profiles are nearly identical even after the interruption. This indicates that shut off periods for maintenance, power failures, or fluctuations in the system are not a significant concern for the temperature.

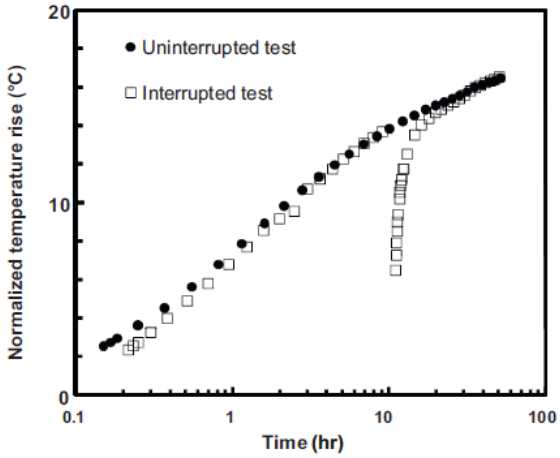

Figure 2.7: Temperature profiles of an interrupted vs uninterrupted test [34]

It has been concluded that due to the hotter fluid at the top of the borehole, the thermal interactions between them is highest at the top of the tube as well. Koohi-Fayegh and Rosen determined that superimposing the temperature increase of several boreholes together is a valid method of modelling a borehole field. This results in a

model that can be used to simulate any number of boreholes [22].

2.7 Summary

This chapter presented a survey of the literature on different configurations and factors that affect tanks and boreholes. Different tubes and geometries were considered and it was found that single U-tubes and cylindrical, vertical tanks are the most common. Heat transfer between the two legs will affect the model, as well as the properties of the concrete and soil type. Heat and moisture models are needed to ensure that the model is accurate. The depth of the borehole is dependent on the load size. G-functions have been proven to have varying accuracy depending on the conditions and assumptions used.

Currently, there has not been much work focused on buried tank-borehole interactions. Many of the existing models oversimplify the problem (use 1D approximations, run short term simulations, can not account for radial stratification). The purpose of this study is to determine the effect of a large buried tank in a borehole field by means of three dimensional, multi-year CFD simulations. Of particular interest is to assess the effect of the heat losses from the tank to the boreholes and the effect of a gap underneath the tank on the borehole field.

Chapter 3

Summary of Verification Test Cases

In order to have confidence in the CFD simulation results, verification of predictions must be performed. A suite of test cases was chosen that provided a methodical means of testing the procedure. Initial simulations were kept simple and at steady state in order to ensure that the simulations could be verified by an analytical solution. The case of a semi-infinite plate was then looked at to assess the accuracy of transient CFD simulations. Then the effects of changing the geometry of the boreholes, tanks and domains were investigated. The final simulation was transient heat extraction from a borehole, which was compared to results presented by Philippe et al [35]. Unless otherwise stated, grid independence tests consisted of doubling the number of nodes along the direction of interest and timestep independence tests consisted of halving the timesteps. The results of these tests can be found in Appendix B.

3.1 Steady State Heat Transfer through Hollow Steel Rod

The first simulation performed was steady state heat transfer through a rod, which was modelled as a wedge to reduce computational effort and can be seen in Figure 3.1. There is a flux through the inner cylinder of q"=50000 W/m^2, a fixed temperature on the outside cylinder of T=283 K and symmetry applied everywhere else.

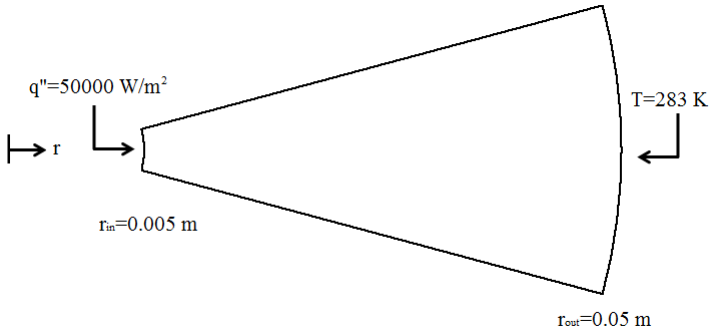

Figure 3.1: Diagram of Geometry used for steady state steel rod simulations

Governing equation [36]:

$$\frac{1}{r}\frac{d}{dr}\left(r\frac{dT}{dr}\right) = 0 \tag{3.1}$$

Boundary conditions:

$$r_{in} = 0.005\ m \qquad q"(r_{in}) = 50000\ W/m^2 \tag{3.2}$$

$$r_{out} = 0.05\ m \qquad T(r_{out}) = 283\ K \tag{3.3}$$

The analytical solution is given by [36], where L=1 m:

$$T = q"(2\pi r_{in} L)\left(\frac{\ln \frac{r_{out}}{r}}{2\pi k}\right) + T_2 \tag{3.4}$$

$$T = 50000(0.005)\left(\frac{\ln \frac{0.05}{r}}{60.5}\right) + 283 \tag{3.5}$$

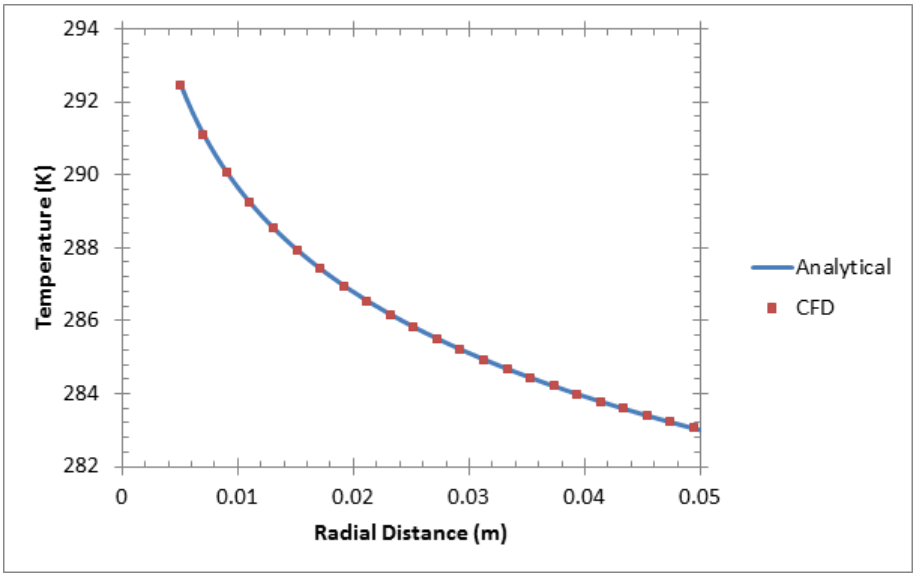

Figure 3.2: Comparison of the analytical solution and CFD result of the steady state temperature profile of a cylindrical steel wedge

Simulation results are compared to the analytical solution as shown in Figure 3.2 and as expected, there is excellent agreement between the two.

3.2 Transient Semi-Infinite Steel Rod

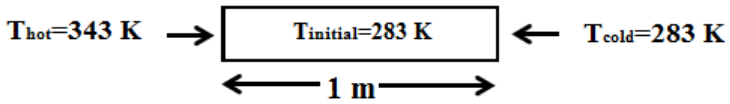

Figure 3.3: Diagram of Geometry used for 1D conduction and compared to the semi-infinite plate solution

A rectangular steel rod with the conditions given in Figure 3.3 was modelled to verify the ability to correctly predict transient problems. The simulation time was 57000 s with 10 s timesteps. Since this problem is one dimensional, the mesh consisted of 30 nodes along the length of the rod.

Governing equation:

$$\rho C_p \frac{\partial T}{\partial t} = k \frac{\partial^2 T}{\partial x^2} \tag{3.6}$$

Analytical solution:

$$\frac{T(x,t) - T_i}{T_s - T_i} = erfc\left(\frac{x}{2\sqrt{\alpha t}}\right) \tag{3.7}$$

$$\frac{T(x,t) - 283}{343 - 283} = erfc\left(\frac{x}{2\sqrt{\frac{60.5}{7854 \times 4.34 \times 10^2} t}}\right) \tag{3.8}$$

$$T(x,t) = 60 erfc\left(\frac{x}{2\sqrt{1.77 \times 10^{-5} t}}\right) + 283 \tag{3.9}$$

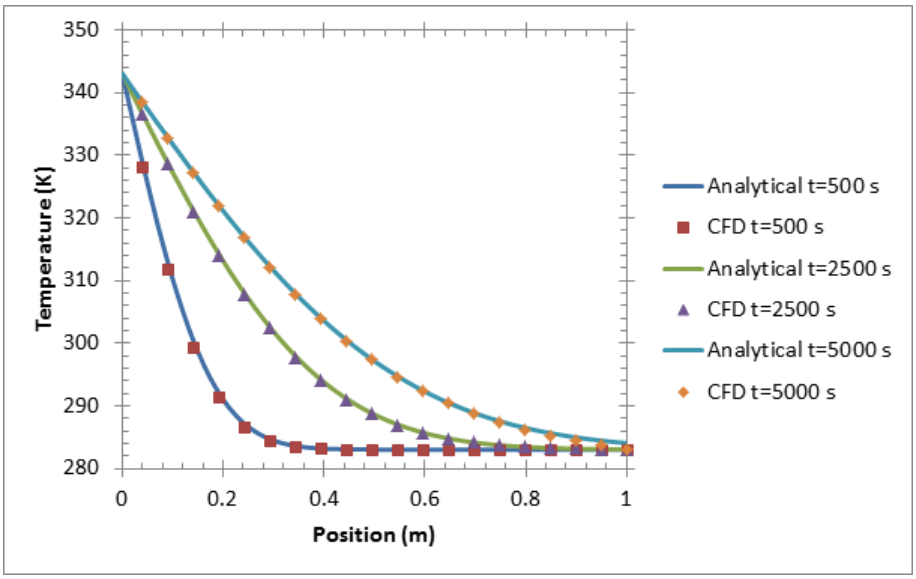

Figure 3.4: Comparison of the analytical solution and CFD result for heat conduction in a semi-infinite rectangular steel rod

The steel rod was compared to the semi-infinite plate solution, shown in Figure 3.3, which provides an accurate solution until the point where the outer wall temperature starts to change. As shown in Figure 3.4, excellent agreement exists between the simulation and the expected solution at early times. At long times, the heat travels along the length of the rod and reaches the other side. At this point, the solution will not match the analytical as the boundary condition of the finite rod will start impacting the solution.

The rod was modelled using properties of steel initially, but the simulation was re-run with the properties of soil to ensure the simulation runs correctly. The duration was changed to 865000 s and the timesteps to 1000 s since soil has a larger time constant as compared to steel. As expected, the results match the analytical solution well.

3.3 Effect of Borehole Shape

Changing the borehole shape in the simulations from circles to squares was considered to simplify the meshing process. To assess the impact of this treatment, simulations were carried out using the same perimeter for both types of boreholes, as seen in Figure 3.5, and then the temperature profiles were compared. The simulation ran for 150 days (around 1 charging cycle) with timesteps of 1 day.

Unless otherwise stated, all simulations from this point forward are using soil properties of ρ=1600 kg/m^3, C$_p$=1480 J/kg·K and k=2 W/m·K. These are fairly average values for soil. The initial condition is 283 K, or the average undisturbed ground temperature in Canada [27].

The radius of the round borehole is 150 mm, and the side length for the square borehole is 118 mm. The borehole temperature is 343 K, the outer walls are at 283 K and all remaining sides have a symmetry boundary condition. There were 50 nodes in the radial direction and 2900 nodes total in the simulation.

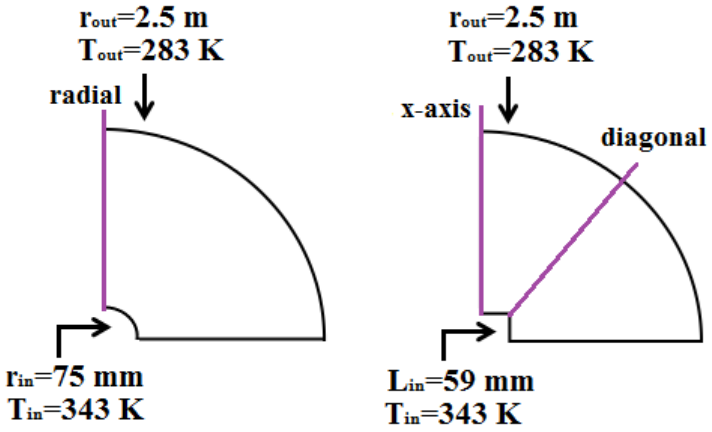

Figure 3.5: Comparison of a square vs a circular borehole with identical perimeters

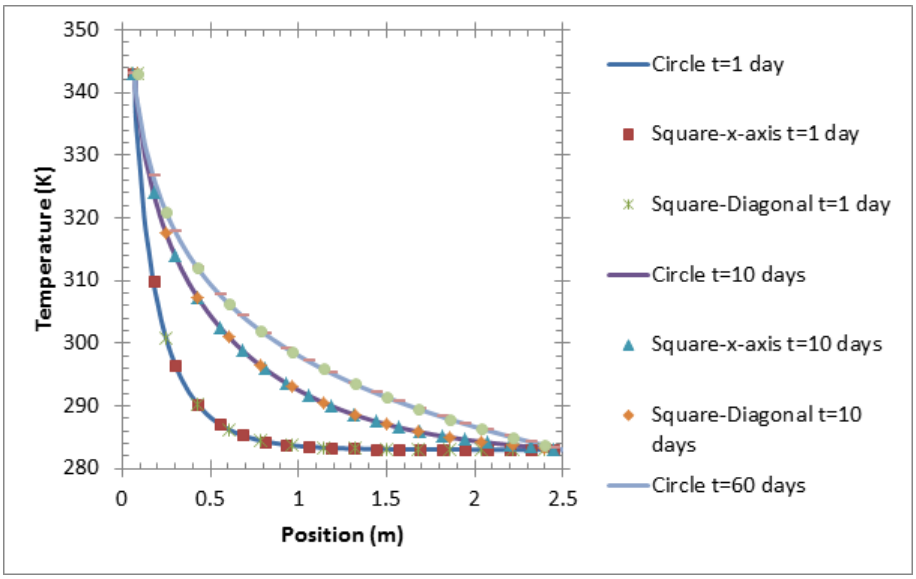

Figure 3.6: Comparison of the temperature profiles extending from a square and circular borehole

Predictions from both simulations at times of one, ten and 60 days are shown in Figure 3.6. As observed in the figure, the temperature profiles are nearly identical with a maximum difference at the borehole wall due to differing temperature profile lengths. For the square borehole, the temperature profiles along both the x-axis and diagonal orientation were considered, and as can be seen in the figure above, did not make a significant difference.

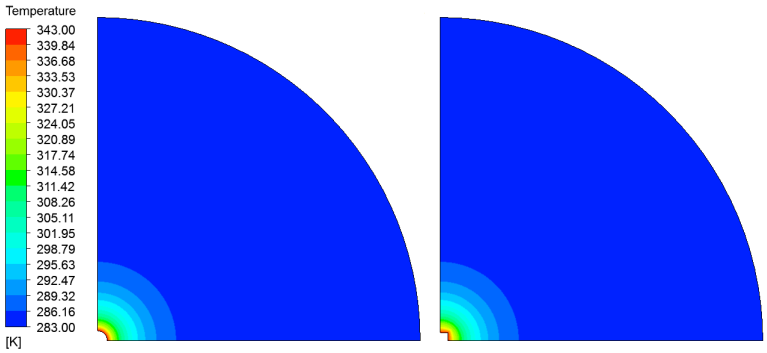

Figure 3.7: Contour plot of temperature of a round (left) vs a square (right) borehole at time t=30 days

The contour plots in Figure 3.7 were taken at time t=30 days, which is relatively early in the transient simulation. The square boreholes temperature contours became round within about one diameter, and considering that the boreholes diameter is around 150 mm, and the size of the domain is 35 m or greater, this is a negligible difference. In the case of a borehole field the spacing between boreholes is typically between 2 m to 5 m. As such 150 mm should not make a significant difference for that case either.

3.4 Effect of Tank & Domain Shape

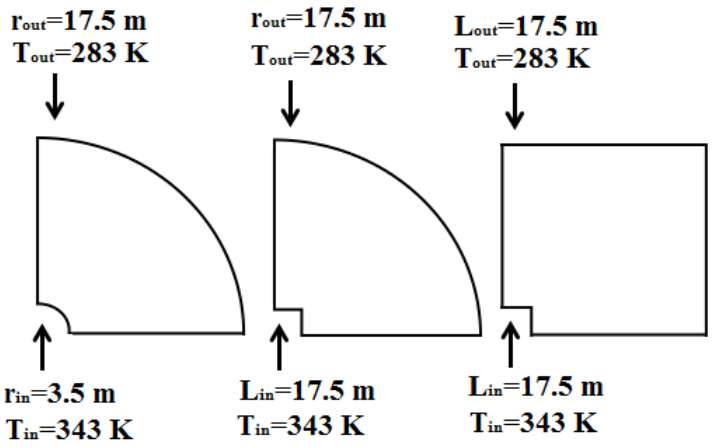

Figure 3.8: Comparison of a square vs a circular tanks and domains

Similar to the boreholes, the shape of the tank needs to be investigated as well. The tank has been changed from a circular cross section to a square. This is for two reasons: one, to simplify the meshing process, and two, because it better fits with the square grid layout of the borehole field. Unlike the boreholes, where the perimeter of the borehole was kept constant, for the tank, the volume and the surface area of the sides of the tank were kept constant to match the STTS at DLSC. This resulted in the diameter of the round tank and the width of the square both being 7 m, but the round has a depth of 7 m, and the square 5.5 m (though this will not be seen in the 2D simulation presented here). These simulations assess the impact of a circular vs square tank. The shape of the overall domain has also been considered. Changing the domain from a circular outer boundary to a square eases the meshing and results in a better quality mesh.

Three geometric configurations were considered: a circular tank in a circular domain, a square tank in a circular domain and, a square tank in a square domain.

All three geometries can be seen in Figure 3.8. The simulations were run with the properties of soil, for 1 year (365 days) with a timestep of 1 day. There were 50 nodes in the radial direction, with 3000 nodes total for the circular tank and 2900 nodes total for the other two cases. The tank was set to 343 K, the outer boundary was 283 K and all other boundaries were symmetry.

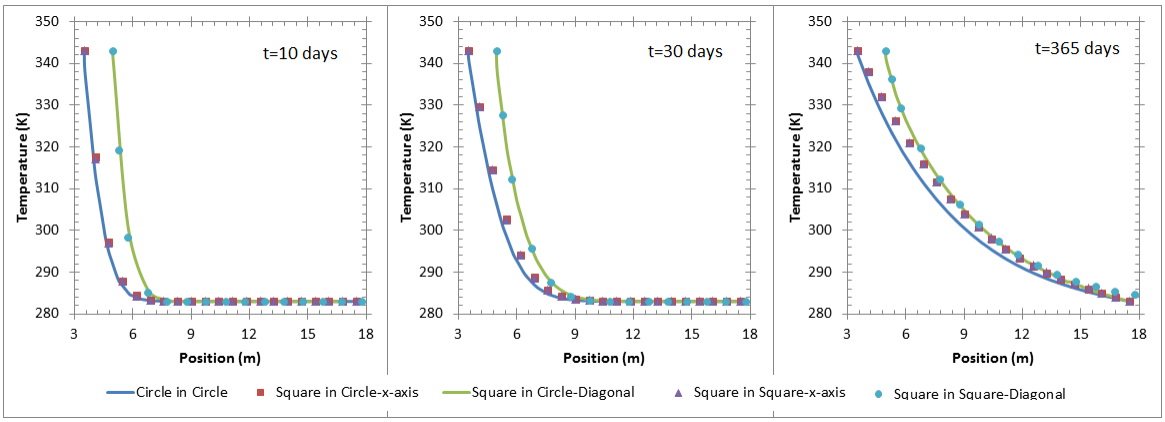

Figure 3.9: Comparison of different tank and domain shapes at time t=10, 30 and 365 days, note x-axis cropped to 18 m as only the diagonal direction has a temperature profile beyond this point (roughly 24.75 m)

Figure 3.9 shows temperature profiles at three different times for the three geometries of interest. It should be noted that for the square tank geometry, the profile depending on whether it was taken along a line coinciding with the x-axis versus a line that crosses diagonally across the domain. The graphs show that all the profiles have a similar trend. The largest discrepancy between the five profiles is due to their lengths. This is because the corner of the tank is a larger distance away from the origin as compared to the side. As time progresses, it can be observed that the profiles are all starting to overlap.

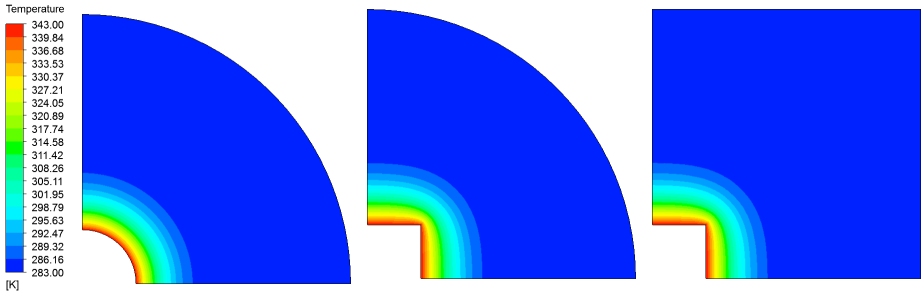

Figure 3.10: Contour plot of temperature of a round tank within a round domain (left), a square tank within a round domain (middle) and a square tank within a square domain (right) at time t=30 days

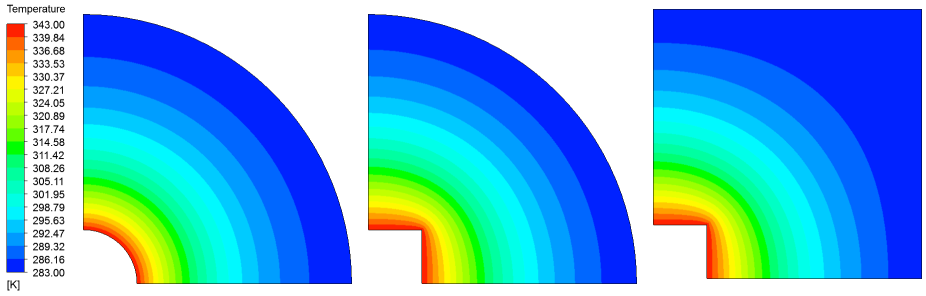

Figure 3.11: Contour plot of temperature of a round tank within a round domain (left), a square tank within a round domain (middle) and a square tank within a square domain (right) at time t=365 days

All three simulations have round temperature contours within 30 days as can be seen in Figures 3.10. Similar to the boreholes, the square tanks temperature contours become round in a fairly short distance of around 2 m, so the biggest difference between the two tanks will be within a few meters of the tank. The shape of the boundary also does not have an impact on the temperature profile as this boundary was set such that it is far enough away from the tank. Figure 3.11 show the contours again after 365 days, and the contours remain very similar.

3.5 Effect of Domain Size

Simulations were performed on two geometries; one with double the domain size of the other (17.5 m vs 35 m), but with the same sized tank (3.5 m in length). This simulation has the same initial and boundary condition as the previous set. It also ran for 365 days with a timestep of 1 day. The overall size of the domain must be carefully selected to ensure the boundaries are not having an impact on the temperature profile. The mesh was selected such that the control volumes in both simulations remain the same.

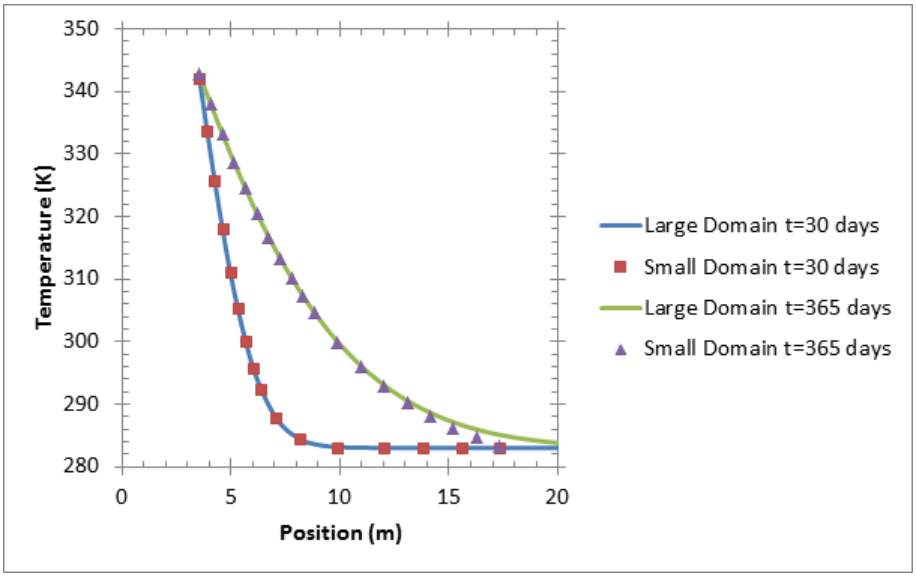

Figure 3.12: Temperature profiles for a 3.5 m by 3.5 m tank within a small (17.5 m by 17.5 m) domain vs a large (35 m by 35 m) domain

Figure 3.12 shows that the temperature profiles were the same up until the point where the heat reaches the edge of the boundary. Note that this graph was cropped to 20 m as the small domain is only 17.5 m wide.

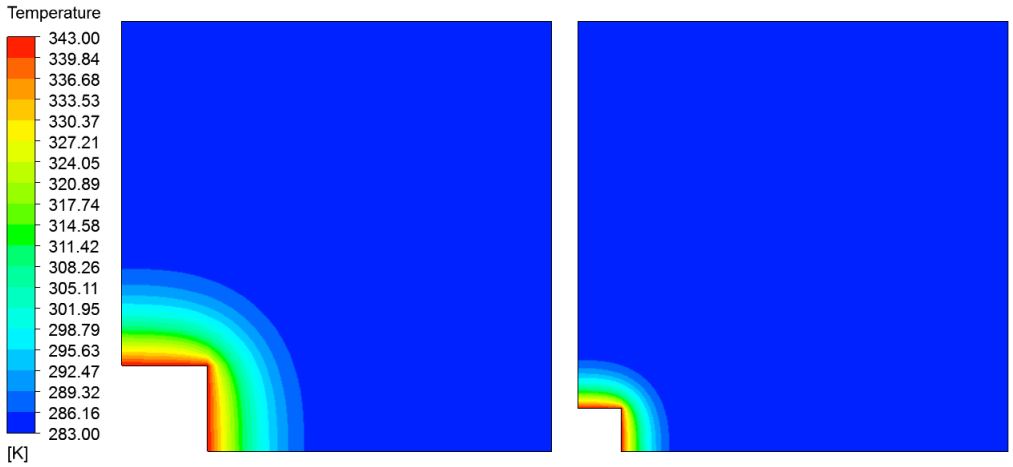

Figure 3.13: Contour plot of temperature of a small domain (left) and a large domain (right) at time t=30 days

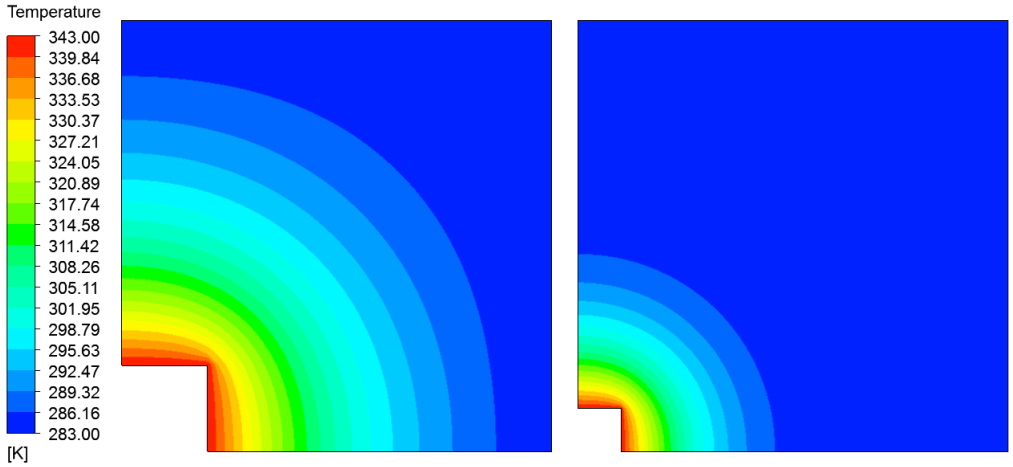

Figure 3.14: Contour plot of temperature of a small domain (left) and a large domain (right) at time t=365 days

As can be seen from Figures 3.13 and 3.14, the heat does not reach the edge of the domain, even after the simulation has been run for a year. In reality, the tank and boreholes would constantly be charged and discharged, which makes it less likely for the energy to reach the domain edge. These simulations will need to be re-considered if there are boreholes closer to the edge of the domain.

3.6 Superposition of Two Rods

It can be shown (both analytically and through simulations) that a rod with one end fixed at 30°C and the other at 20°C (hot & cold rod) with an initial condition of T=0°C everywhere can be treated as the superposition of a "hot" rod and a "cold" rod as shown in Figure 3.15 below. This is essentially the superposition of two of the semi-infinite plate solutions, which has been previously verified. As such, three CFD simulations were run and compared to each other, instead of the analytical solution.

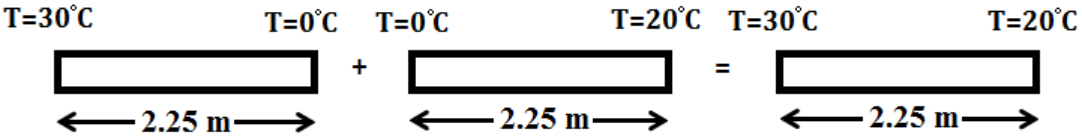

Figure 3.15: 1D Superposition of a hot rod and a cold rod in comparison to a hot and cold rod

This simulation had a run time of 600 hours with a timestep of 30 minutes. The mesh had 50 nodes along the length of the rod as this is simply a one dimensional problem.

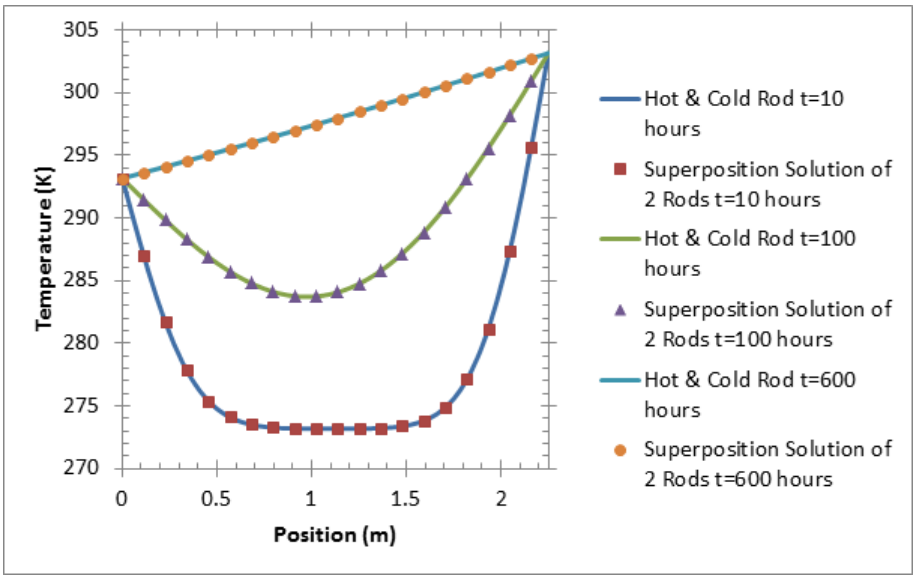

Figure 3.16: Transient temperature profiles of conduction in a rectangular rod with both ends heated vs two superimposed rods

Figure 3.16 shows the superposition solutions of the hot rod and cold rod as compared to the hot & cold rod. Excellent agreement between the simulations and superposition solution is seen, with a maximum difference of 0.05%.

3.7 Superposition of Two Boreholes in a Large Domain

A set of simulations involving a single borehole and two boreholes was performed. Superposition was once again applied to determine if the two borehole case will have the same temperature profile as two single boreholes overlaid and the geometries are presented in Figure 3.17

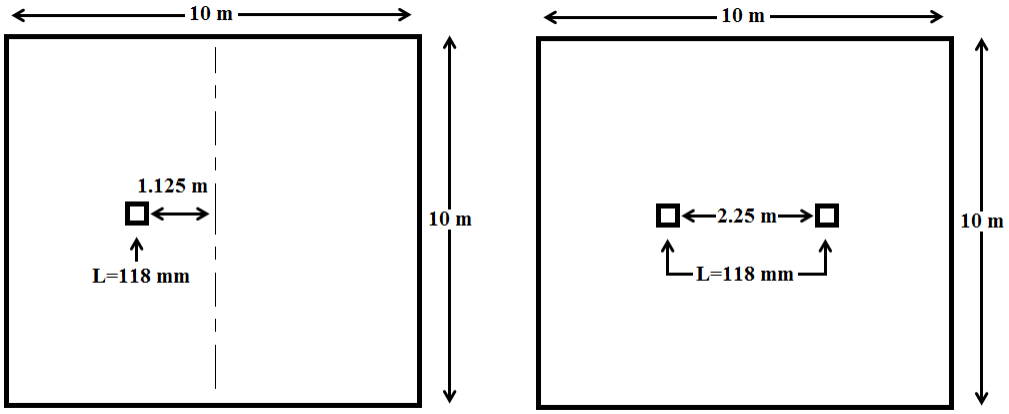

Figure 3.17: Diagram of a single borehole in a large domain (left) and two boreholes interacting in a large domain (right) (not to scale)

This simulation has the boreholes set to 343 K, the edges at 283 K, and symmetry on all other boundaries. The timesteps were 30 minutes, and the simulation was run for 500 hours.

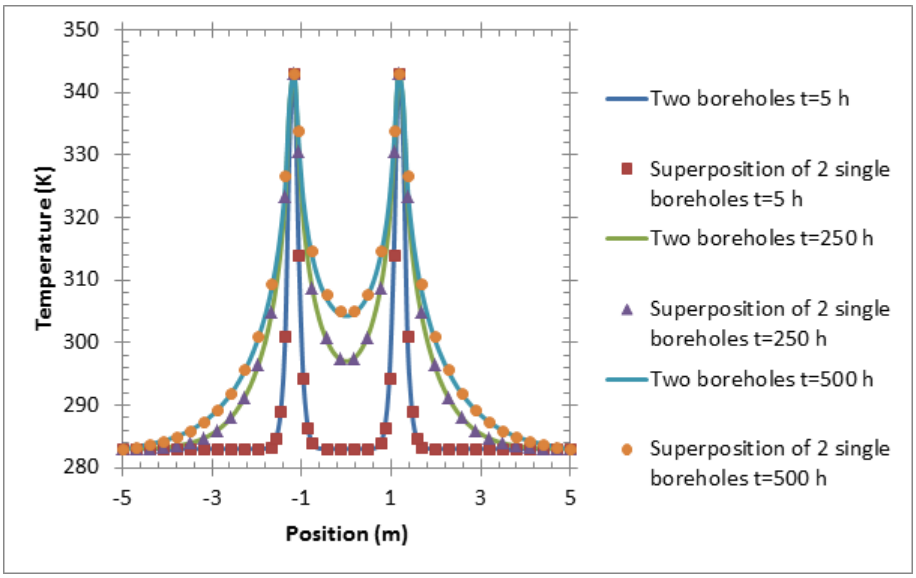

Figure 3.18: Superposition of two single boreholes compared to two boreholes

As can be seen in the Figure 3.18, the two simulations are in good agreement.

The biggest errors occur at the borehole wall at later times when the energy from one borehole and has reached the other one. This invalidates the boundary condition assumed for the superposition, resulting in extra heat being added to the two single boreholes solution. This is similar to how the semi-infinite plate solution is no longer accurate at later times when heat reaches the edge of the domain.

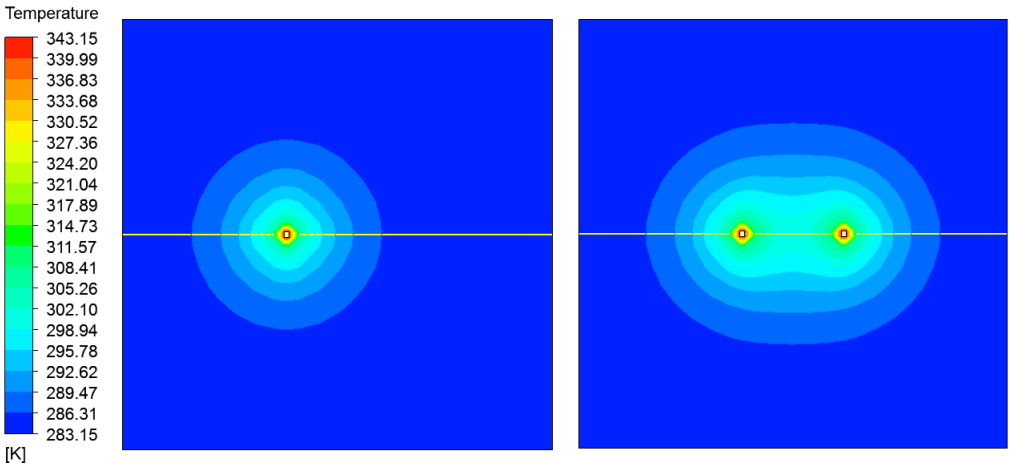

Figure 3.19: Temperature contours of a single borehole (left) and two interacting boreholes (right) at time t=500 hours

The contours in Figure 3.19 were taken at t=500 h. The heat from one borehole has reached the other. The yellow horizontal line represents the line along which the temperature profile was taken.

3.8 Verification of Borehole Transient Temperature Profile

An exact solution of transient heat transfer from a cylinder into a semi-infinite medium could not be obtained, so results from Philippe et al [35] were digitized

and used instead. Philippe et al used infinite line source theory to generate the results. In this simulation, a borehole with side length of 0.078 m (or 0.039 m in the domain) was placed within a 15 m by 15 m domain. The boundary conditions were selected to match those from Phillipe et al. The boundary condition for this borehole was a heat flux of q"=-159 W/m^2. This means that energy is leaving the domain and the borehole is discharging. The initial condition and outer boundary conditions were 8°C. The remaining boundaries have a symmetry boundary condition.

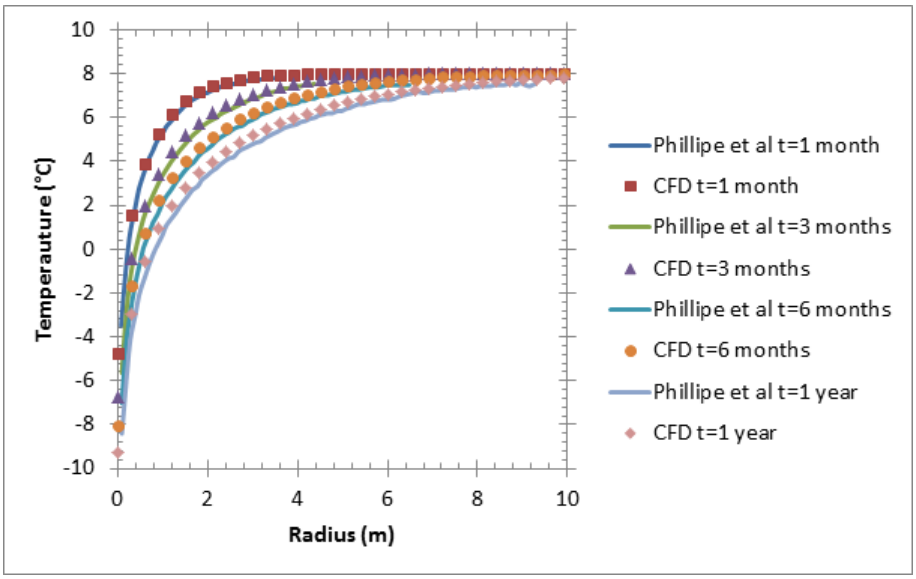

Figure 3.20: Verification of transient 2D conduction for a borehole based on Phillipe et al

There is good agreement between the solution presented and the CFD simulation, as observed in Figure 3.20.

3.9 Summary of Results

Verification for both a steady state and transient heat conduction problems with known analytical solutions were run and agreed with the expected solution. The impact of changing borehole, tank and domain shapes was tested and found to be of little consequence. The theory of superposition was verified, both for a rod and for interacting boreholes. And finally, simulations were run and compared against Philippe et al and it was found the results agreed well.

Chapter 4

Modelling & Methodology

This chapter presents the details on the geometry and meshing, initial and boundary conditions, and timestep and grid independence for the initial Base Case study. All simulations were run using ANSYS-CFX V12. Meshing was done using ICEM V12.

4.1 Base Case Geometry

The base case is motivated by the geometry and layout of the borehole field at DLSC and includes a tank that is roughly the same volume as the two STTS tanks at DLSC. It was selected as the simplest geometry to incorporate a buried tank within a borehole field based on the specifications of the existing layout at DLSC. The geometry consists of 45 boreholes in 5 rings surrounding a tank and can be seen in Figures 4.1 and 4.2. The boreholes have a square cross section[1] with a side length of 118 mm and depth of 30 m. The tank is also square and has a side length of 7 m and 5.5 m deep. Since the borehole field is symmetric, only one quarter of the domain is modelled, along

[1]The impact of modelling the boreholes as having a square rather than circular cross-section was assessed in Chapter 3

with one quarter of the tank. The boreholes are spaced 2.3 m apart, and the tank to borehole gap is 2.5 m.

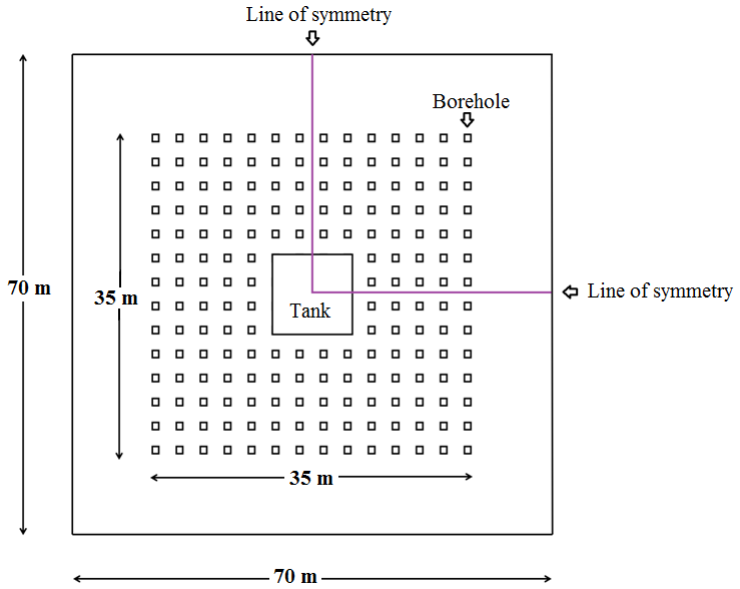

Figure 4.1: Top view of the base case geometry (not to scale)

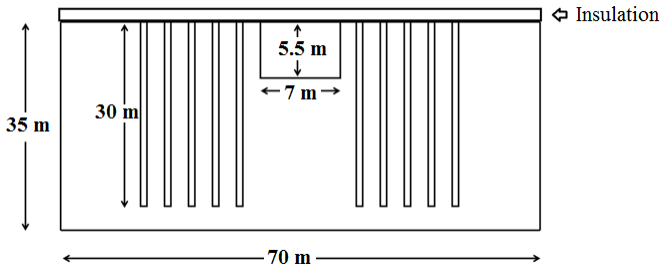

Figure 4.2: Side view geometry of the base case geometry (not to scale)

The simulation boundaries extend to 5 m below the bottom of the boreholes as well as 17.5 m away radially from the edge of the field in order to ensure that they do not impact the solution.

4.2 Initial & Boundary Conditions

The initial temperature of the domain was set to be uniform at 283 K, which is the average soil temperature in Canada. The ambient air temperature was taken to be a sine wave, based on historical data for Okotoks, Alberta (location of DLSC) for the year of 2012 [37] and is seen in the equation below:

$$T_{air} = 17sin\left(\frac{2\pi t}{365}\right) + 278 \tag{4.1}$$

where time is measured in days and temperature in Kelvin. The start of the simulation (ie, t=0) coincides with the conditions representative of the month of May.

The top of the borehole field at DLSC has 200 mm of XPS insulation [5]. This was inputted into the model using an effective heat transfer coefficient of h=0.01895 W/m^2K and the ambient air temperature. Details on the heat transfer coefficient calculations are provided in Appendix C. The vertical sides of the domain were also set to 283 K as the far-field temperature. The two remaining vertical sides of the domain had symmetry boundary conditions applied. The bottom boundary was set to a heat flux of q"=0.058 W/m^2, which is the average geothermal heat flux [38], where heat is flowing into the domain. The effect of a set temperature as compared to a set heat flux for the bottom boundary was investigated and it was found to have a negligible impact n the borehole field temperatures.

Unless otherwise specified, all simulations use data from DLSC for the year of July 2011 to June 2012 [39] that was analyzed and a temporal sinusoidal temperature transient for the tank and boreholes was established as:

$$T_{bh} = 12sin\left(\frac{2\pi t}{365}\right) + 323 \tag{4.2}$$

For the base case simulation, the tank walls and boreholes are set to a specified temperature which varies with time to reflect the overall borehole temperatures at DLSC.

More details on the top and bottom boundary conditions may be found in Appendix C.

The simulation was also tested for residual independence, and the results can be found in Appendix D.

4.3 Meshing

Presented in Figures 4.3 and 4.5 is the mesh used for the base case. The mesh is most refined in between the boreholes and expands in the far field since the gradients there are smaller. The total number of nodes for this mesh is 1,636,072. The aspect ratio varies depending on the region, as the gradients are higher in certain directions and the control volumes account for that.

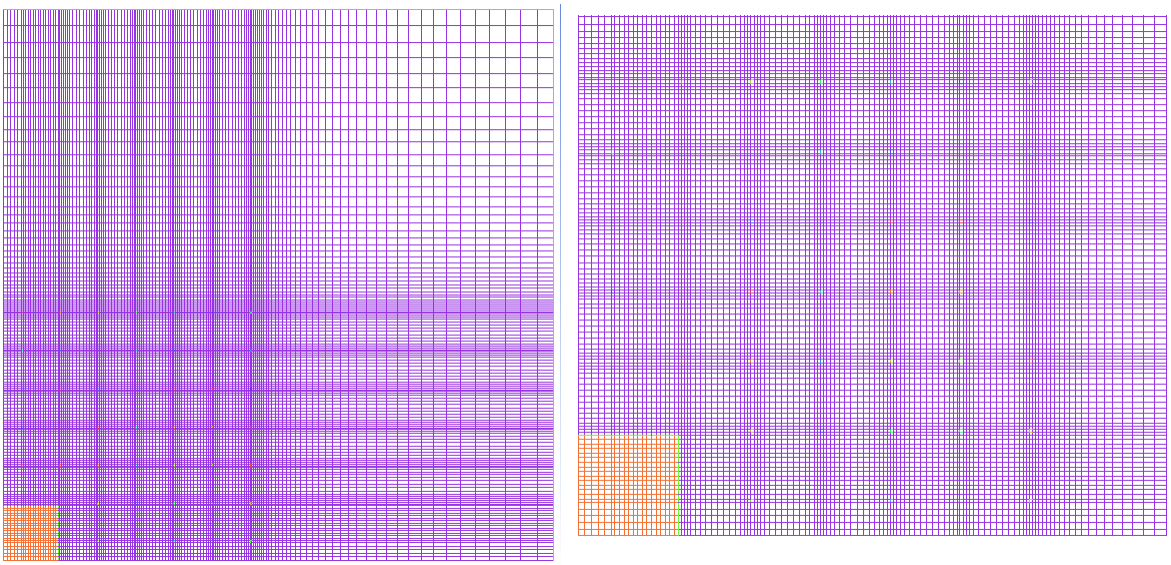

Figure 4.3: Top view of the base case mesh (left) and zoomed in (right)

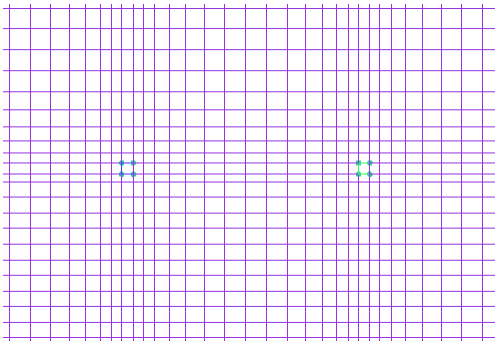

Figure 4.4: Top view of the base case mesh zoomed in around two boreholes

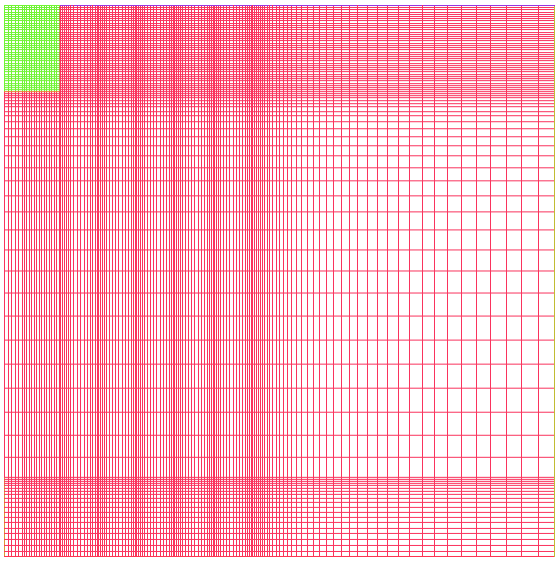

Figure 4.5: Side view of the base case mesh

4.4 Grid and Timestep Independence

Grid and timestep independence tests were carried out on the mesh presented in Figures 4.3, 4.5 and 4.4. This mesh were used for all subsequent tests that had the same borehole and tank geometry. For test cases in which the geometry of the tank or the number of boreholes was changed, a similar scaled grid was applied.

4.4.1 Timestep Independence Study

All timesteps were initially taken to be 24 hours. As seen in the previous chapter, this was sufficient for simple 2 dimensional modelling, however, timestep independence needed to be rechecked to ensure the simulation remained timestep independent. The timesteps were halved to 12 hours, and it was shown that the simulation remains timestep independent, the results of which can be observed in Figures 4.6 and 4.7.

The vertical temperature profile was taken from the bottom of the tank to the bottom of the domain at 1.75 m and 1.75 m into the domain (the middle of the tank in the domain) and the horizontal temperature profile was taken at y=-2.25 m (halfway down the tank) and x=1.16 m (through the plane containing boreholes closest to the edge of the domain).

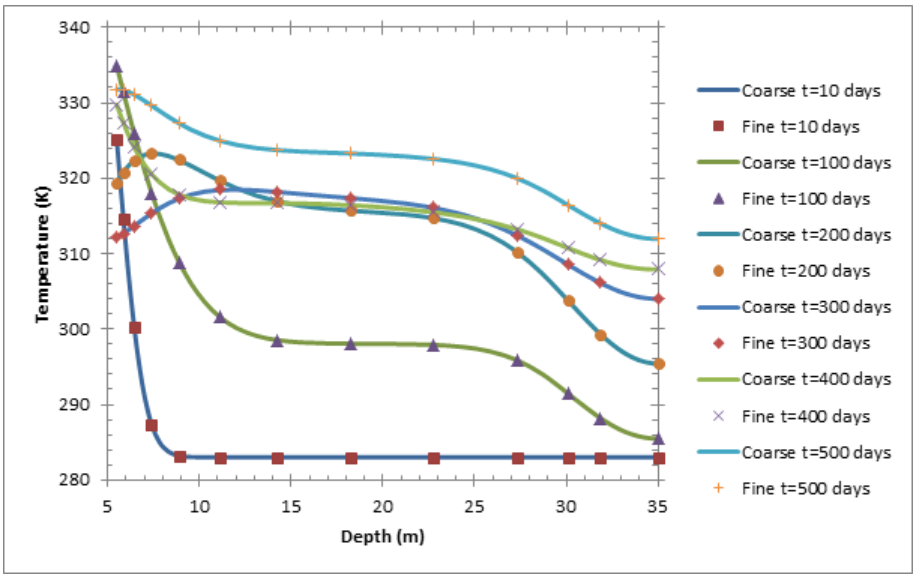

Figure 4.6: Timestep independence in the vertical direction (y-axis), where coarse=24 hours and fine=12 hours

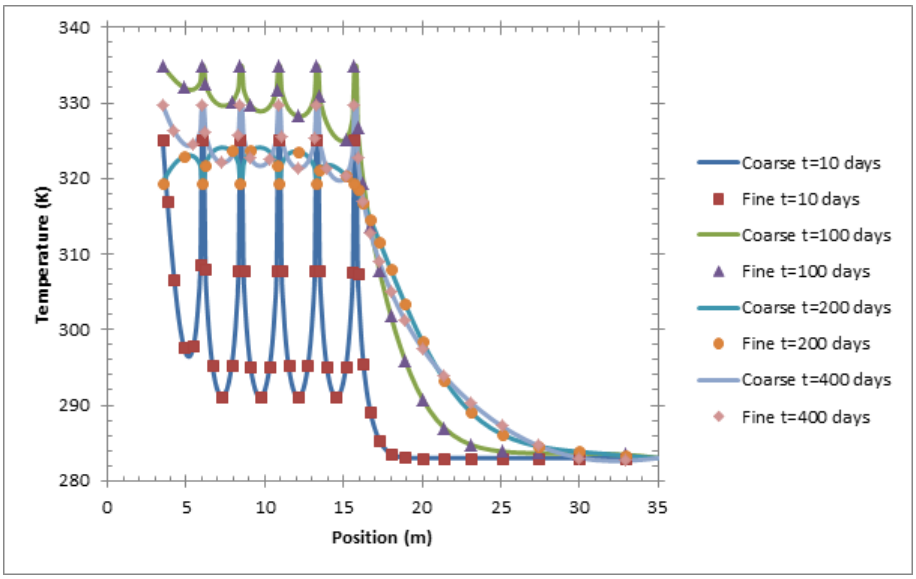

Figure 4.7: Timestep independence in the horizontal direction, where coarse=24 hours and fine=12 hours

4.4.2 Grid Independence Study: Vertical Direction

The mesh presented in Figure 4.5 was refined in the vertical direction by doubling the number of nodes adjacent to the boreholes from 70 to 140. This resulted in the total number of nodes for the entire mesh increasing from 1,636,072 to 2,933,902. Note that the mesh under the boreholes was not refined since the temperature is close to uniform in this region. The vertical temperature profile was taken in the same location as the timestep independence profile and results are shown in Figure 4.9. As seen in the figure, the predicted temperature is insensitive to the grid used.

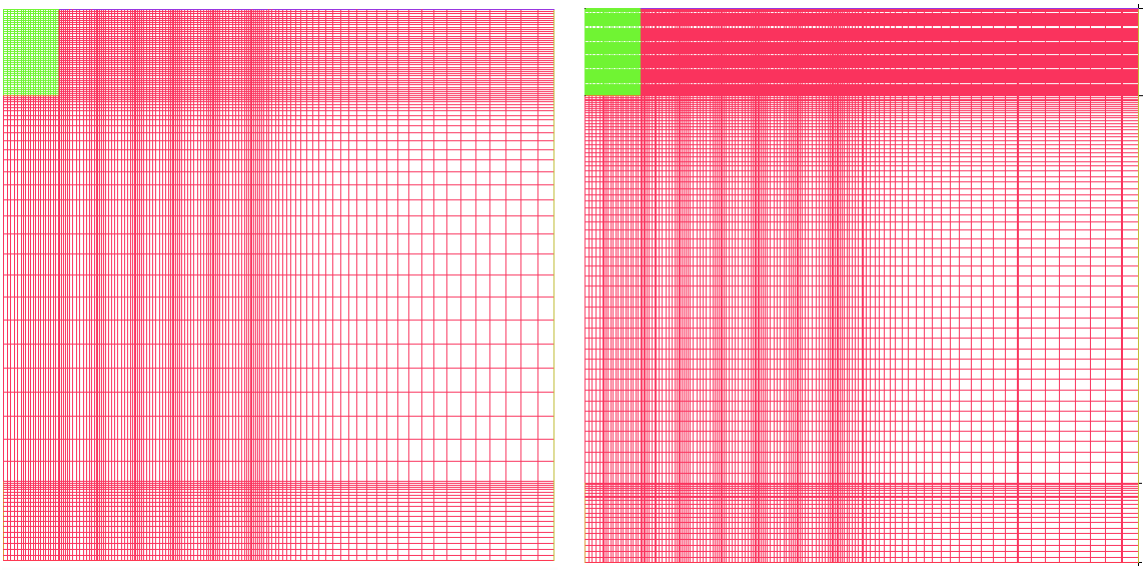

Figure 4.8: Side view of the base case mesh (left) compared to the mesh used for determining vertical grid independence (right)

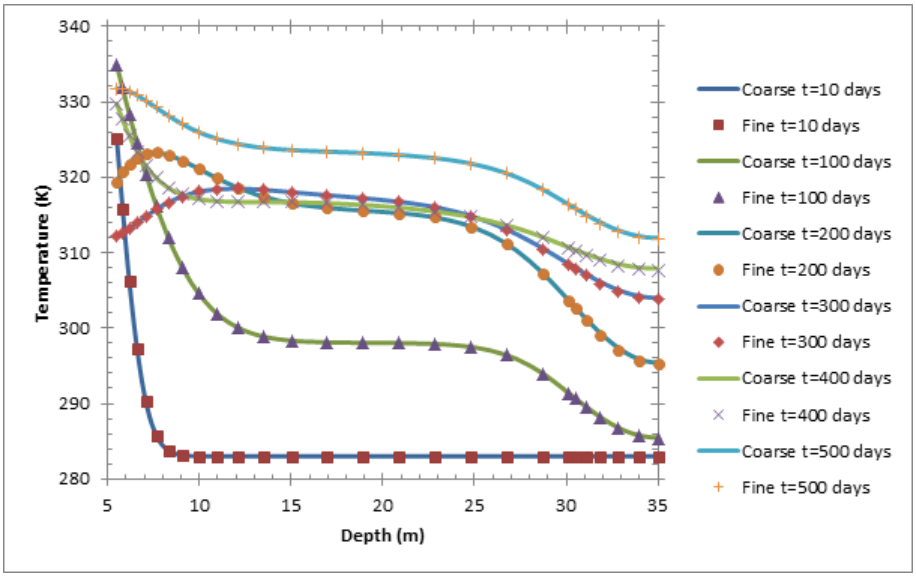

Figure 4.9: Grid independence in the vertical direction

4.4.3 Grid Independence Study: Horizontal Direction

For horizontal grid independence, the mesh presented in Figure 4.3 was doubled between the boreholes in the x-direction (from 96 to 192 in the region of refinement) which resulted in the total nodes increasing from 1,636,072 to 2,777,068. The meshes are shown in Figure 4.10. Due to the large domain size and symmetry along the x and z directions, doubling the nodes in both directions would make the simulation needlessly computationally expensive while providing relatively no new information. The horizontal temperature profile was taken in the same location as the timestep independence profile.

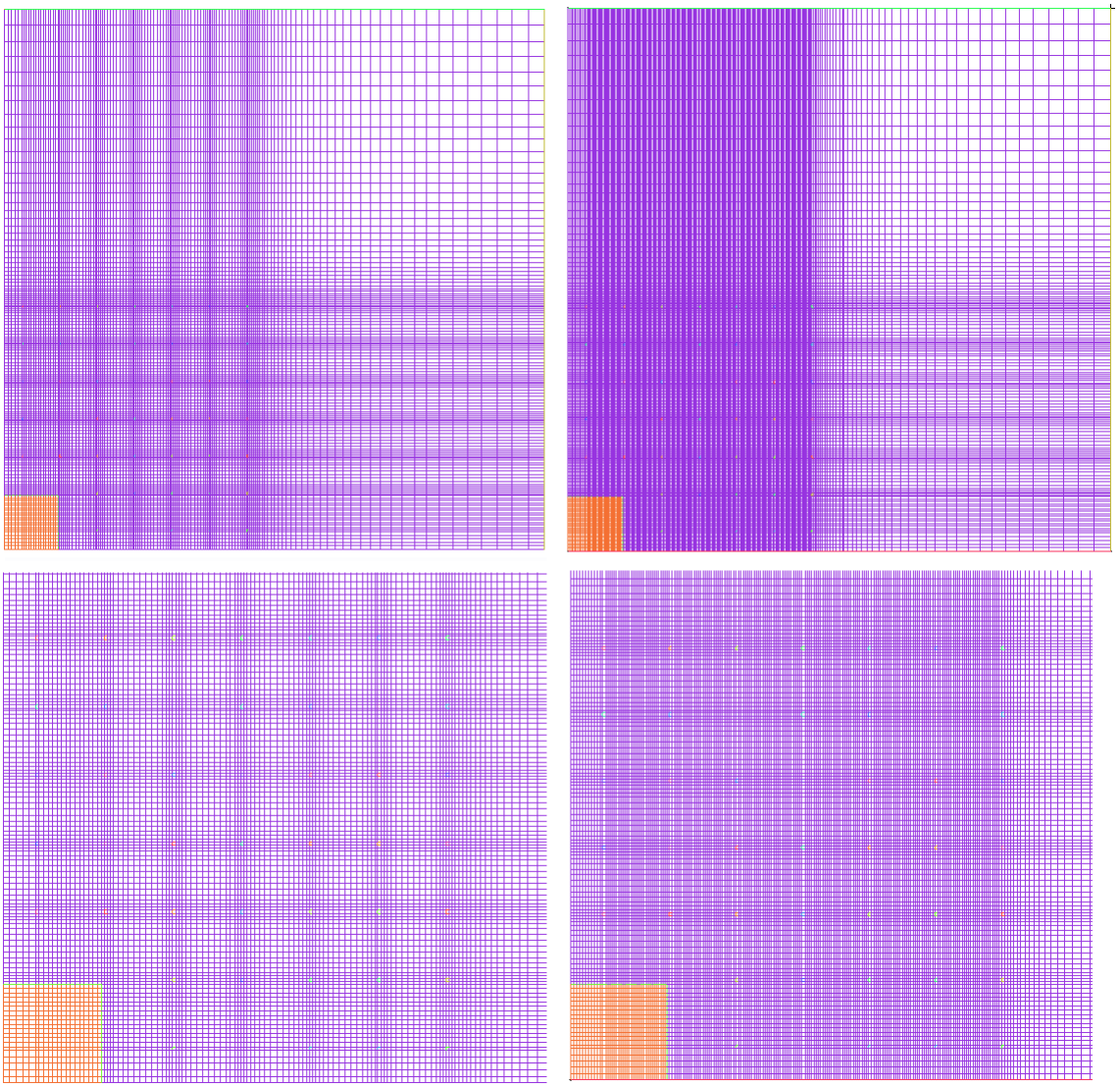

Figure 4.10: Top view of the base case mesh (top left) compared to the mesh used for determining horizontal grid independence (top right) and zoomed in versions (bottom)

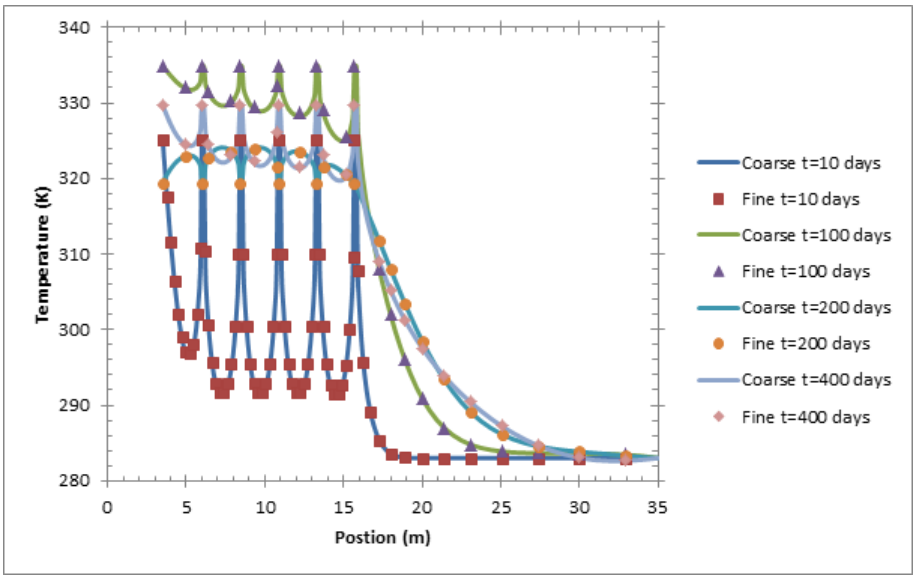

Figure 4.11: Grid independence in the horizontal direction (x-axis)

Figure 4.11 shows that the simulation is grid independent in the x direction and due to symmetry, the z direction as well.

4.5 Summary

This chapter presented the factors used in the methodology. The geometry, initial and boundary conditions were selected to be similar to DLSC. Care was taken to ensure that simulation results are independent of grid and timestep resolution.

Chapter 5

Results & Analysis

This chapter presents the results of the Base Case simulation as well as seven other sets of simulations that examine different parameters. Unless otherwise noted, all simulations were run using the geometry, meshes, initial and boundary conditions presented in Chapter 4 and can be viewed in Figure 5.1 below. The properties of soil are found in Chapter 3.

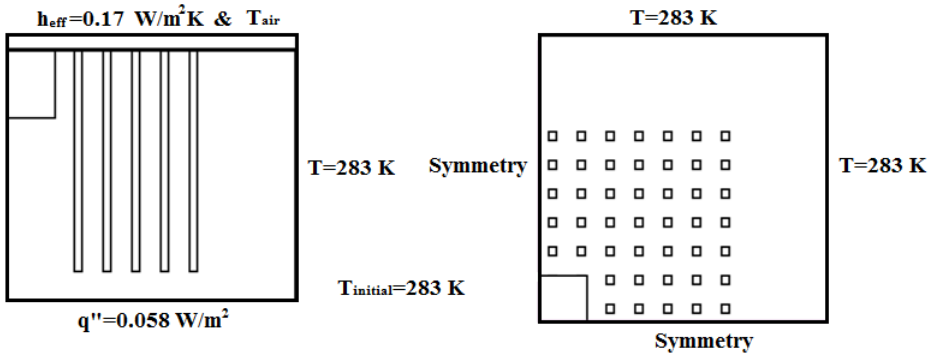

Figure 5.1: Geometry and boundary conditions for the base case, side view (left) and top view (right)

The temperature of the tank walls and the boreholes are important boundary

conditions for this problem. The temperature of these boundaries varies with time in order to represent the seasonal variation experienced at DLSC. The high temperatures coincide with charging the borehole field and the low temperatures with discharging. All simulations will use the borehole boundary condition provided in chapter 4 unless otherwise specified. The borehole temperature is plotted in Figure 5.2 below. Also shown is the air temperature.

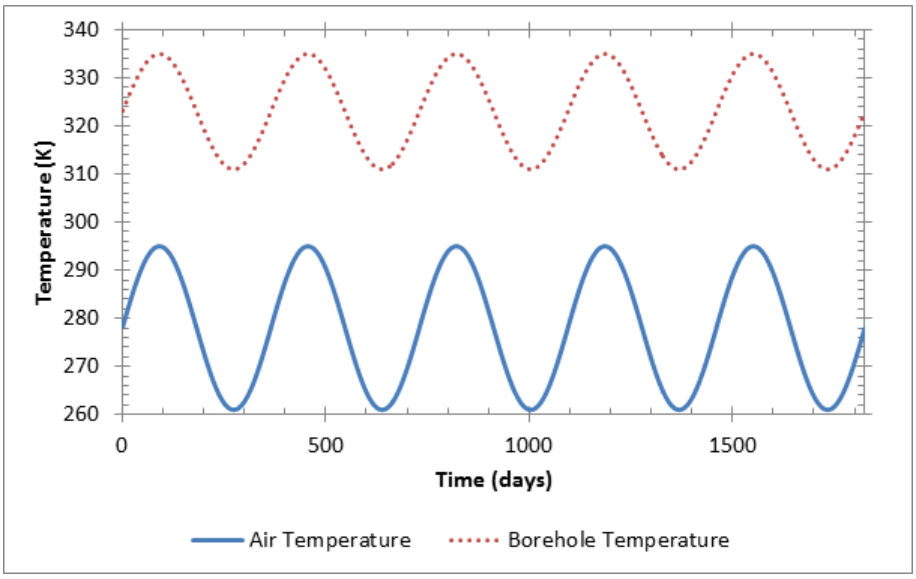

Figure 5.2: Temperature transients of the air and borehole temperatures

The soil was at an initial uniform ground temperature of 283 K and the heat transfer process was modelled to simulate the five year performance of the system.

5.1 Definition of Core Region & Soil Plug

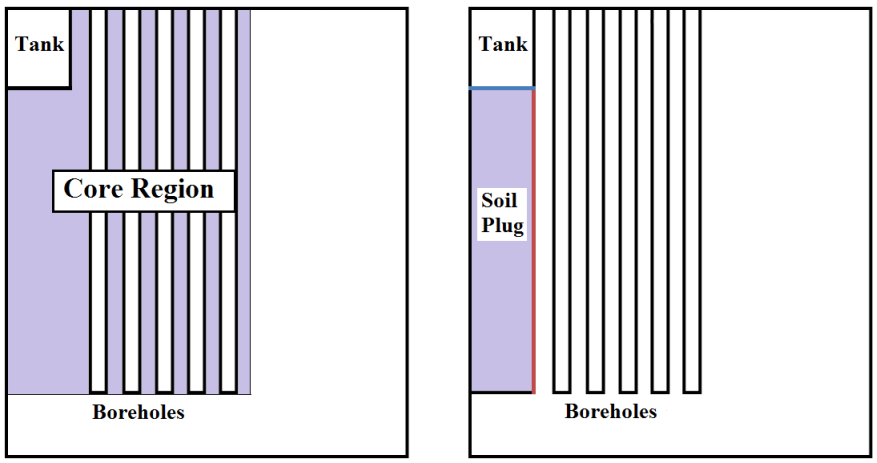

Figure 5.3: Diagram showing the location of the core region (left) and soil plug (right) (not to scale)

The domain was selected to be large enough to ensure that the location of the vertical boundaries does not interfere with the solution. As a result, a large portion of the domain away from the boreholes is not of great interest for the purposes of this study. To rectify this, a region is defined as the "core region", and can be observed in Figure 5.3.

The presence of the tank in the centre of the borehole field necessitates the displacement of boreholes from that region. As such, there is a column of soil below the tank that may act as an additional energy storage device and could influence the performance of the borehole field. The column of soil below the tank, shown in Figure 5.3, will be referred to herein as the "soil plug." The soil plug is within the core region. One of the goals of this research is to explore the thermal interaction of the "soil plug" with the adjacent boreholes and to assess the impact on the overall performance of the borehole field.

5.2 Base Case

The first simulation run was a Base Case, which is important as it will be used as the control and compared against several other simulations that change certain factors.

In the figures below, temperature contours of the first two years will be discussed. The side view is taken at z=1.16 m or through a plane containing boreholes, and the top view is taken at y=-15 m, or halfway down the length of the boreholes.

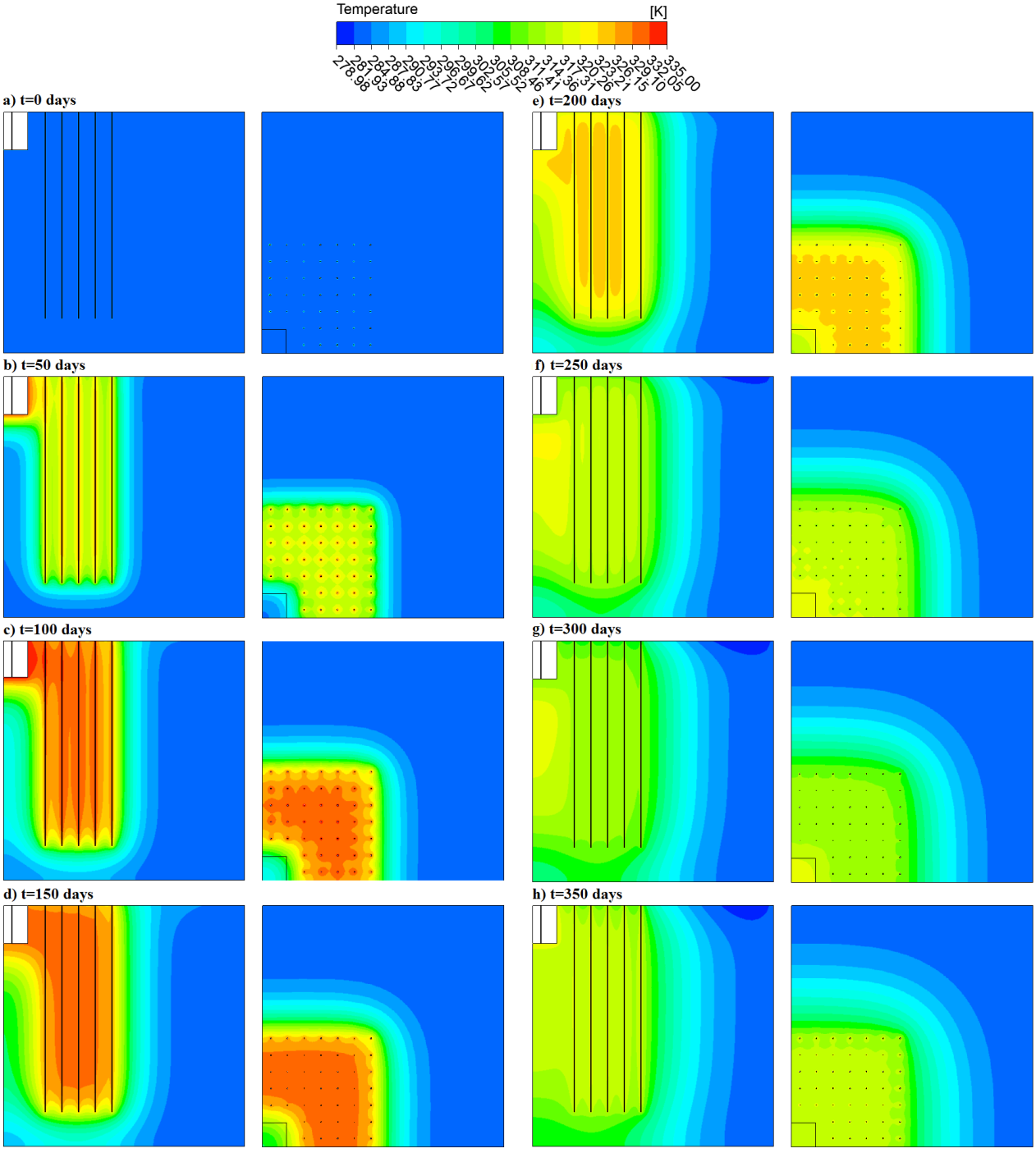

Figure 5.4: Temperature contour plots of the side view (plane containing boreholes, z=1.16 m) and top view (borehole half length, y=-15 m) of the base case during the first year of operation

At the initial condition, the soil everywhere is at 283 K. The start of charging representative of the condition in May. After 50 days, the soil in the core region starts to heat up and the plug of soil under the tank starts to see heat entering and the temperature increases to around 290 K. After 100 days, coinciding with the height of summer (August) the core region has reached its peak temperature of around 325 K. The volume of soil between the tank and boreholes is nearly fully charged at almost 335 K. The heat is also beginning to leave the core region transferring outwards, which is then unrecoverable. The plug of soil under the tank is not at as high temperature as the rest of the core as it is around 300 K. At 150 days, the temperature in the core region is starting to drop as the discharging cycle begins and the boreholes extract the energy out of the ground.

At 200 days (November), the core region temperature is still dropping. There is still a fair bit of heat in the borehole region, but the plug of soil under the tank is still seeing lower temperatures than the core at around 310 K compared to the 323 K in the core. As a result, there is a transfer of energy to the "soil plug" region from the borehole core and the temperature of the soil plug under the tank continues to increase even though the field is being discharged. After 250 days (January), heat is still being extracted. The losses out of the core region continues, even in the discharging cycle. The losses out of the top surface can also be observed by considering at the top right corner of the side view and noting the curvature of the isotherms. At 300 days, the discharging cycle continues, and almost all of the heat has been extracted. There is still a pocket of hot soil under the tank at 318 K compared to the core at around 311 K. Additionally, there is more heat lost to the ambient air. At 350 days, nearly an entire cycle, charging is starting again. The soil in the core region is at a relatively

uniform temperature around 314 K.

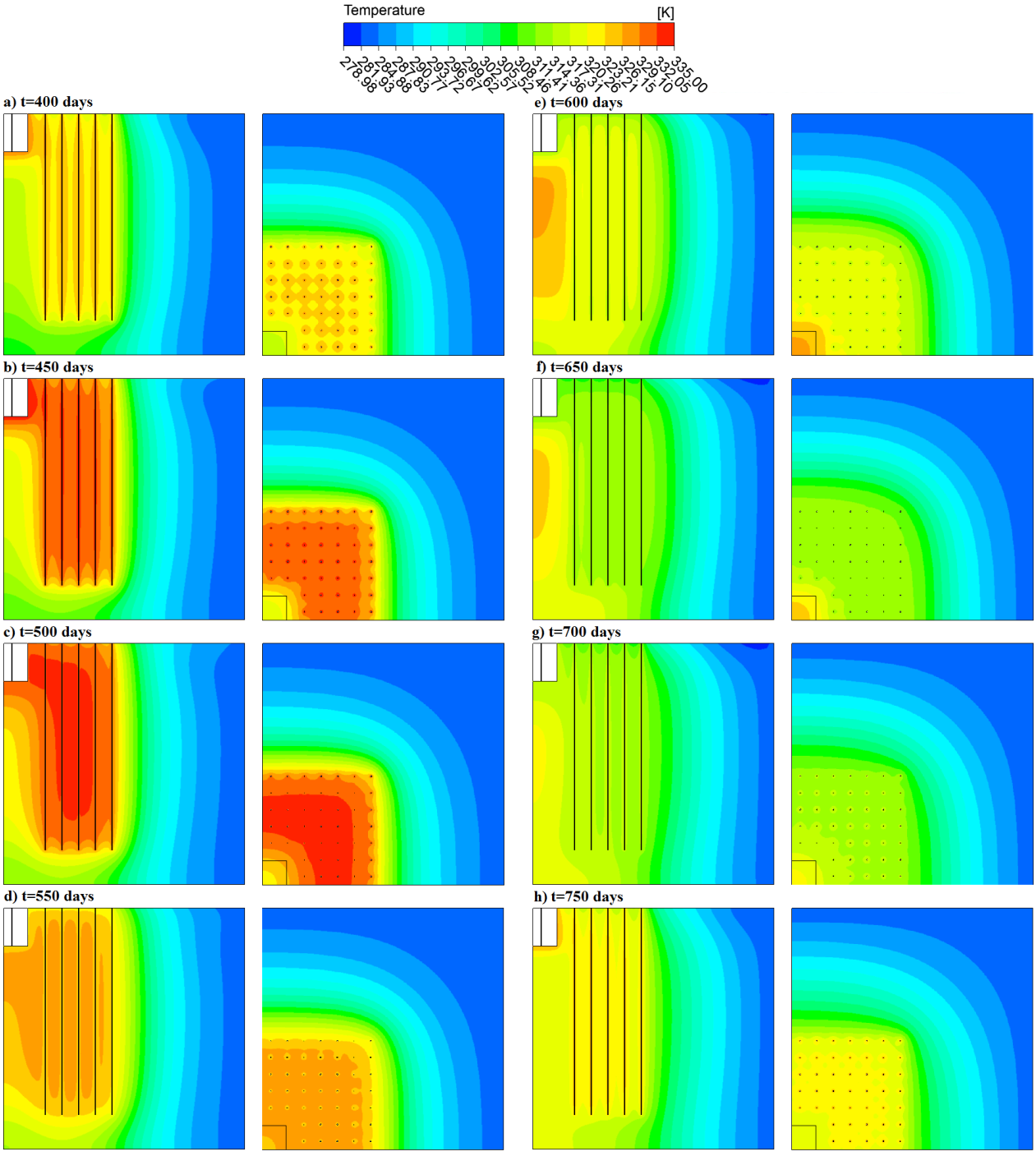

Figure 5.5: Temperature contour plots of the side view (plane containing boreholes, z=1.16 m) and top view (borehole half length, y=-15 m) of the base case during the second year of operation

After 400 days, the charging cycle has begun again. Since the soil in the core region was hotter than the initial soil (323 K, compared to 283 K for the uncharged ground), the core region takes less time to heat up. At 450 days (July), the charging continues. The heat front leaving the core region is penetrating further into the domain than during the first charging cycle. At 500 days, the core region has reached its peak temperature of around 330 K. Compared to the first charging cycle, the core region is hotter, as is the plug of soil under the tank. The core region is nearly saturated at this point. After 550 days, the discharging cycle has begun again.

At 600 days, discharging is continuing. There is again a pocket of hot soil under the tank, but it is hotter than the pocket in the first year. After 700 days (March), the field has nearly finished discharging. The pocket of hot soil under the tank has shrunk in size, but not all of the energy has been recovered. Finally, at 750 days (May), and the charging cycle recommences. The cycle from this point out is very similar to the second year, so further times will not be discussed. From these contour plots, it is evident that the effect of the boreholes is felt further into the domain as time progresses, and in general, the entire domain gets hotter.

Temperature

Spatially average temperature transients were taken of the core region and the soil plug to assess their behaviour.

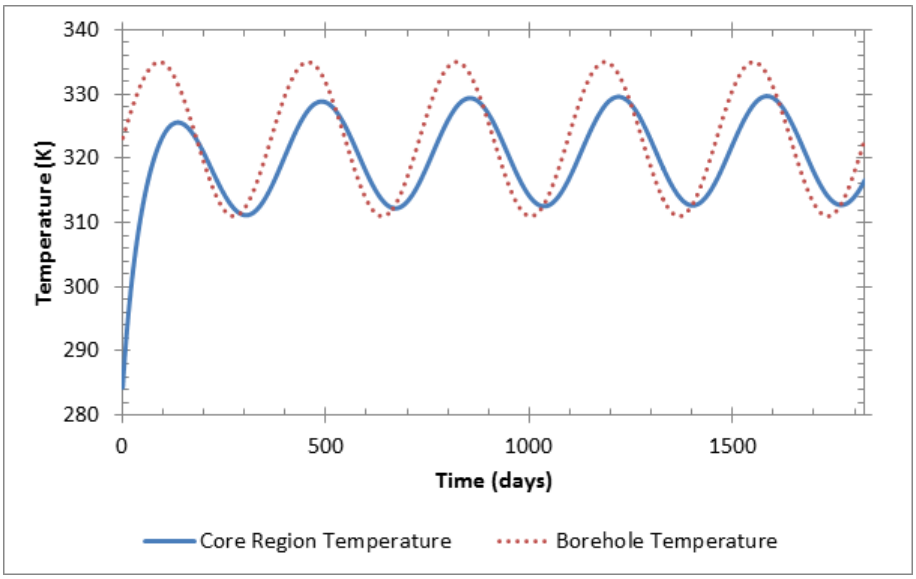

Figure 5.6: Temperature transient of the domain and the borehole boundary condition over 5 years for the base case

As can be seen in Figure 5.6, the temperature within the core reaches a periodic sinusoidal state after about two years. It does not get as hot as the maximum borehole temperature, but it forms a sinusoidal wave with the same period. There is a response time of about 30 days between the borehole temperature and core temperature. The core temperature fluctuates around 321 K. The midpoint of the borehole temperature is 323 K, and the difference between the two is due to heat losses from the core region.

In order to study the soil plug an investigation of the transient temperature distribution was performed.

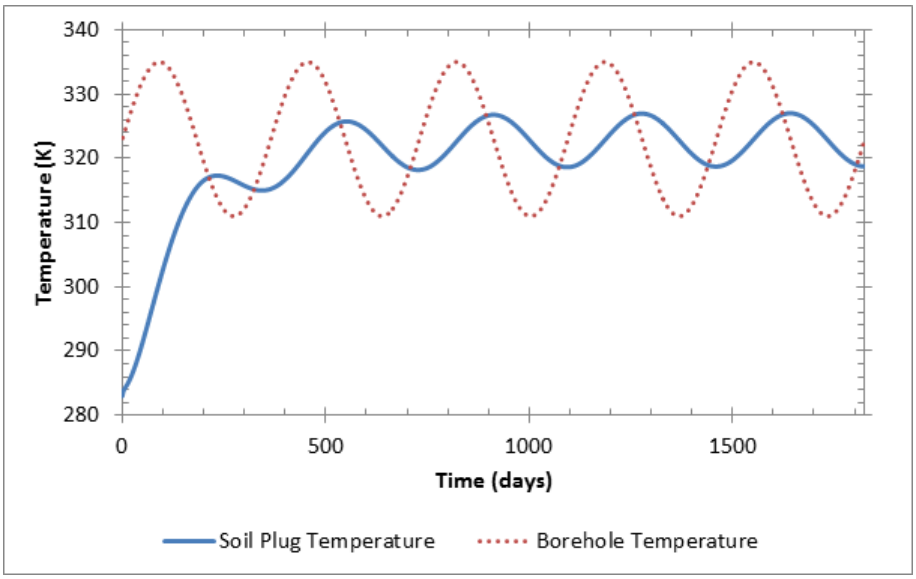

Figure 5.7: Temperature transient of the soil plug and the borehole boundary condition over 5 years

Figure 5.7 depicts the average temperature of the soil plug over time. Also shown, for reference is the applied transient borehole temperature boundary condition. In the first year, there is a large temperature increase from 283 K to almost 318 K. Subsequent years show that the soil plug temperature also follows a sinusoidal wave with a midpoint around 322.8 K, which is very close to the midpoint of the borehole temperature of 323 K. This indicates that the soil plug has reached a periodic sinusoidal state. The soil plug temperature significantly lags behind the borehole temperature due to the time taken for the heat to reach the soil plug, by around 100 days. This will be discussed further in the following section.

Soil Plug Heat Fluxes

Heat fluxes at the boundaries of the soil plug are shown in Figure 5.8. The blue line in the figure is the heat flux from the bottom of the water tank and the red dashed

line is the heat flux at the vertical boundaries of the soil plug. Positive heat flux is defined as a heat flux into the soil plug, and negative leaving the soil plug. This will give a complete analysis as to how the soil plug stores energy, and more importantly, the amount of energy that can be recovered.

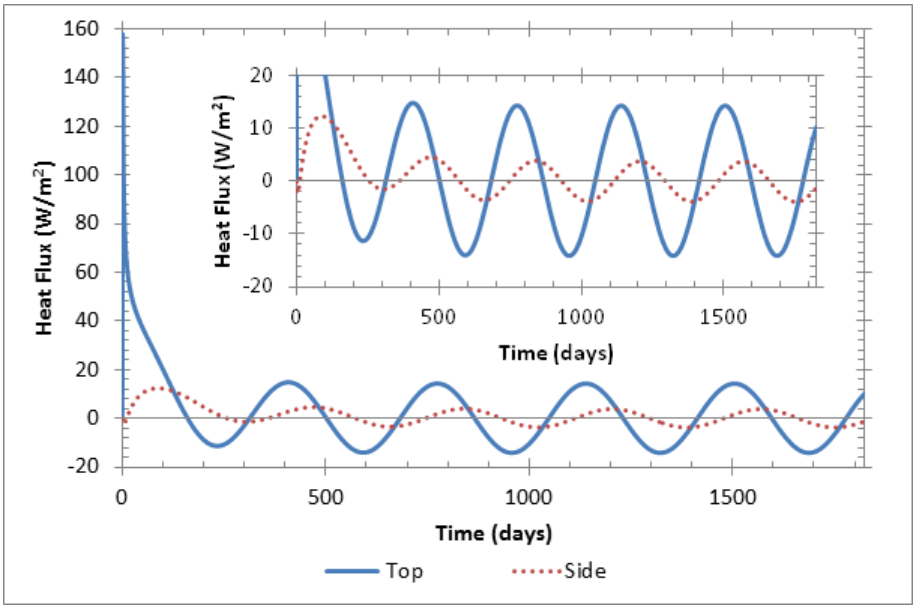

Figure 5.8: Heat fluxes to the soil plug for the base case over 5 years, with inset showing a zoomed in view

The two heat fluxes are nearly out of phase due to the difference in distance that the heat needs to travel. The heat flux from the bottom of the tank responds more quickly to changes of the tank temperature, but the heat fluxes at the side of the soil plug are a function of the borehole temperature, and those are displaced by 2.5 m. Therefore, as the borehole temperature changes, the soil plug will not respond to the borehole temperature change for some time according to the simple scaling analysis shown below.

The soil plug will be approximated as a one dimensional problem in cylindrical

coordinates, and the governing equation is as follows:

$$\frac{1}{\alpha}\frac{dT}{dt} = \frac{1}{r}\frac{d}{dr}\left(r\frac{dT}{dr}\right) \tag{5.1}$$

Non-dimensionalizing the equation using

$$\theta = \frac{T_2 - T}{T_2 - T_1}, \qquad t^* = \frac{t}{t_c}, \qquad r^* = \frac{r}{R} \tag{5.2}$$

will yield:

$$\frac{1}{\alpha}\frac{T_2 - T_1}{t_c}\frac{d\theta}{dt^*} = \frac{T_2 - T_1}{R^2}\frac{1}{r^*}\frac{d}{dr^*}\left(r^*\frac{d\theta}{dr^*}\right) \tag{5.3}$$

simplifying

$$\frac{R^2}{\alpha t_c}\frac{d\theta}{dt^*} = \frac{1}{r^*}\frac{d}{dr^*}\left(r^*\frac{d\theta}{dr^*}\right) \tag{5.4}$$

A time constant can be approximated as:

$$t_c = \frac{R^2}{\alpha} = \frac{3.5^2}{0.0797} = 168 \text{ days} \tag{5.5}$$

This is a comparable value to the 100 days that the soil plug temperature lags behind the borehole temperature that was seen in the previous section and Figure 5.7.

The corresponding heat transfer rates in units of MJ/day are shown in Figure 5.9.

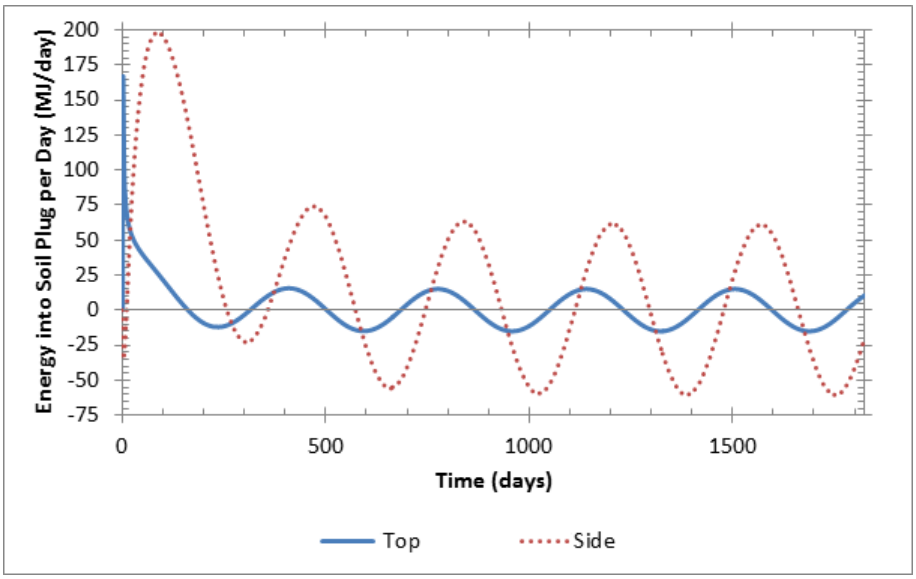

Figure 5.9: Energy injected and extracted from the soil plug for the base case over 5 years

As seen in Figure 5.9, the heat flux into the top of the soil plug is much higher than through the sides of the soil plug, however, due to the much larger area of the latter, more energy is injected through the sides of the soil plug as opposed to the top. Similar to the core and soil plug temperatures, the heat fluxes and energy both reach a sinusoidal state after about two cycles. This indicates that the energy injected into the soil plug can be recovered and the space underneath is not wasted. Due to he large time constant of the soil plug, however, the full capacity of that region as an energy store is not utilized.

5.2.1 Boreholes Field Performance

This section presents an analysis of the performance of full borehole field. It considers the heat transfer across all boundaries and the unrecoverable losses.

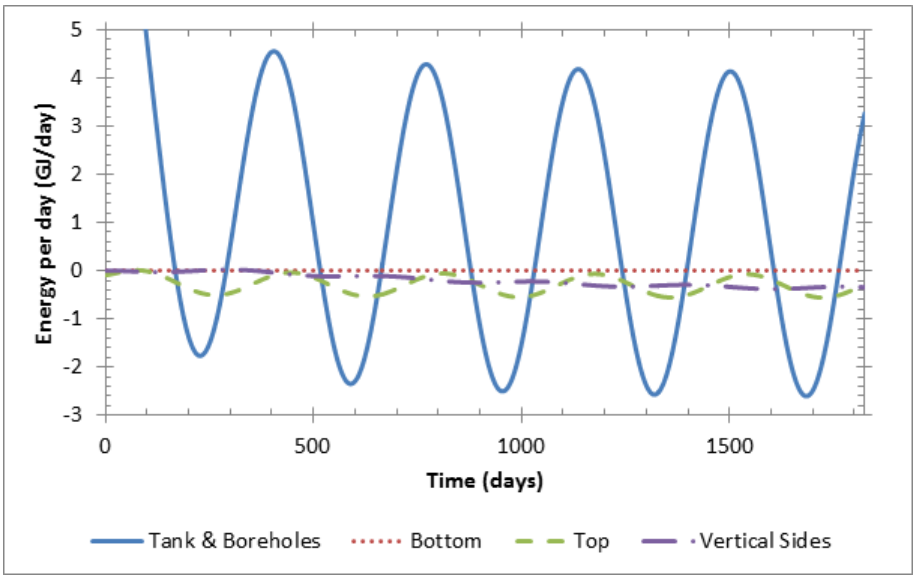

Figure 5.10: Energy injected and extracted from all boundaries over five years for the base case

Figure 5.10 shows the energy injected and extracted through each of the boundaries per day over five years. From the figure it can be seen that the losses (which have negative values) out the vertical sides increase in magnitude with time. This is because the heat front penetrates deeper into the field with each subsequent cycle, which leads to greater losses.

In order to study understand the performance of the overall field, the energy injected and extracted must first be studied on a borehole ring basis. In addition, an efficiency can be defined as:

$$\eta = \frac{Energy_{extracted}}{Energy_{injected}} \times 100\% \tag{5.6}$$

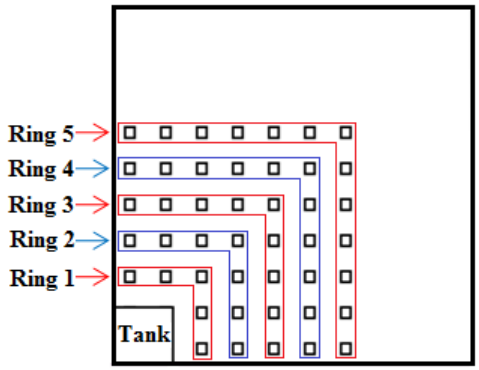

Figure 5.11: Location of borehole rings for the Base Case

Figure 5.11 shows the location of each borehole ring. This will be used to calculate energy injected and extracted as well as efficiency in the graphs below.

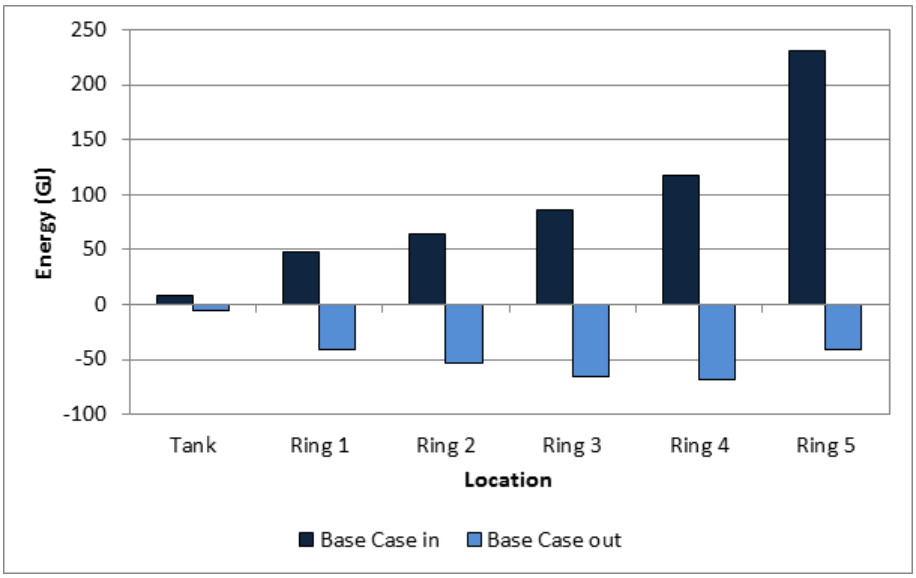

Figure 5.12: Energy injected and extracted for the base case by ring for Year 5

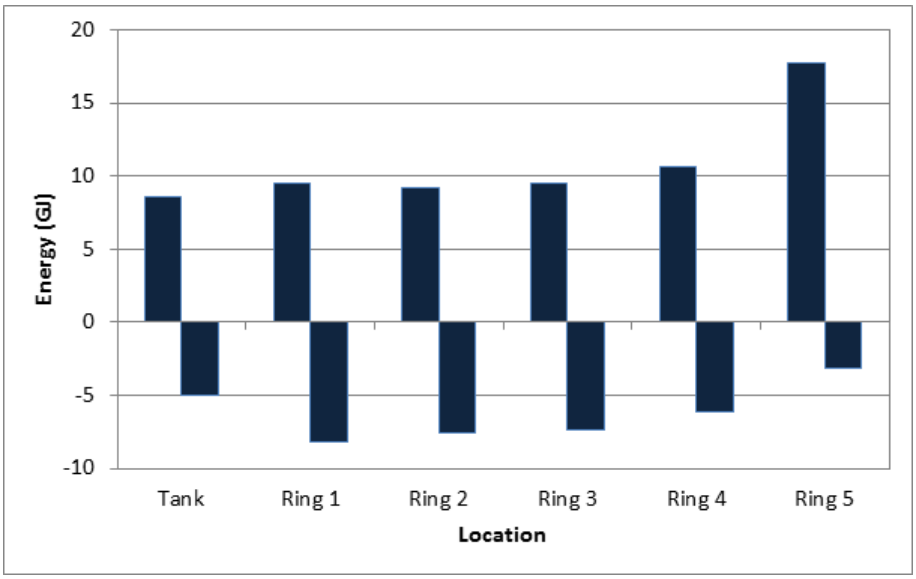

Figure 5.13: Average energy injected and extracted for the base case by ring for Year 5

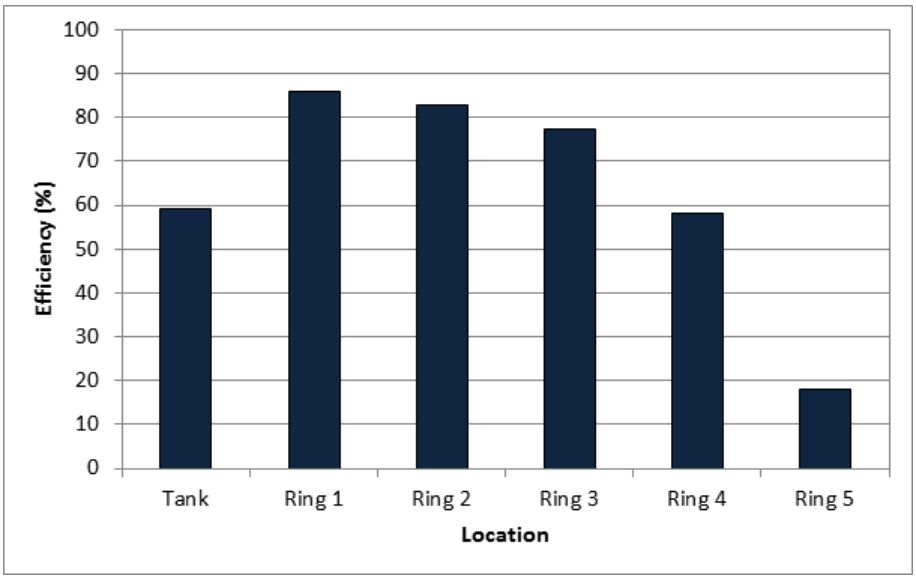

Figure 5.14: Efficiency for the base case by ring for Year 5

Figure 5.12 presents the amount of energy injected and extracted in Year 5 on a per ring basis. Figure 5.13 shows the average per borehole in the ring which is

required as each of the rings has a different number of boreholes. It is important to investigate the energy on a per ring basis since the losses primarily occur in the fifth ring. Essentially, the outermost ring acts to insulate the rest of the field from the uncharged ground around the field. Ring 1 extracts the most amount of heat, as expected, but it is also important to note that overall, rings 3 and 4 extract the bulk of the energy recovered. The fifth ring injects the most amount of energy, but most of it is lost to the surrounding ground.

Figure 5.14 also shows that the highest losses are in the outermost ring. There is a sharp decrease in efficiency from ring 4 to ring 5 (58% to 18%).

The energy injected and extracted for the whole field will be considered next.

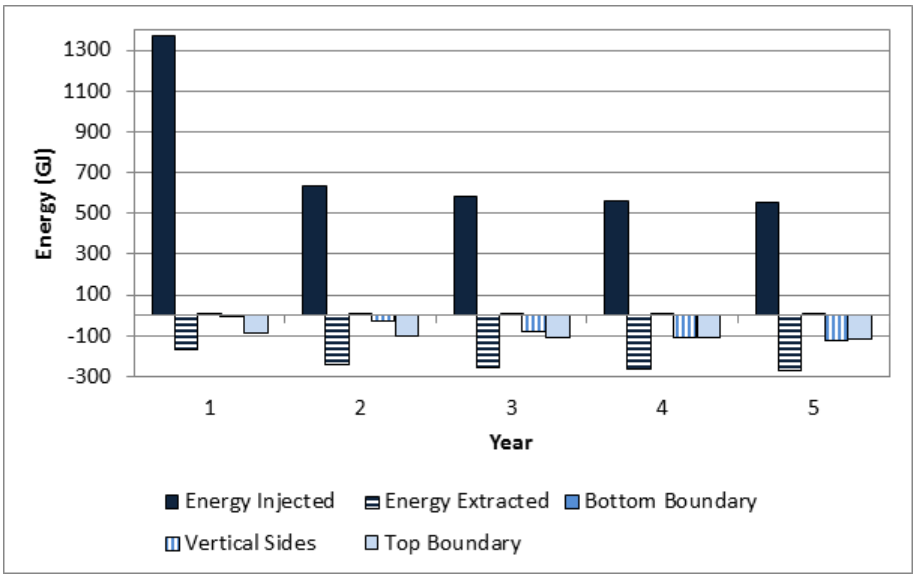

Figure 5.15: Energy injected and extracted for the base case over 5 years

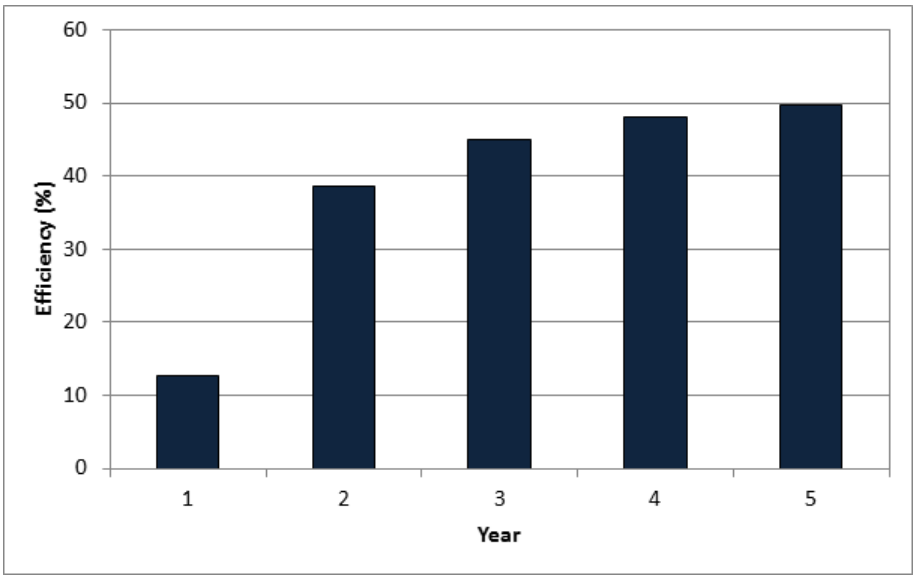

Figure 5.16: Efficiency of the base case over 5 years

Figure 5.15 presents the amount of energy injected and extracted per year through the boreholes. The figure also shows heat losses from the vertical and horizontal sides of the domain. These losses only account for energy entering and exiting the domain. A large portion of the energy injected by the boreholes is "lost" to the region outside the core region and is not recoverable, leading to reduced efficiencies. It can be observed that the largest amount of energy injection occurs in the first year. In the first year, the ground is at an uncharged temperature of 283 K, whereas the fluid temperature varies between 311 and 335 K, which results in a high heat flux/high energy injection and very little recovered energy. Subsequent years see higher temperatures, and Figure 5.6 shows that the temperature difference between the domain and boreholes is much smaller, resulting in the reduced heat injection.

From Figure 5.15, it can also be observed that a significant portion of the energy injected by the boreholes is being lost to the vertical sides and top of the domain and that there is a very small amount of energy injected through the bottom of the

domain. It is due to these factors that the energy extracted is much lower than what was injected.

Because of the high injection rate and low extraction, the efficiency is significantly lower in the first year, which can be observed in Figure 5.16 due to the initial charge from 283 K. The efficiency is increasing for the subsequent years, which indicates that the overall system has not yet reached steady state after 5 years, however, the differences between years is greatly diminishing after this point, so simulations were stopped there. The efficiency predicted in the fifth year is approximately 50%, which is comparable to the efficiency of 54% found at DLSC [5].

5.2.2 Impact of Losses on Tank Temperature

The tank in this study is not insulated. In order to ensure that the losses from the tank do not significantly impact the tank temperature, a simple energy balance was performed. The rate at which energy is added or extracted by flows entering of leaving the tank is given by:

$$\dot{Q} = \dot{m} C_p \Delta T = \rho \dot{V} C_P \Delta T \tag{5.7}$$

The properties of water at T=25°C are ρ=997 kg/m^3 and C$_p$=4181.7 J/kg·K. The STTS tanks at DLSC have a temperature difference between the entering and exiting water temperature of 20 K [39]. The average charging flow rate is 14 l/s, discharging is 6 l/s, minimum 2 l/s and they charge for roughly 12 hours a day [39].

$$\dot{Q}_{charge} = 997 \times \frac{14}{1000} \times 4187.7 \times 20 = 1167363\ J/s \doteq 50\ GJ/day \tag{5.8}$$

$$\dot{Q}_{discharge} = 997 \times \frac{6}{1000} \times 4187.7 \times 20 = 501016\ J/s \doteq 22\ GJ/day \tag{5.9}$$

Meanwhile, the maximum energy lost from the tank to the domain in a day is 0.26 GJ and the maximum energy gained by the tank from the domain in a day is 0.17 GJ. This corresponds to about 1% of the energy injected into the tank by the solar collectors.

This amount of energy will affect the temperature of the water as seen below.

$$Q = MC_p\Delta T = \rho V C_P \Delta T \tag{5.10}$$

$$\Delta T = \frac{Q}{\rho V C_P} = \frac{0.26 \times 10^9}{997 \times 7 \times 7 \times 5.5 \times 4187.7} = 0.023\ \text{K/day} \tag{5.11}$$

This results in a drop in tank temperature of 0.23 K which is insignificant.

5.2.3 Summary of Base Case

From the analysis of the Base Case, it was determined that the core region and soil plug temperatures reach a periodic sinusoidal temperature after about two years. The soil plug temperature sees more of a lag to the borehole temperatures as compared to the core region temperature, which can also be observed in the heat fluxes and energy into the soil plug. The losses out of the vertical sides of the domain increase as time progresses as the heat penetrates deeper into the uncharged ground every year. It was also observed that the innermost rings have a higher efficiency. The outermost ring has a significantly reduced efficiency compared to the others, which is due to the

uncharged ground directly adjacent to it. The overall efficiency of the system ranges from around 40-50% (excluding the initial charging year, as there are high losses). The losses from the tank into the field are small compared to the energy added to the tank by the solar collectors, which shows that energy loss from the tank does not significantly reduce the tank temperature.

The base case is fairly simple, but the effect of the number of rings, insulation on the tank, stratification within the tank and within the borehole field, tank aspect ratio and soil type all need to be investigated.

5.3 Alternate Geometries

In order to isolate and analyze the impact of the water tank on the borehole field, two simulations were carried out. The two simulations, referred to as the "No Tank" and "Typical BTES" and are described below.

The "No Tank" case is identical to the base case, with the removal of the tank in the centre. Essentially, it consists of five rings of boreholes with a gap in the centre where the tank would otherwise be. Removing the tank allows for the effect of the water tank on the "soil plug" to be isolated.

The "Typical BTES" case had four additional boreholes in the centre of the field. This is the typical borehole field layout, similar to the one at DLSC, seen in Figure 5.17, and the change in efficiency due to the tank's presence must be determined. It must be noted that the surface area of the tank is 207 m^2, and the surface area of the boreholes it replaces is 227 m^2, so they are of comparable surface area.

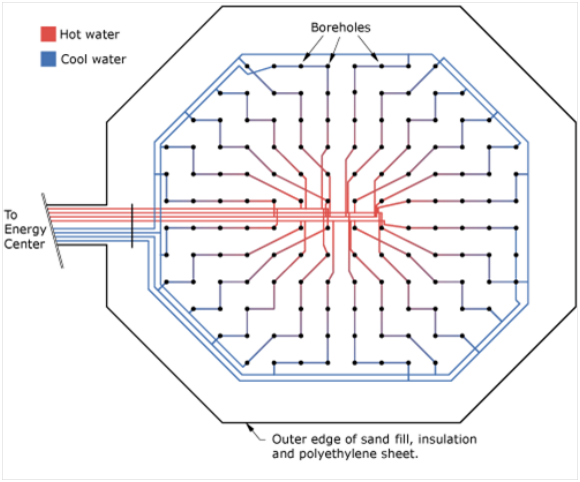

Figure 5.17: Top view of borehole field at Drake Landing Solar Community [5]

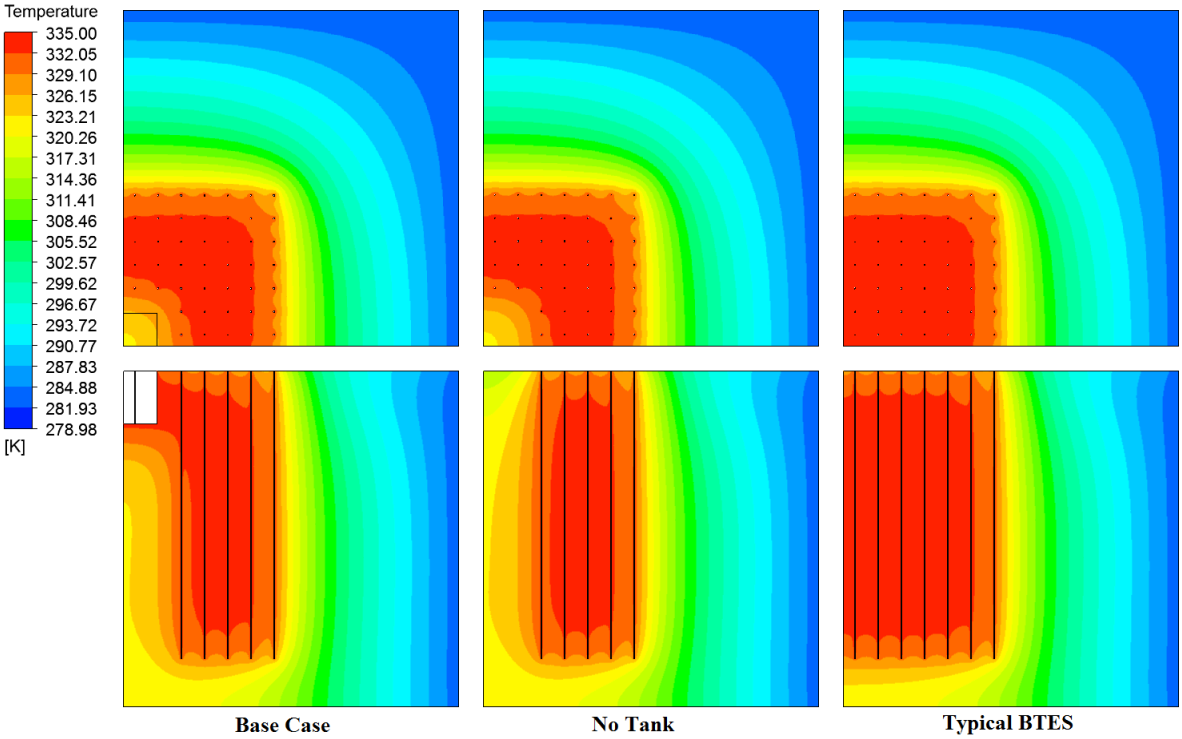

Figure 5.18: Temperature contours for the different geometries at a fully charged state (1590 days) for the side view (plane containing boreholes, z=1.16 m) and top view (borehole half length, y=-15 m)

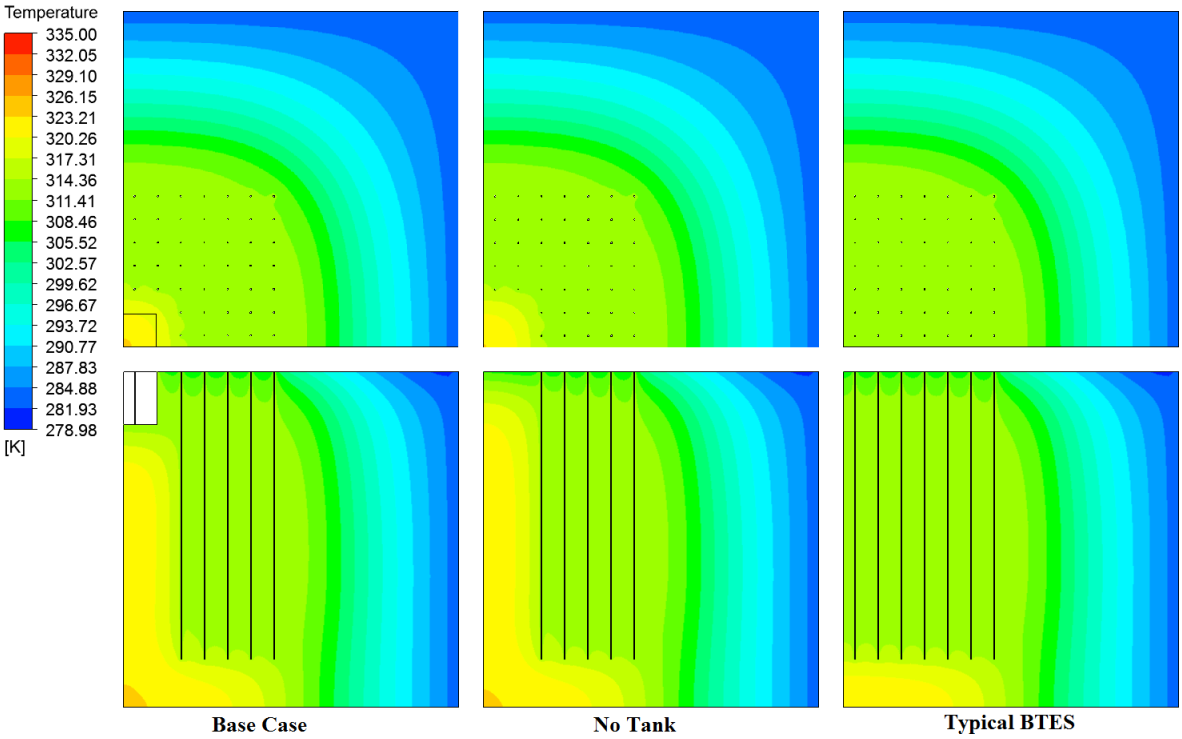

Figure 5.19: Temperature contours for the different geometries at a fully discharged state (1770 days) for the side view (plane containing boreholes, z=1.16 m) and top view (borehole half length, y=-15 m)

Figures 5.18 and 5.19 show the temperature contours for the three geometries under consideration. The Base Case and No Tank case both have a gap in the centre that is not reaching as high a temperature during charging, nor is it dropping to as low a temperature during discharging as compared to the Typical BTES. This shows that while energy can be recovered from this region, the full thermal storage capacity of the soil plug is not exploited. In Figure 5.19, there is a small pocket of hot soil at the bottom left of the domain for the Base Case and No Tank that cannot be recovered. This is an artifact of the simulation, since in a practical application this heat would be lost to the soil below the domain shown. If the domain was deeper, this energy would be dissipated.

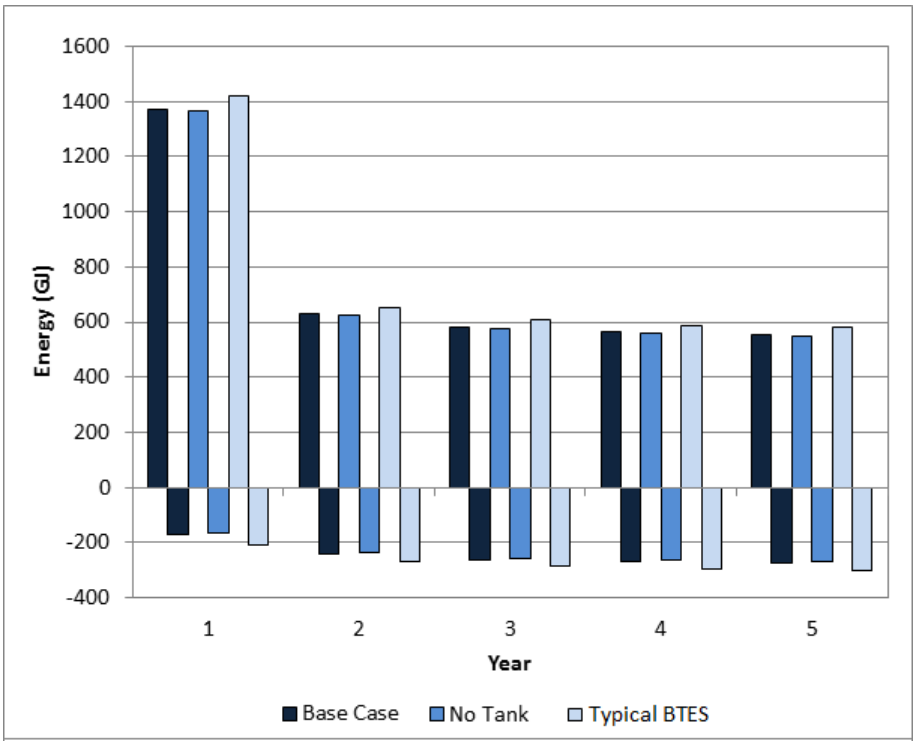

Figure 5.20: Energy injected into and extracted from the borehole field over 5 years

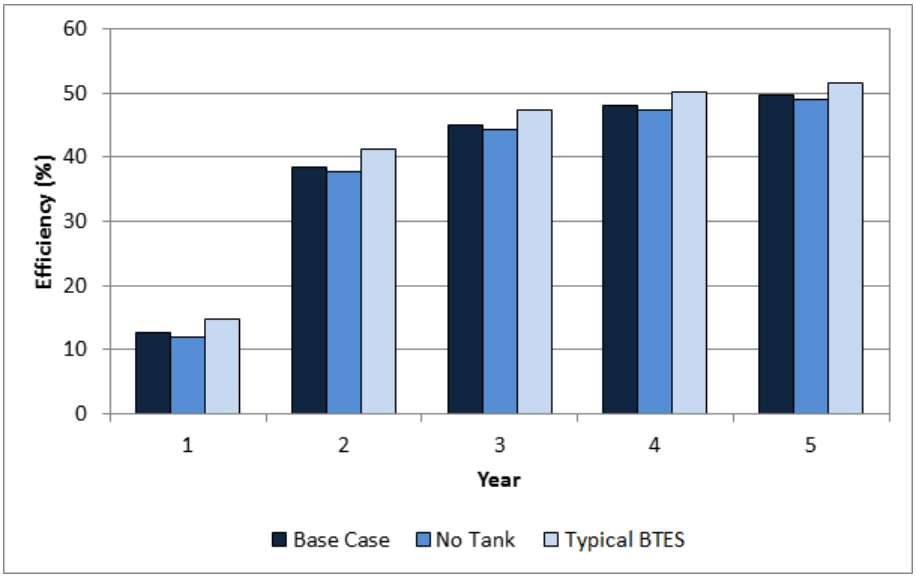

Figure 5.21: Efficiency of the alternate geometries over 5 years

Case	Surface Area (m^2)	% Increase in Surface Area	Year 5 Efficiency	% Increase in Year 5 Efficiency
Base Case	687.55	N/A	49.62	N/A
No Tank	636.80	-7.38	48.93	-1.40
Typical BTES	693.40	0.85	51.57	3.92

Table 5.1: Comparison of efficiencies based on surface area of tank and boreholes

Case	Energy Injected (GJ)	Energy Extracted (GJ)	Efficiency
Base Case	553.95	-274.89	49.62
No Tank	549.31	-268.77	48.93
Typical BTES	580.32	-299.25	51.57

Table 5.2: Year 5 data for alternate geometries

Figures 5.20 and 5.21 show the energy transferred to and from the borehole field and the corresponding efficiencies, respectively. Table 5.2 shows the values for energy and efficiency in year five. The Typical BTES case outperforms the other two scenarios. This is to be expected since the central boreholes are highly efficient at penetrating the core of the field. However, the difference in performance of the three cases is relatively small. The No Tank case is the poorest performer, but since it has the smallest heat transfer surface area, as seen in Table 5.1, that is to be expected. Putting a tank in the centre of a borehole field results in a drop in efficiency by around 3%. From the discussion of efficiency based on borehole ring from the previous section, it was established that the rings at the centre of the field have the

highest efficiency. If the innermost ring is replaced by a tank, some of the efficiency is lost. This loss may be justified if the tank performance is enhanced compared to a tank placed on the surface of the ground, since the buried tank is able to recover much of the energy that it loses to the ground.

5.4 Effect of Number of Borehole Rings

In order to assess the impact of the surface area to volume ratio of the borehole field, simulations were carried out with fewer rings of boreholes.

The first simulation considers 5 boreholes in a single ring around the same tank as in the base case. The domain size is smaller in the cross-section, due to the smaller size of the borehole field (17.5 m by 17.5 m as compared to 35 m by 35 m), but the depth of the of the domain remains the same at 35 m deep. This is referred to as the "1 Ring" case.

The second simulation considers of 12 boreholes in 2 rings around the same tank as in the base case. It has the same domain dimensions as the 1 ring case.

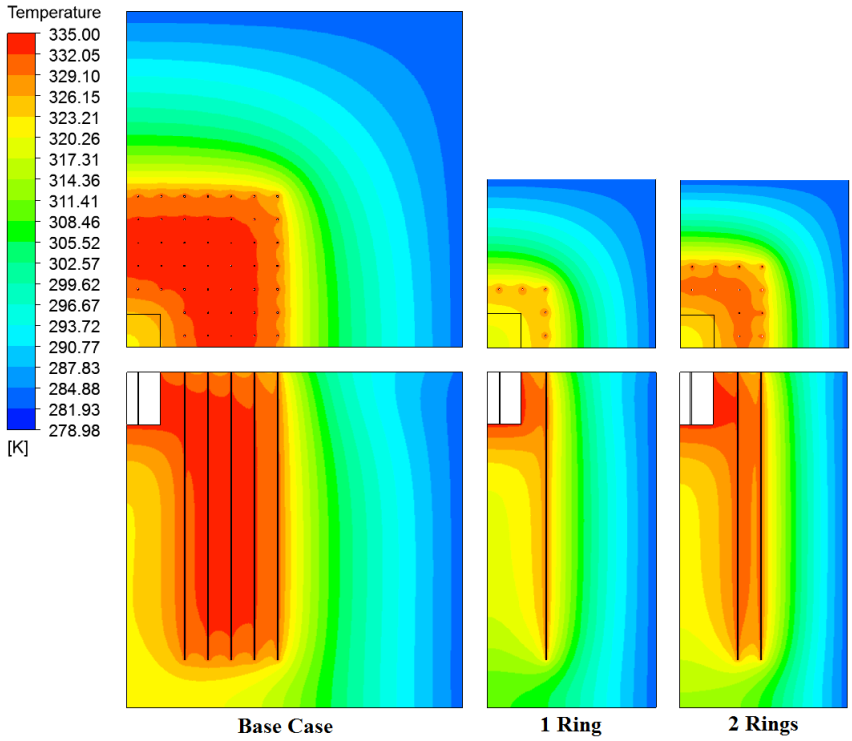

Figure 5.22: Temperature contours for the different number of rings at a fully charged state (1590 days) for the side view (plane containing boreholes, z=1.16 m) and top view (borehole half length, y=-15 m)

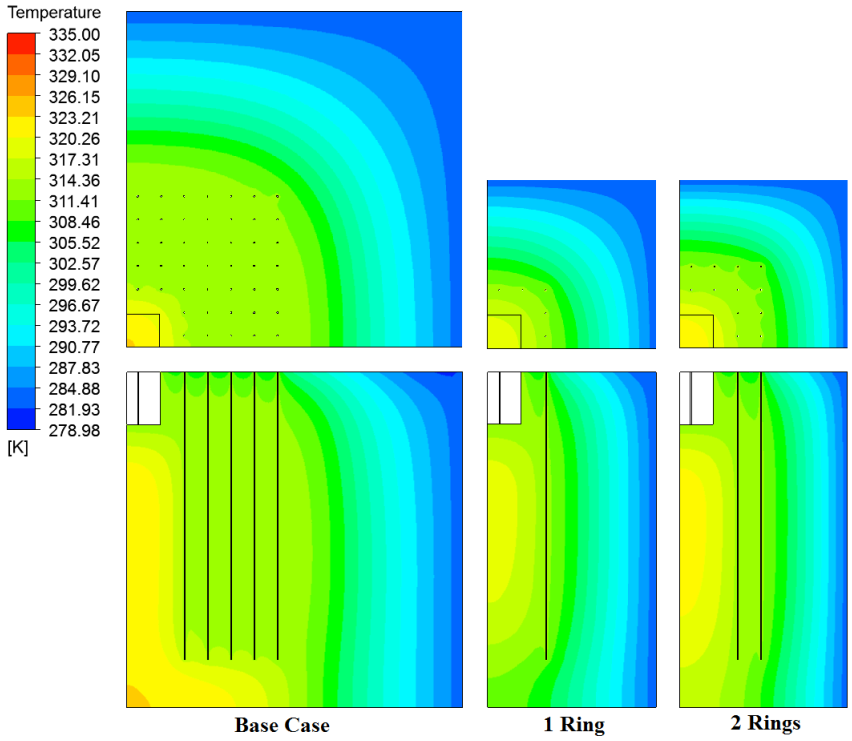

Figure 5.23: Temperature contours for the different number of rings at a fully discharged state (1770 days) for the side view (plane containing boreholes, z=1.16 m) and top view (borehole half length, y=-15 m)

From Figures 5.22 and 5.23, it is apparent that the soil plug is hottest for the Base Case and coldest for the 1 Ring case. The addition of more rings also ensures the soil between the boreholes reaches a hotter temperature, which is critical since it then increases the temperature difference between the soil and the boreholes' discharging temperature. The percentage of losses to the environment is also higher for the 1 Ring and 2 Rings cases as compared to the Base Case.

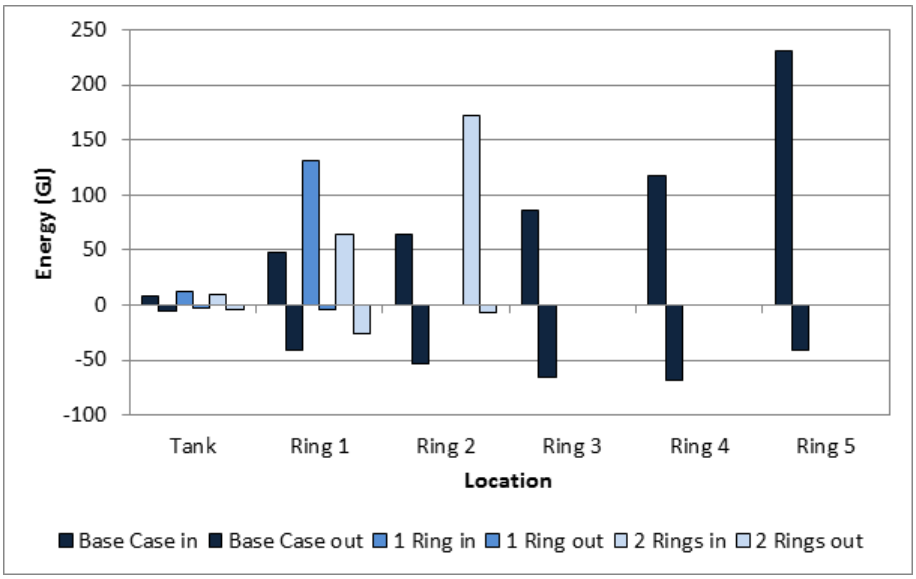

Figure 5.24: Energy injected and extracted based on number of rings by ring for Year 5

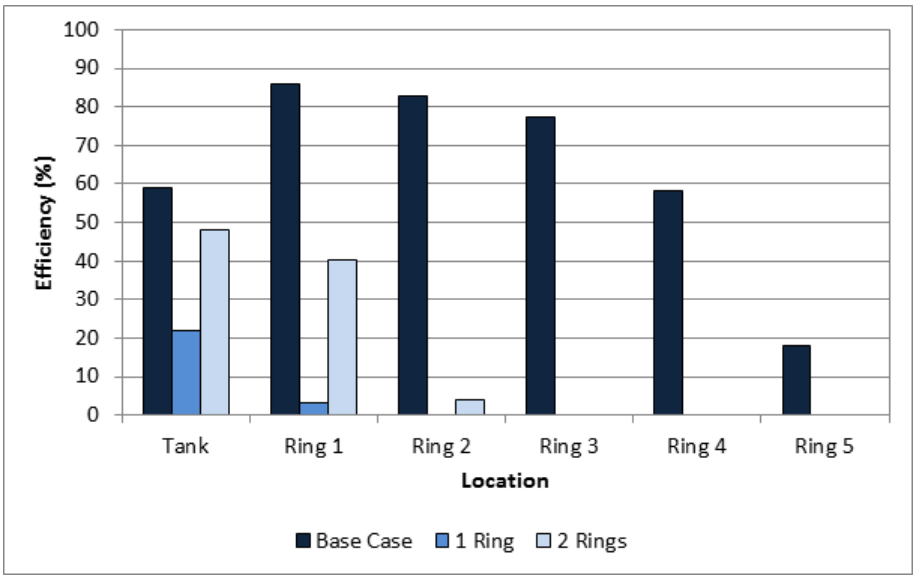

Figure 5.25: Efficiency based on number of rings by ring for Year 5

Figure 5.24 presents the energy injected and extracted on a per borehole ring basis and Figure 5.25 presents the corresponding efficiency. From these two graphs, it can

be seen that the outermost ring has a much lower efficiency compared to the inner rings. Essentially, the outermost ring acts to insulate the interior boreholes.

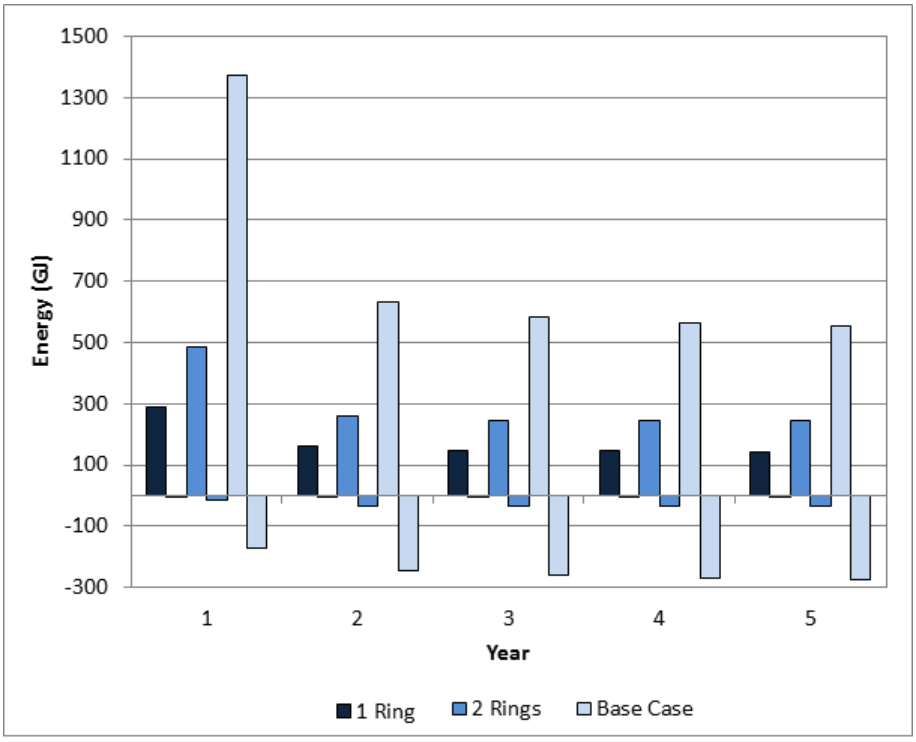

Figure 5.26: Energy injected and extracted based on the number of rings over 5 years

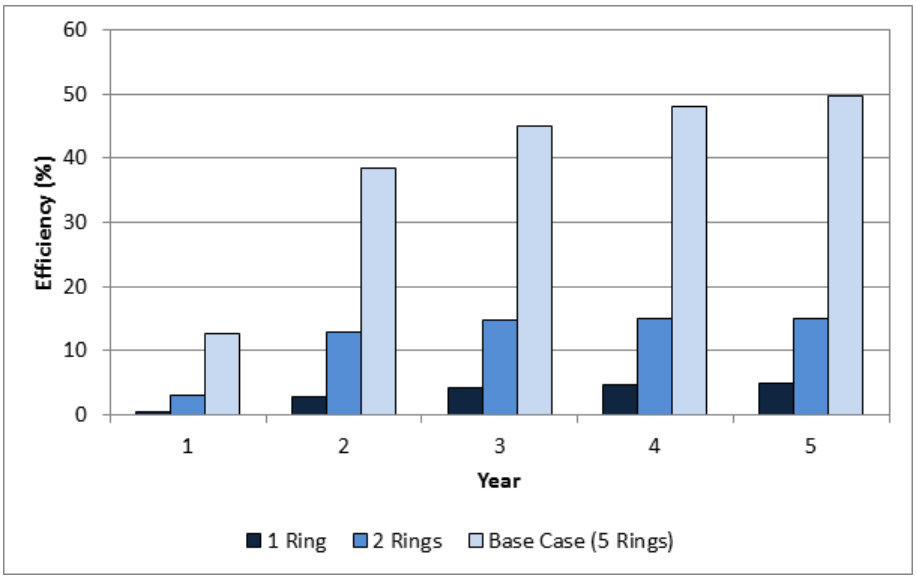

Figure 5.27: Efficiency based on the number of rings over 5 years

Case	Surface Area (m^2)	% Increase in Surface Area	Year 5 Efficiency	% Increase in Year 5 Efficiency
Base Case	687.55	N/A	49.62	N/A
1 Ring	121.51	-82.33	4.87	-90.18
2 Rings	220.56	-67.92	15.06	-69.65

Table 5.3: Comparison of efficiencies based on surface area of tank and boreholes

Case	Energy Injected (GJ)	Energy Extracted (GJ)	Efficiency
Base Case	553.95	-274.89	49.62
1 Ring	143.65	-7.00	4.87
2 Rings	244.92	-36.89	15.06

Table 5.4: Year 5 data for number of rings

Table 5.3 shows the increase in efficiency based on increased surface area and it can be observed that the efficiency increases with increased surface area. Table 5.4 shows the values for energy and efficiency in year five. While it is unsurprising that the 1 Ring and 2 Rings cases both perform worse than the Base Case, it becomes evident from Figure 5.27 that their efficiencies are much lower, to the point where they may be infeasible.

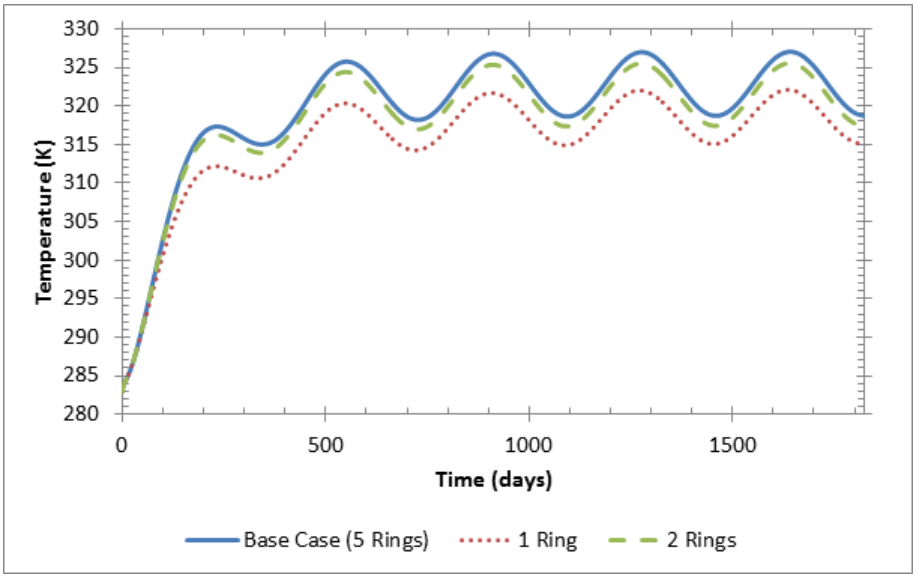

Figure 5.28: Temperature transients of the soil plug based on the number of rings over 5 years

Figure 5.28 shows the soil plug temperature for the three cases. Due to the high

losses to the outer regions of the domain for the 1 Ring case, the soil plug temperature is much lower than the other two. However, the 2 Rings case compares quite similarly to the Base Case. This indicates that even the addition of one extra ring around the tank has a significant impact on the soil plug.

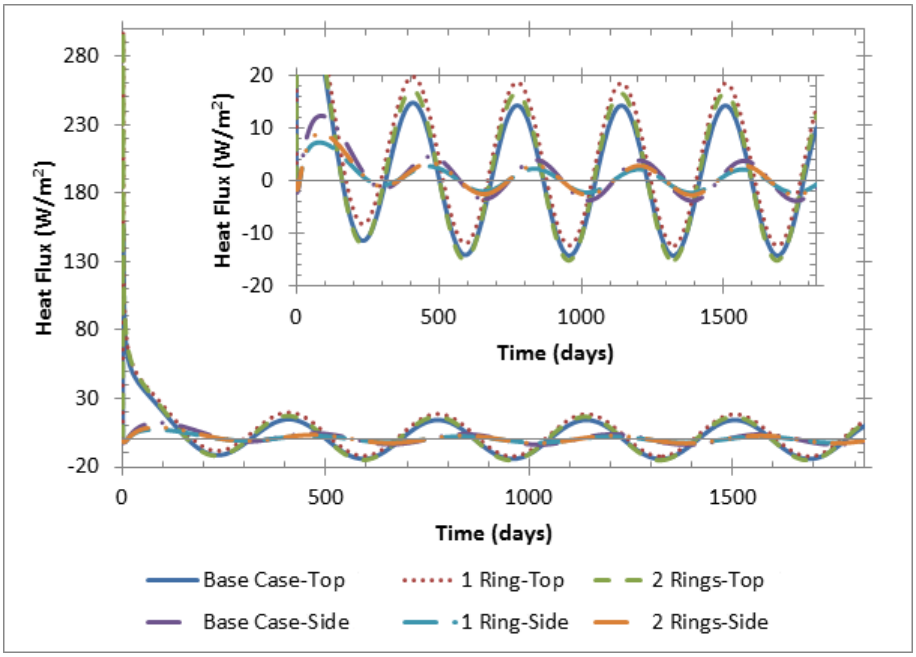

Figure 5.29: Heat fluxes to the soil plug based on the number of rings over 5 years

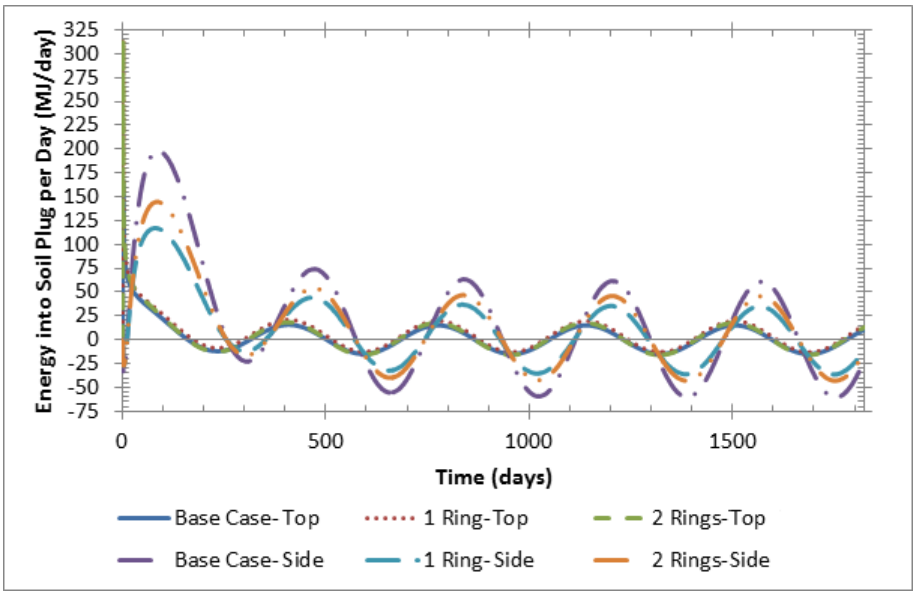

Figure 5.30: Energy injected and extracted from the soil plug based on the number of rings over 5 years

From Figure 5.29, it can be observed that the Base Case has the highest plug side heat flux, and lowest plug top heat flux, and vice versa for the 1 Ring case. This trend also applies to Figure 5.30. This combined with the soil plug temperature implies that the fewer rings a field has, the greater the losses, and therefore the lower the energy stored within the soil plug. This also suggests that it would be more advantageous to bury a tank within a larger field since the surface area to volume ratio for the borehole field decreases with increasing diameter of the borehole field, thus reducing losses.

5.5 Radial Stratification

DLSC has radial stratification within its borehole field as a means of improving efficiency. Radial stratification is sectioning of the borehole field such that the hottest

fluid starts in the centre and slowly cools as it moves outwards through the string. This leads to smaller temperature differences between the outermost ring and the adjacent uncharged ground, reducing heat losses and improving efficiency. In order to mimic radial stratification different sinusoidal waves were applied to different rings of boreholes. Two different cases were run: one based on DLSC data and one with a weighted average based on borehole area. The two cases do not have the same overall average temperature.

5.5.1 DLSC Radial Stratification

For this simulation, the temperature transients at each of the sensors at DLSC for the year of July 2011 to June 2012 were set for each ring of boreholes. The temperature readings from the innermost sensor was set as the tank temperature, and each subsequent sensor was applied to the following rings.

Tank:

$$T_{bh} = 11.5sin\left(\frac{2\pi t}{365}\right) + 330 \tag{5.12}$$

Ring 1:

$$T_{bh} = 11sin\left(\frac{2\pi t}{365}\right) + 327.5 \tag{5.13}$$

Ring 2:

$$T_{bh} = 11sin\left(\frac{2\pi t}{365}\right) + 325 \tag{5.14}$$

Ring 3:

$$T_{bh} = 11sin\left(\frac{2\pi t}{365}\right) + 321.5 \tag{5.15}$$

Ring 4:

$$T_{bh} = 11sin\left(\frac{2\pi t}{365}\right) + 318.5 \tag{5.16}$$

Ring 5:

$$T_{bh} = 11sin\left(\frac{2\pi t}{365}\right) + 316 \tag{5.17}$$

5.5.2 Weighted Average Radial Stratification

The temperature transients were established by calculating a weighted average temperature based on surface area, with the highest temperature in the centre and decreasing by a few degrees for each of the subsequent rings. The weighted average of these transients is the same as the Base Case. The sine waves applied were as follows:

Tank:

$$T_{bh} = 12sin\left(\frac{2\pi t}{365}\right) + 332 \tag{5.18}$$

Ring 1:

$$T_{bh} = 12sin\left(\frac{2\pi t}{365}\right) + 331 \tag{5.19}$$

Ring 2:

$$T_{bh} = 12sin\left(\frac{2\pi t}{365}\right) + 328 \tag{5.20}$$

Ring 3:

$$T_{bh} = 12sin\left(\frac{2\pi t}{365}\right) + 325 \tag{5.21}$$

Ring 4:

$$T_{bh} = 12sin\left(\frac{2\pi t}{365}\right) + 321 \tag{5.22}$$

Ring 5:

$$T_{bh} = 12sin\left(\frac{2\pi t}{365}\right) + 315 \tag{5.23}$$

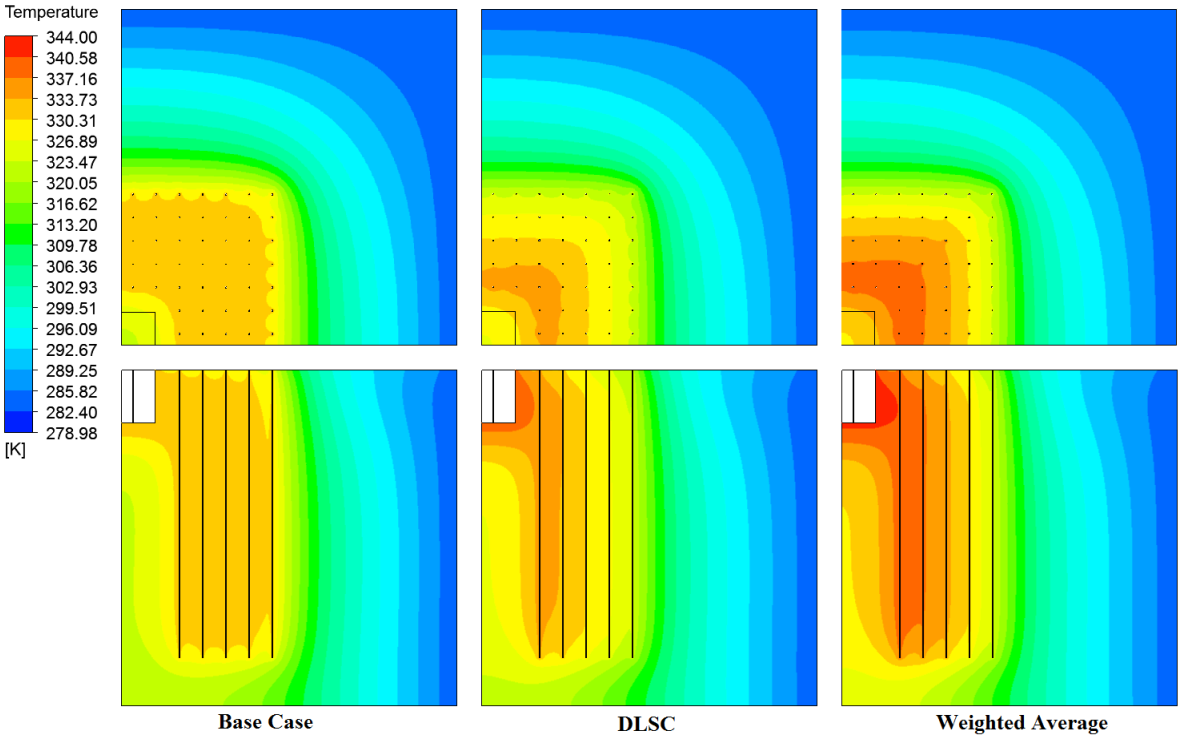

Figure 5.31: Temperature contours for radial stratification at a fully charged state (1590 days) for the side view (plane containing boreholes, z=1.16 m) and top view (borehole half length, y=-15 m)

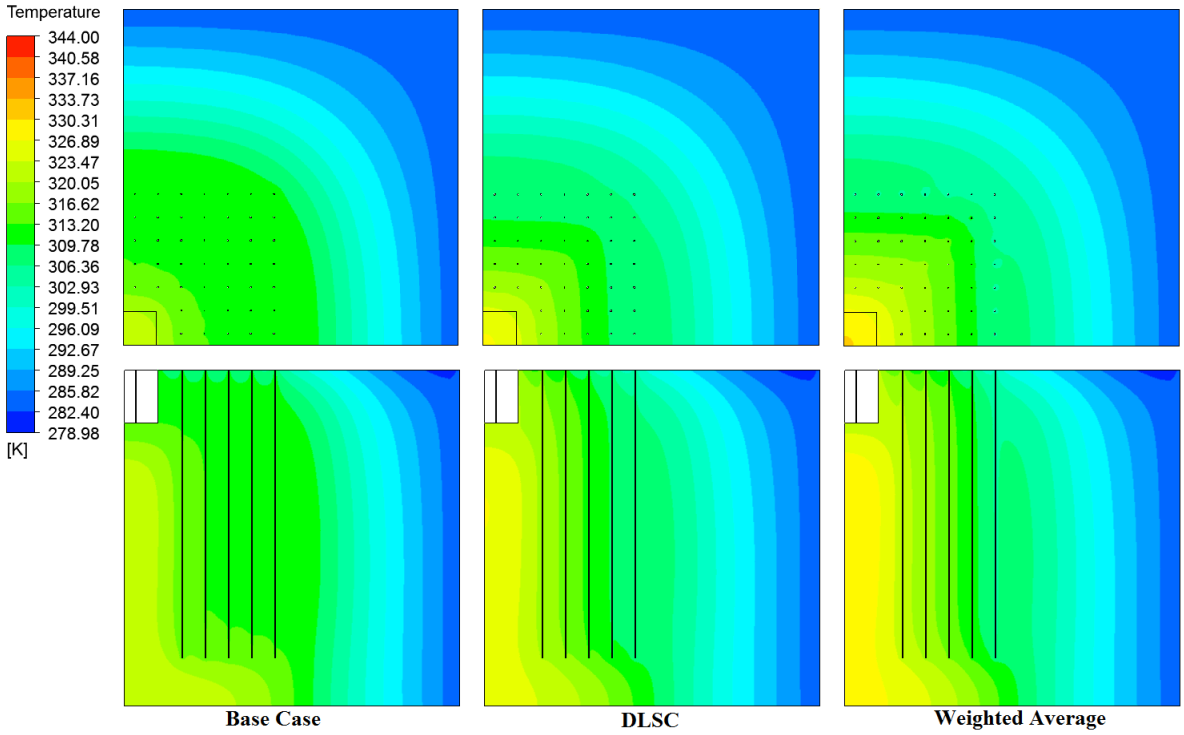

Figure 5.32: Temperature contours for radial stratification at a fully discharged state (1770 days) for the side view (plane containing boreholes, z=1.16 m) and top view (borehole half length, y=-15 m)

The effect of radial stratification can be observed in Figures 5.31 and 5.32. The innermost rings for both the DLSC case and the Weighted Average case are hottest and the radial temperature gradient can be seen clearly.

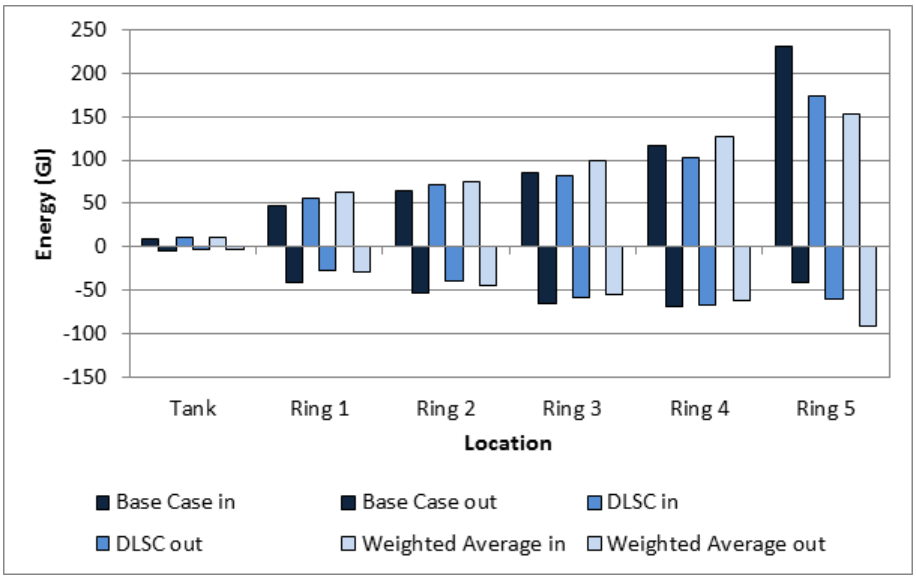

Figure 5.33: Energy injected and extracted for radial stratification by ring for Year 5

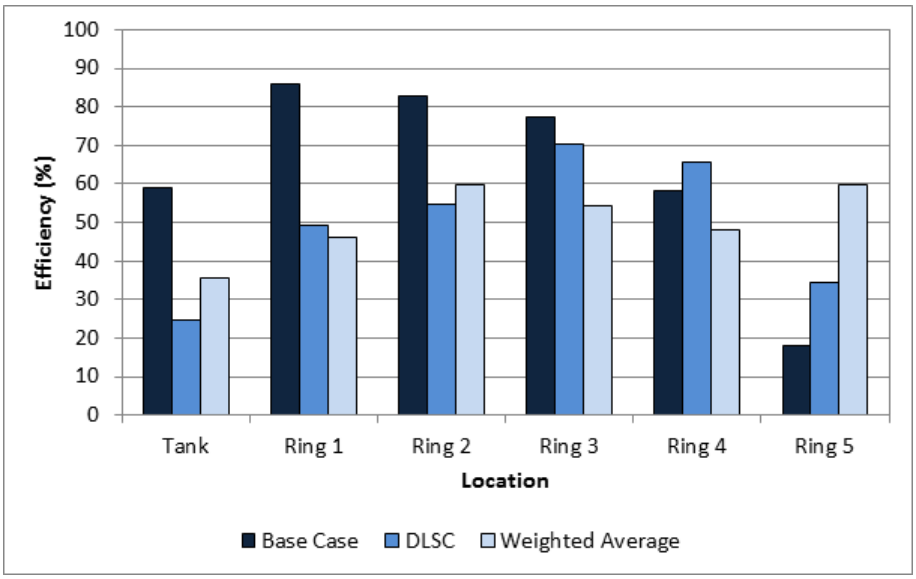

Figure 5.34: Efficiency for radial stratification by ring for Year 5

From Figure 5.33, it can be observed that the all three cases have similar amounts of energy injected and extracted, with the exception of in ring 5. Figure 5.34 depicts the corresponding efficiencies, which show that the Base Case has a higher efficiency

in the innermost rings, and the Weighted Average cases has the highest efficiency in the outermost rings and in general has a more uniform efficiency. Because ring 5 contains the most boreholes, a small increase in efficiency in this ring can lead to a higher overall efficiency for the field.

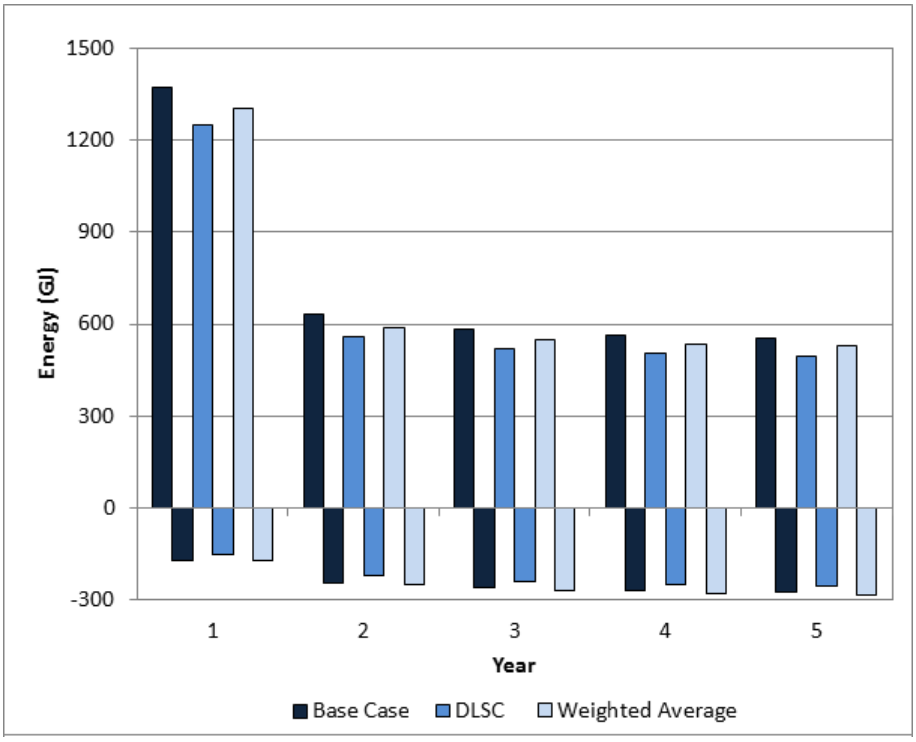

Figure 5.35: Energy injected and extracted for radial stratification over 5 years

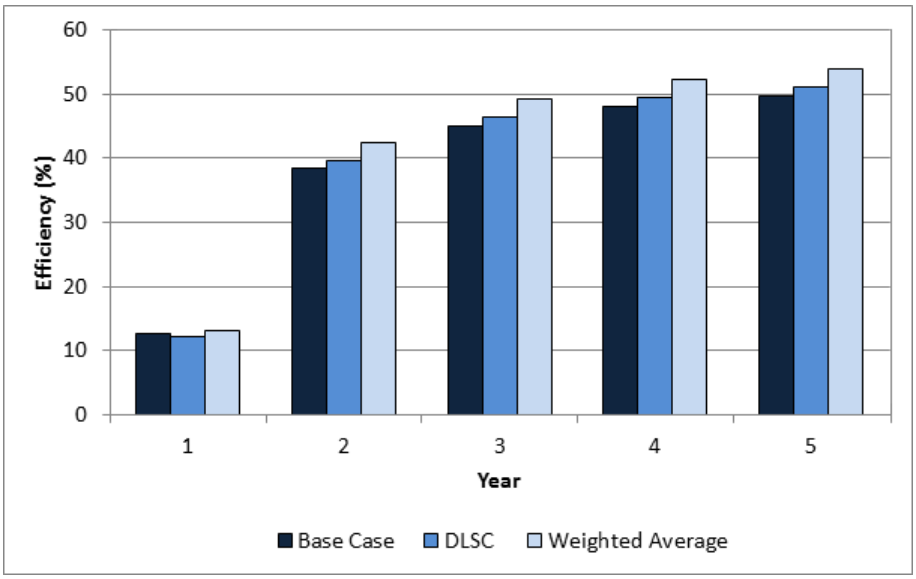

Figure 5.36: Efficiency of radial stratification over 5 years

Figure 5.35 shows that the Base Case injects the most amount of energy out all three cases, but that the Weighted Average case extracts the most. This leads to the Weighted Average case having the highest efficiency, which can be observed in Figure 5.36.

Case	Energy Injected (GJ)	Energy Extracted (GJ)	Efficiency
Base Case	553.95	-274.89	49.62
DLSC	495.51	-253.16	51.09
Weighted Average	527.53	-283.85	53.81

Table 5.5: Year 5 data for radial stratification

Table 5.5 shows the values for energy and efficiency in year five. Though the

Base Case injects the most energy out of the three cases, it generally has the lowest efficiency. For both of the cases with radial stratification, the rings further out have lower temperatures, and so they have a smaller temperature difference with the undisturbed ground, therefore leading to smaller losses and higher efficiencies. Note that while the average temperature for both the Base Case and the Weighted Average cases were the same, the latter has a higher efficiency. This highlights the importance of radially stratifying borehole fields where possible, as a greater portion of the energy can be recovered.

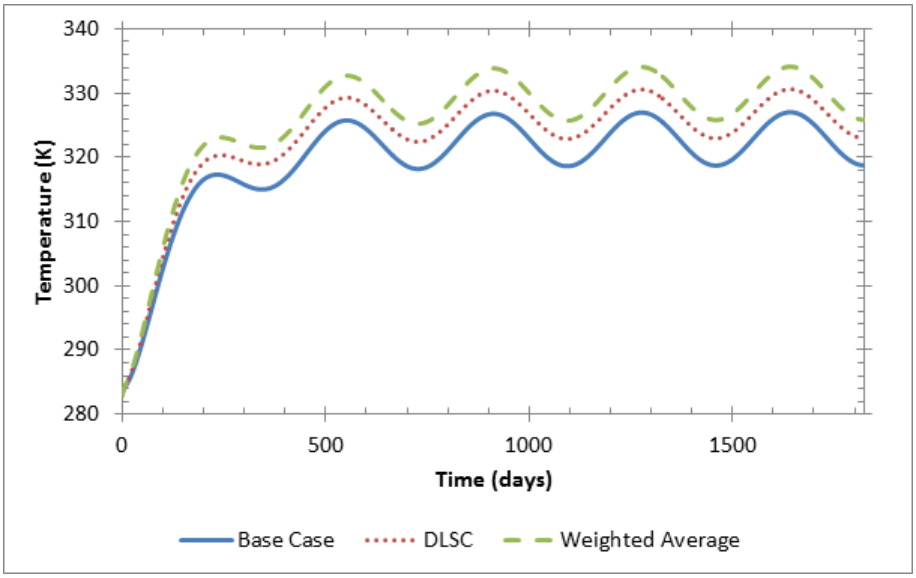

Figure 5.37: Temperature transients of the soil plug over 5 years for the study of radial stratification

Figure 5.37 depicts the temperatures of the soil plugs for all three cases. Since the boreholes near the centre of the field are hottest for the stratified cases, the soil plug gains more energy and is hotter than in the Base Case. As expected, the hotter the innermost ring, the higher the temperature in the soil plug.

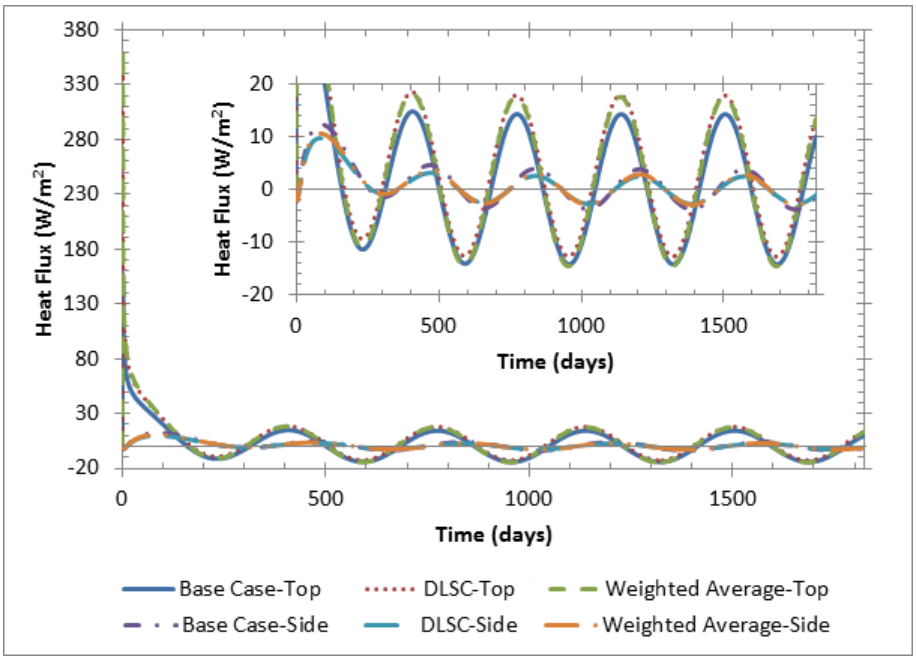

Figure 5.38: Heat fluxes to the soil plug for radial stratification over 5 years

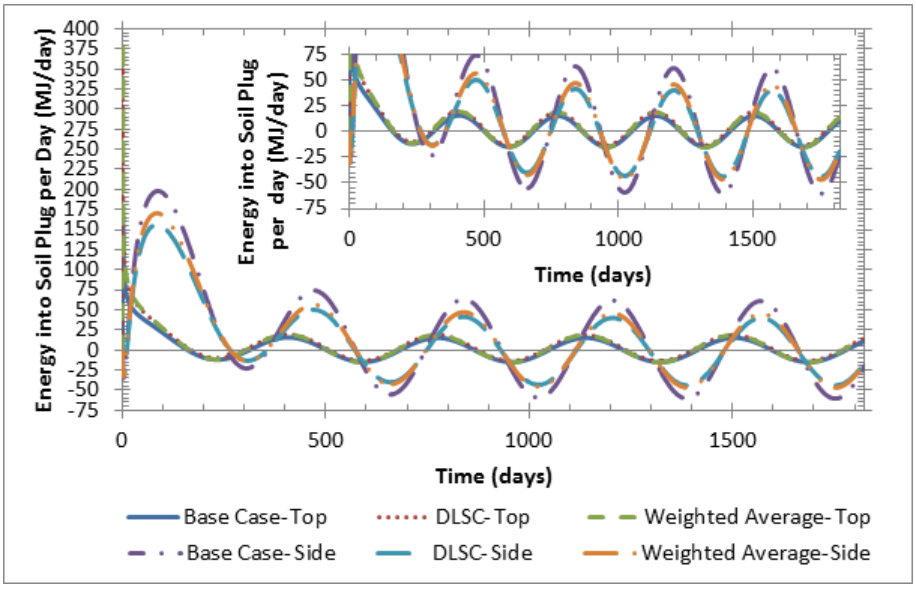

Figure 5.39: Energy injected and extracted from the soil plug for radial stratification over 5 years

Figure 5.38 shows that both forms of radial stratification have similar heat fluxes

at the soil plug boundaries. However, Figure 5.39 shows that the Weighted Average Radial Stratification case has a slightly higher energy injection from the plug sides. Because the innermost ring is hotter for the Weighted Average case as compared to the DLSC, it results in a hotter soil plug for the Weighted Average case.

5.6 Effect of Insulating the Bottom of the Tank

For this simulation, the bottom surface of the tank was set to be adiabatic to model a tank with insulation on the bottom. This allows for the study of the soil plug under a case with some insulation.

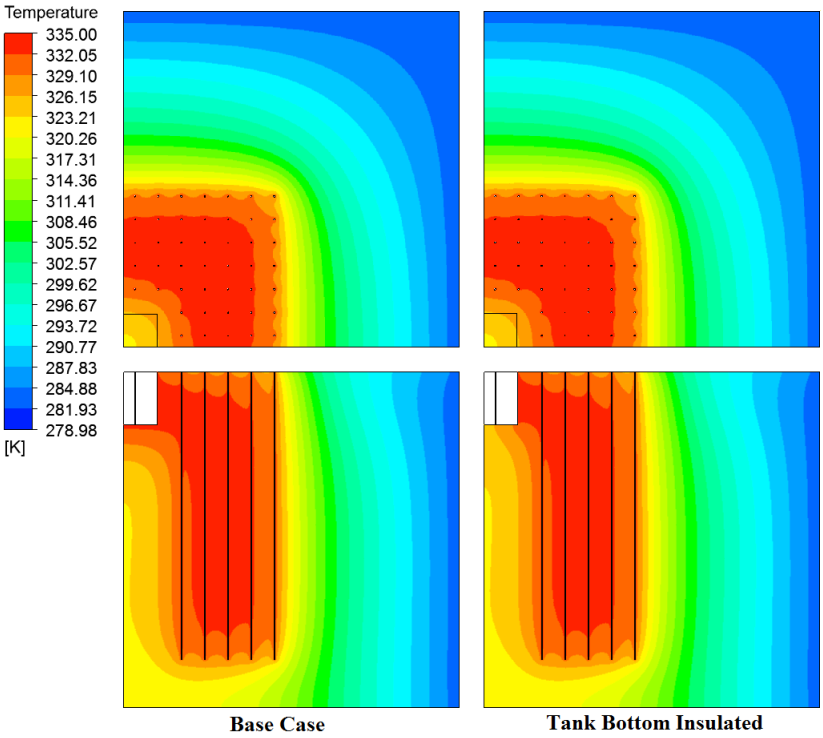

Figure 5.40: Temperature contours for the tank bottom insulated case at a fully charged state (1590 days) for the side view (plane containing boreholes, z=1.16 m) and top view (borehole half length, y=-15 m)

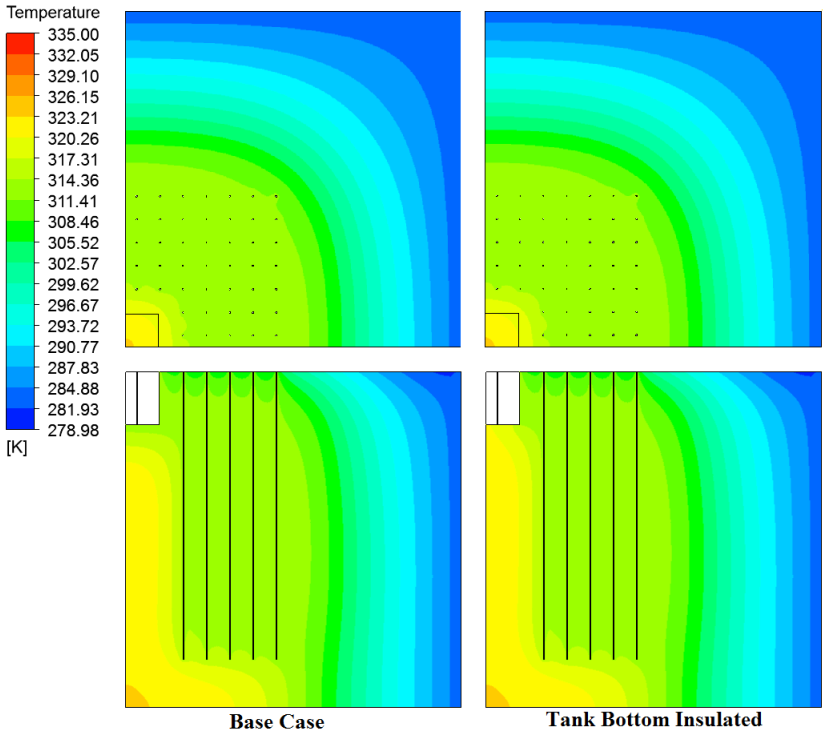

Figure 5.41: Temperature contours for the tank bottom insulated case at a fully discharged state (1770 days) for the side view (plane containing boreholes, z=1.16 m) and top view (borehole half length, y=-15 m)

Figures 5.40 and 5.41 show that the differences between the Base Case and the Tank Bottom Insulated case are primarily in the region below the tank. The adiabatic surface causes the contours under the tank to be perpendicular to the bottom of the tank, which can be seen more clearly in Figure 5.42. Moreover, the insulation causes the isotherms to change directions and the region directly under the tank (within 2 m of the tank bottom) is colder with insulation than without. However, this is not significant enough to change the overall soil plug temperature.

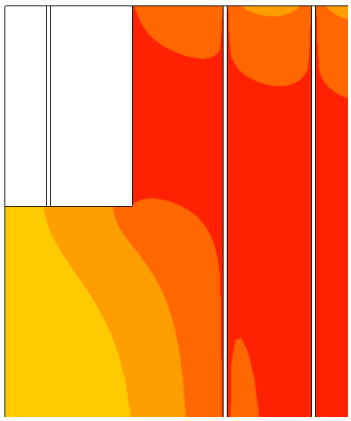

Figure 5.42: Close-up view of the temperature contour for the tank bottom insulated case at a fully charged state (1590 days)

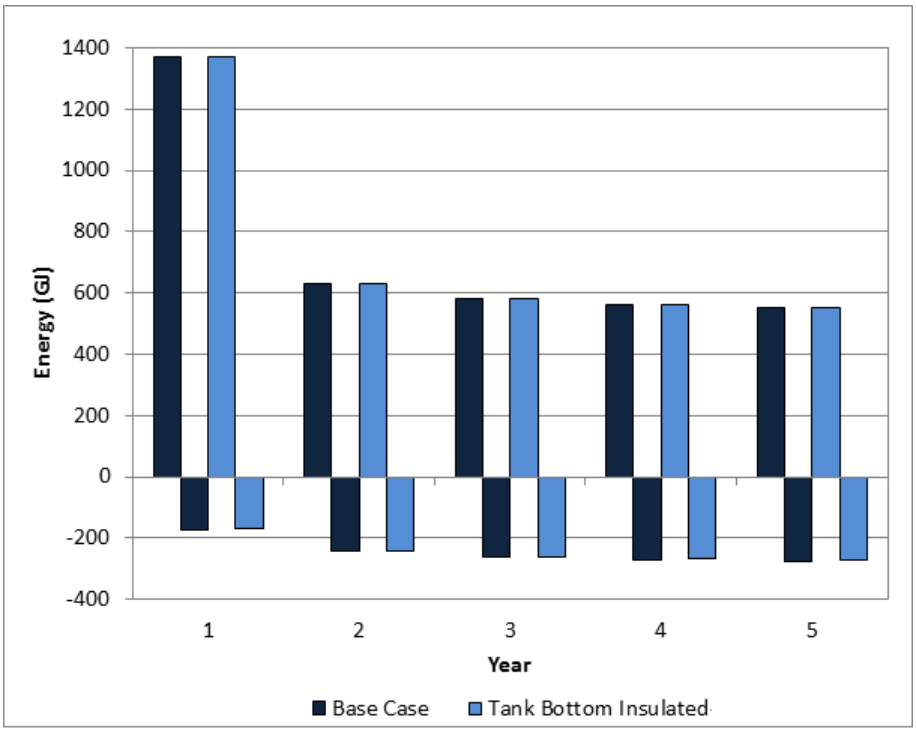

Figure 5.43: Energy injected and extracted for the tank bottom insulated case over 5 years

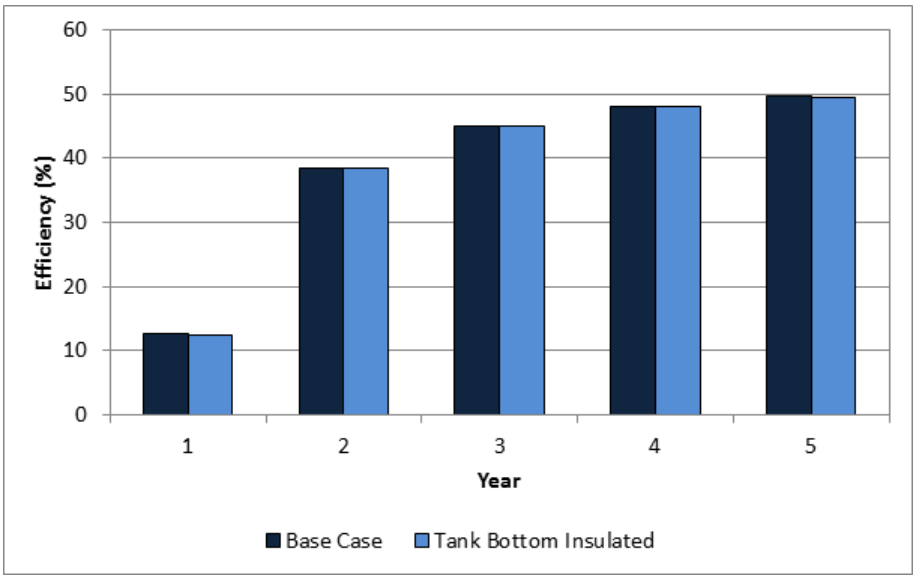

Figure 5.44: Efficiency of the tank bottom insulated case over 5 years

Case	Energy Injected (GJ)	Energy Extracted (GJ)	Efficiency
Base Case	553.95	-274.89	49.62
Bottom Insulated	552.02	-273.26	49.50

Table 5.6: Year 5 data for the tank bottom insulated case

From Figures 5.43 and 5.44 and Table 5.6, it can be observed that the predictions are nearly identical for this case and the Base Case. The Tank Bottom Insulated case injects a slightly smaller amount of energy into the domain, but the efficiencies remain roughly the same for both simulations.

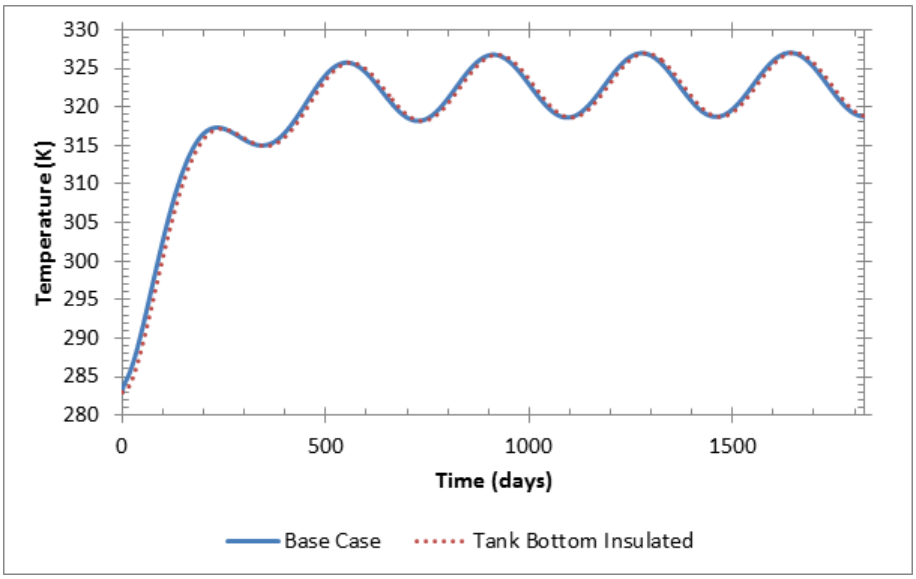

Figure 5.45: Temperature transients of the soil plug of the tank bottom insulated case over 5 years

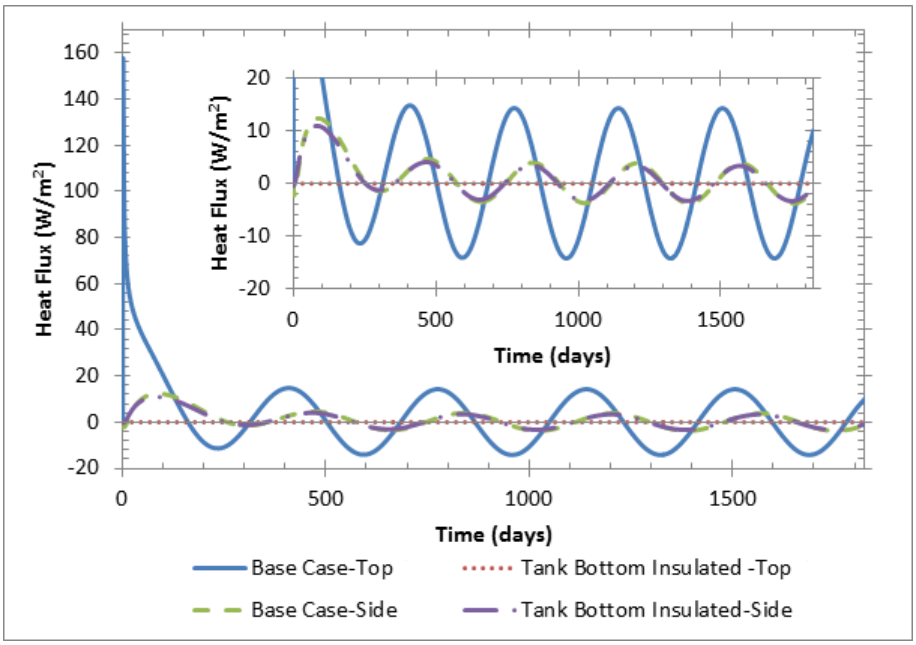

Figure 5.46: Heat fluxes to the soil plug for the tank bottom insulated case over 5 years

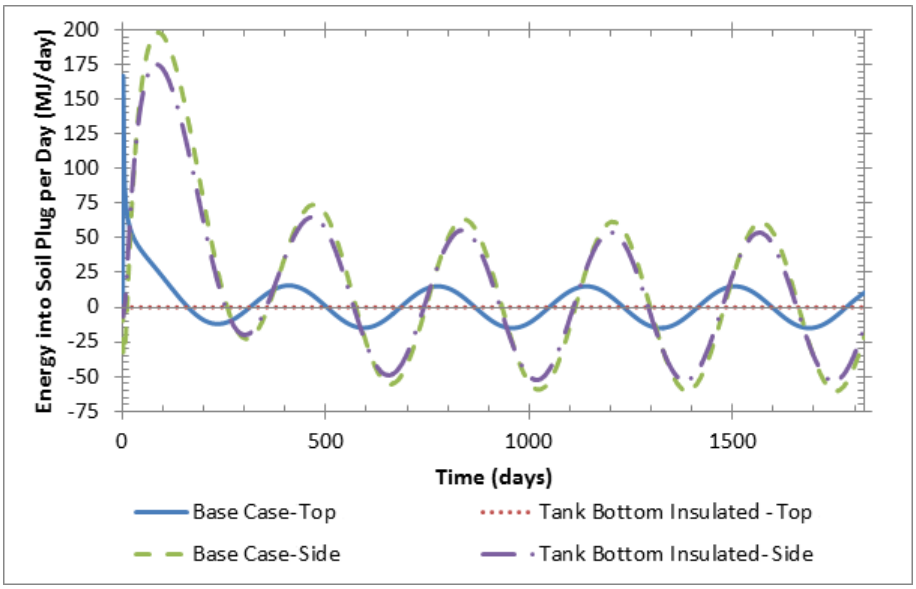

Figure 5.47: Energy injected and extracted from the soil plug for the tank bottom insulated case over 5 years

In Figure 5.45, it can be observed that there is a very small effect on the soil plug temperature. While it has been established that the top of the plug has a higher heat flux than through the sides in the Base Case, as seen in Figure 5.46, the larger area of the sides causes far more heat to be injected through them. Figure 5.47 shows that the energy injected through the top of the Base Case is small, so even though the Tank Bottom Insulated case has no energy injected through the plug top, there is not a significant difference between the two simulations. The Base Case has slightly higher energy injected through the sides of the soil plug, but that is likely due to the smaller amount of energy injected into the overall domain.

5.7 Tank Stratification

Another consideration in this study is the effect of stratification within the tank. Tank stratification is important as it improves the system efficiency by ensuring the hottest water is discharged to the user, and the coldest water is sent to the solar collectors. This will need to be investigated further as future work to determine the impact of the boreholes on the fluid within the tank, but a preliminary analysis of tank stratification on the borehole field has been performed.

The tank was split into two sections. The top half of the tank had the same temperature transient as the Base Case while the bottom half of the tank was 20 degrees colder, which is the temperature rise across the solar collectors [39].

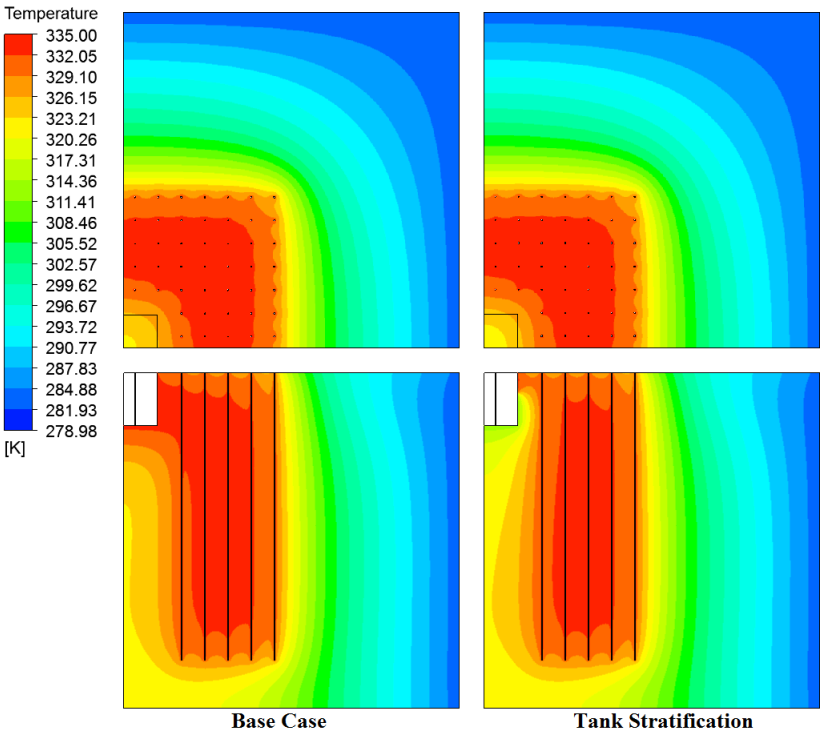

Figure 5.48: Temperature contours for tank stratification at a fully charged state (1590 days) for the side view (plane containing boreholes, z=1.16 m) and top view (borehole half length, y=-15 m)

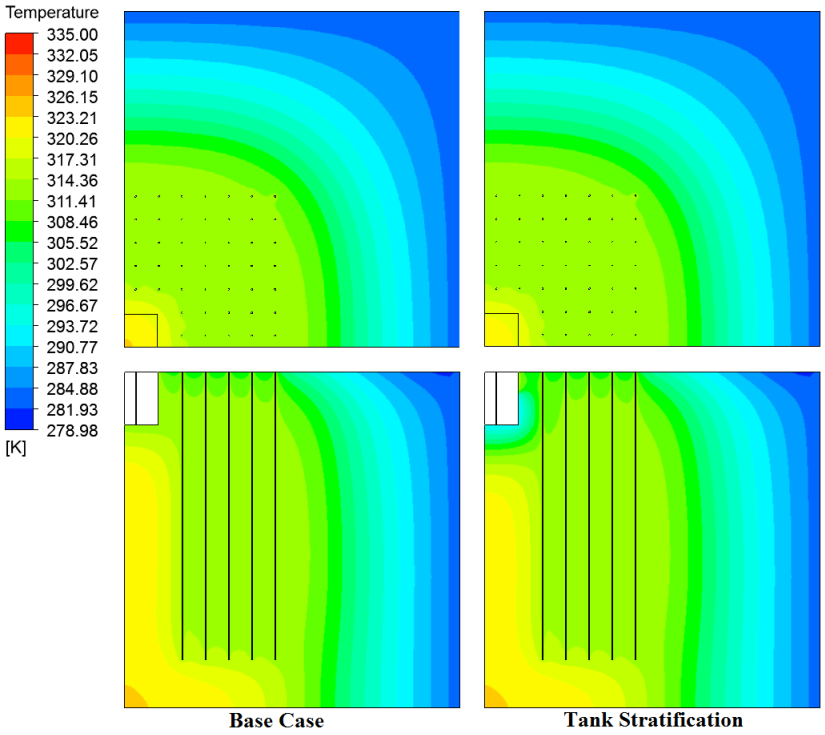

Figure 5.49: Temperature contours for tank stratification at a fully discharged state (1770 days) for the side view (plane containing boreholes, z=1.16 m) and top view (borehole half length, y=-15 m)

The Tank Stratification has an interesting effect on temperature contours, as seen in Figures 5.48 and 5.49, which leads to a pocket of colder soil near the bottom half of the tank, while the rest of the domain is relatively unchanged. Tank stratification also results in lower temperatures between the tank and the first ring of boreholes.

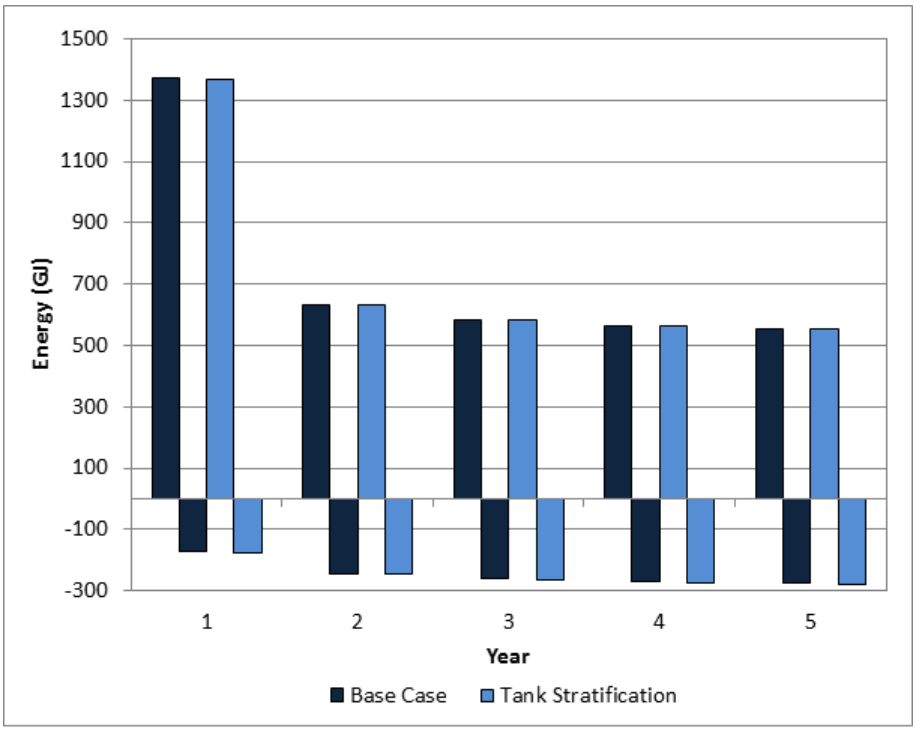

Figure 5.50: Energy injected and extracted for tank stratification over 5 years

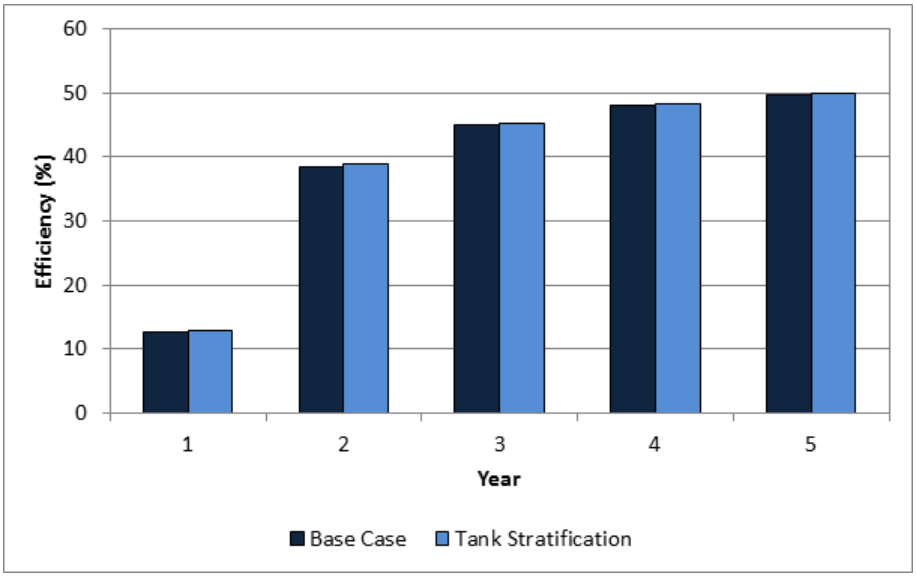

Figure 5.51: Efficiency of tank stratification over 5 years

Case	Energy Injected (GJ)	Energy Extracted (GJ)	Efficiency
Base Case	553.95	-274.89	49.62
Tank Stratification	556.01	-277.50	49.91

Table 5.7: Year 5 data for tank stratification

As seen from Figures 5.50 and 5.51 and Table 5.7, the tank stratification had little effect on both energy and efficiency of the system, similar to the case of insulating the bottom of the tank.

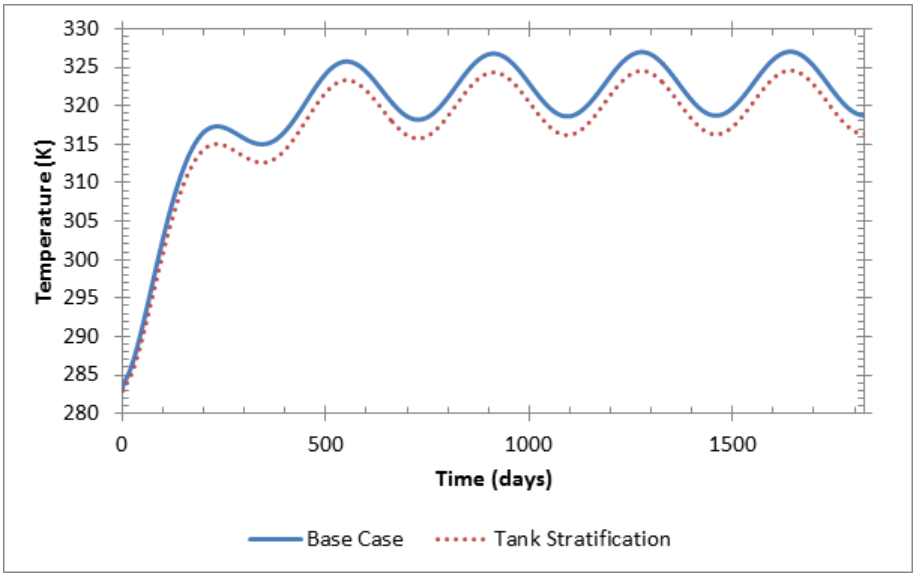

Figure 5.52: Temperature transients of the soil plug of tank stratification over 5 years

From Figure 5.52 it can be observed that there is a greater difference between the two in terms of the soil plug temperature. This is because the soil plug temperature includes the area very close to the tank, where there would be the largest difference between the two simulations. Because efficiency looks at overall system performance,

for which the tank is a small component, there is essentially no overall difference in efficiency.

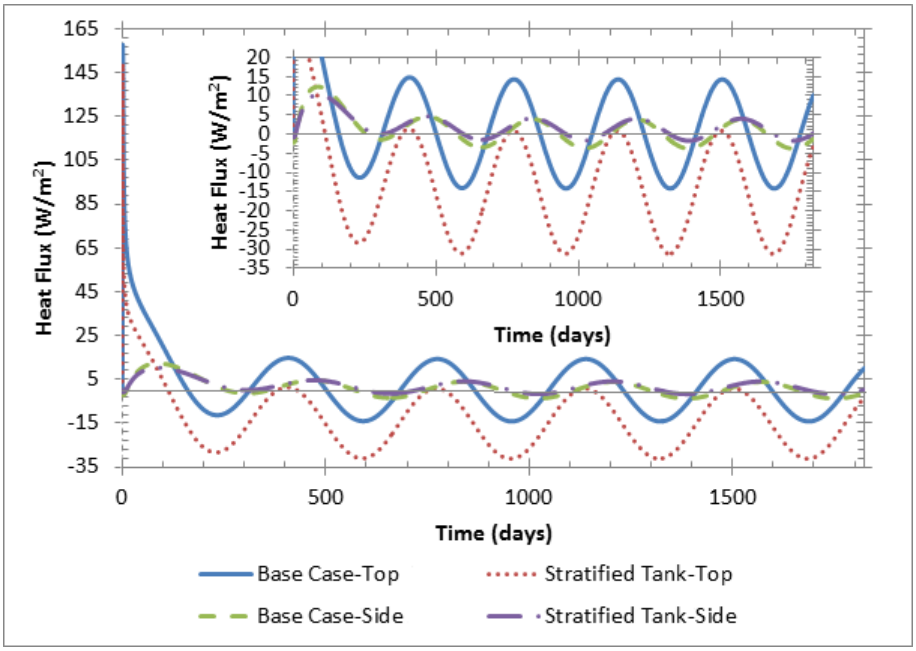

Figure 5.53: Heat fluxes to the soil plug for tank stratification over 5 years

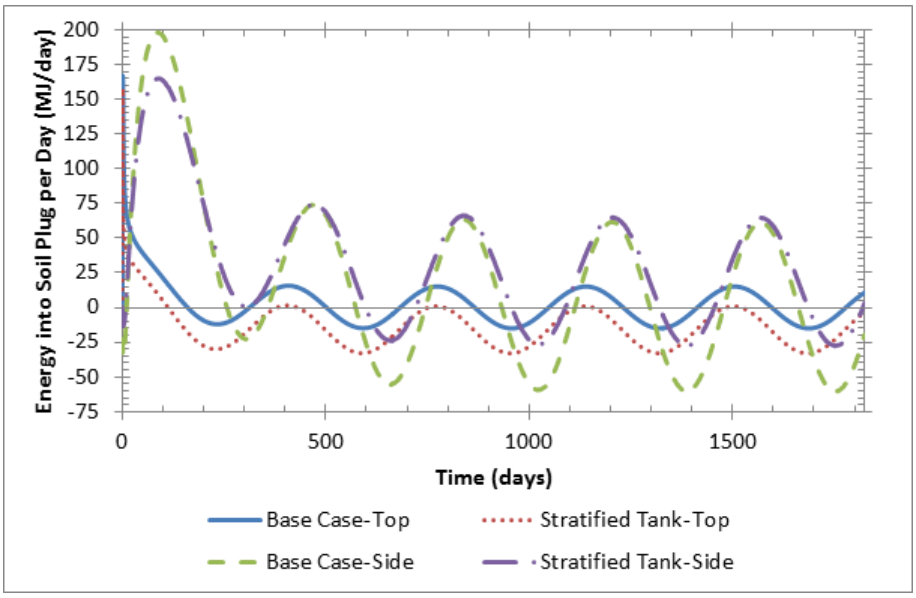

Figure 5.54: Energy injected and extracted from the soil plug for tank stratification over 5 years

Figures 5.53 and 5.54 confirm this fact. The heat flux through the bottom of the tank, and the corresponding energy is lower for the Tank Stratified case compared to the Base Case. There is a larger difference between the heat fluxes, but due to the small area of the bottom of the tank, the overall energy transfer to the borehole field is unaffected the the stratification.

5.8 Impact of Tank Aspect Ratio

The geometry of the tank studied in all the simulations thus far has been the same, a fairly standard tank designed to reduce the amount of heat losses by minimizing the surface area to volume ratio. However, tanks can come in a range of dimensions, so the impact of the aspect ratio must be considered. The two tanks presented here are roughly the limit on what would be implemented in the field [39]. The number of

boreholes has been changed to maintain the spacing as close to that of the Base Case as possible. The tank volume was kept the same as in the Base Case, but the aspect ratio varied. Two additional cases were simulated: a narrow tank and a wide tank. All tanks were modelled as having square cross sections. Details on the geometries are given in Table 5.8.

Case	Width/Width/Depth	Number of Boreholes
Base Case	7 m×7 m×5.5 m	45
Narrow Tank	5.5 m×5.5 m×9 m	40
Wide Tank	11.5 m×11.5 m×2 m	55

Table 5.8: Dimensions of tanks with different aspect ratios

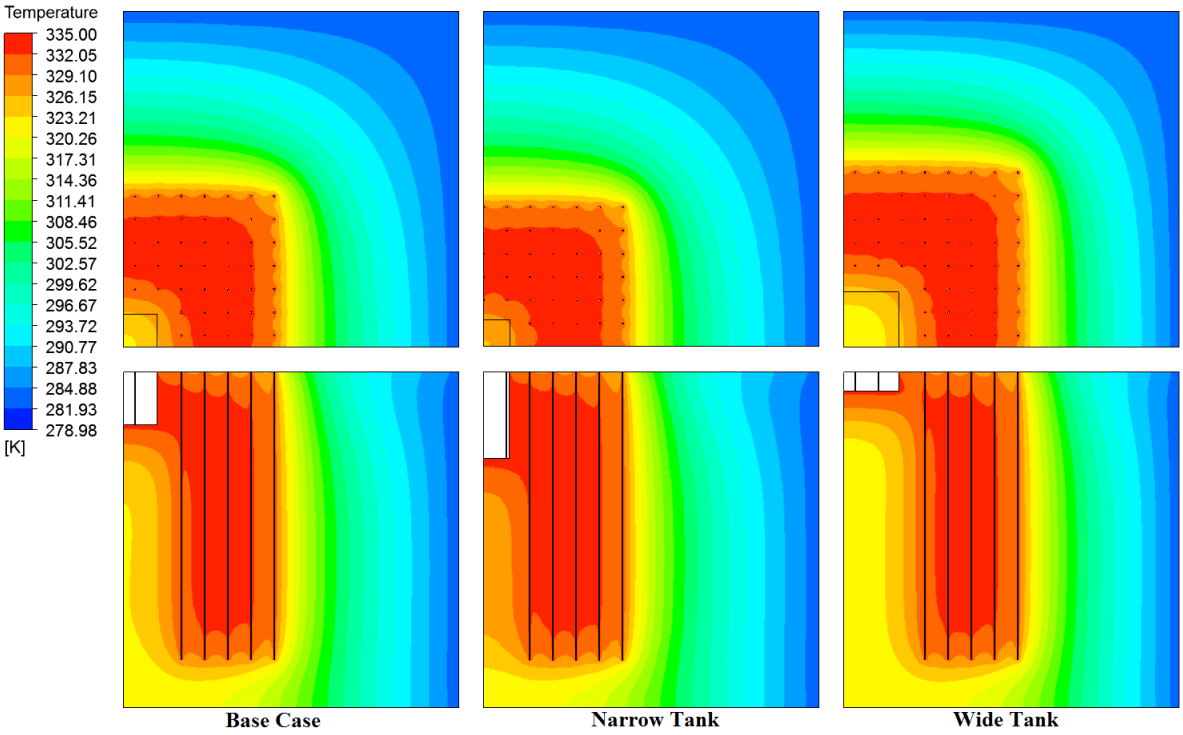

Figure 5.55: Temperature contours for different tank aspect ratios at a fully charged state (1590 days) for the side view (plane containing boreholes, z=1.16 m) and top view (borehole half length, y=-15 m)

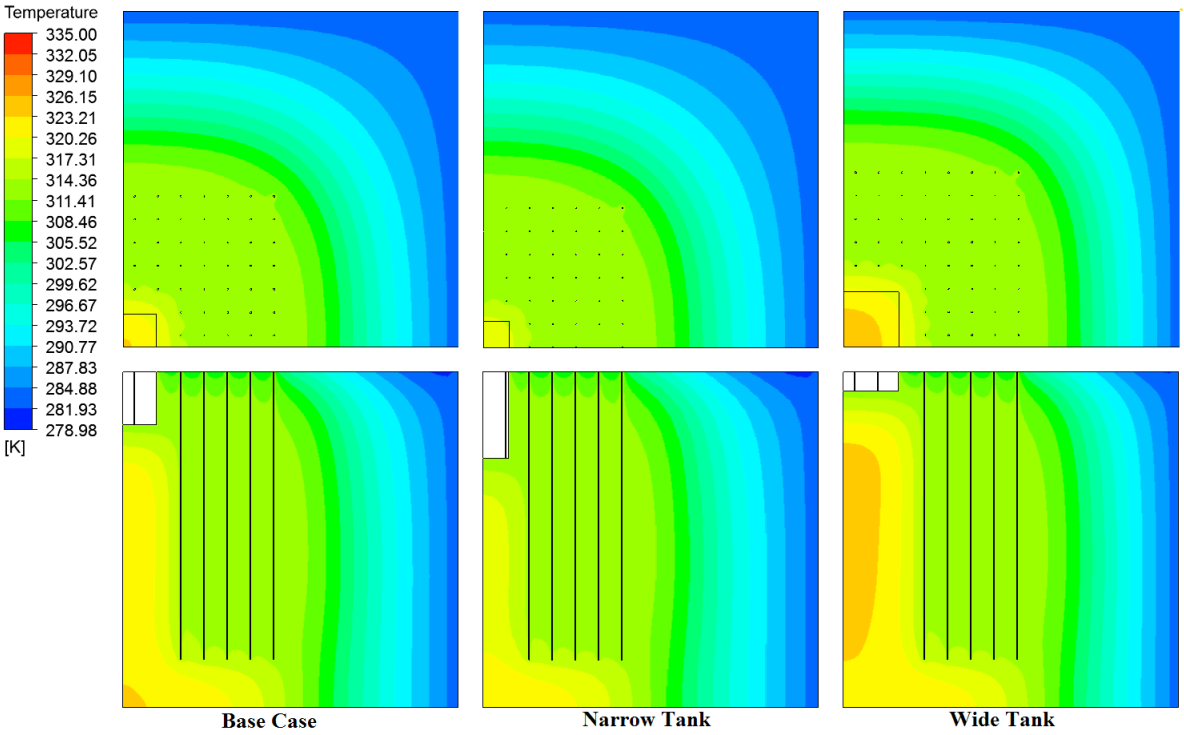

Figure 5.56: Temperature contours for different tank aspect ratios at a fully discharged state (1770 days) for the side view (plane containing boreholes, z=1.16 m) and top view (borehole half length, y=-15 m)

In order to assess the performance of the soil plug, a scaling analysis to estimate a heat transfer time constant was carried out similar to what was presented in section 5.2 for the Base Case. The results are presented in Table 5.9 below.

Case	Half Tank Side Length (m)	Time Constant (days)
Base Case	6	168
Narrow Tank	2.25	69
Wide Tank	5.75	453

Table 5.9: Time constants for tanks with different aspect ratios

Figures 5.55 and 5.56 show that the narrower the tank, the hotter the soil plug, which is consistent with the time constants of each in Table 5.9. The Wide Tank case is also seeing less thermal interaction between the tank and the first ring of boreholes.

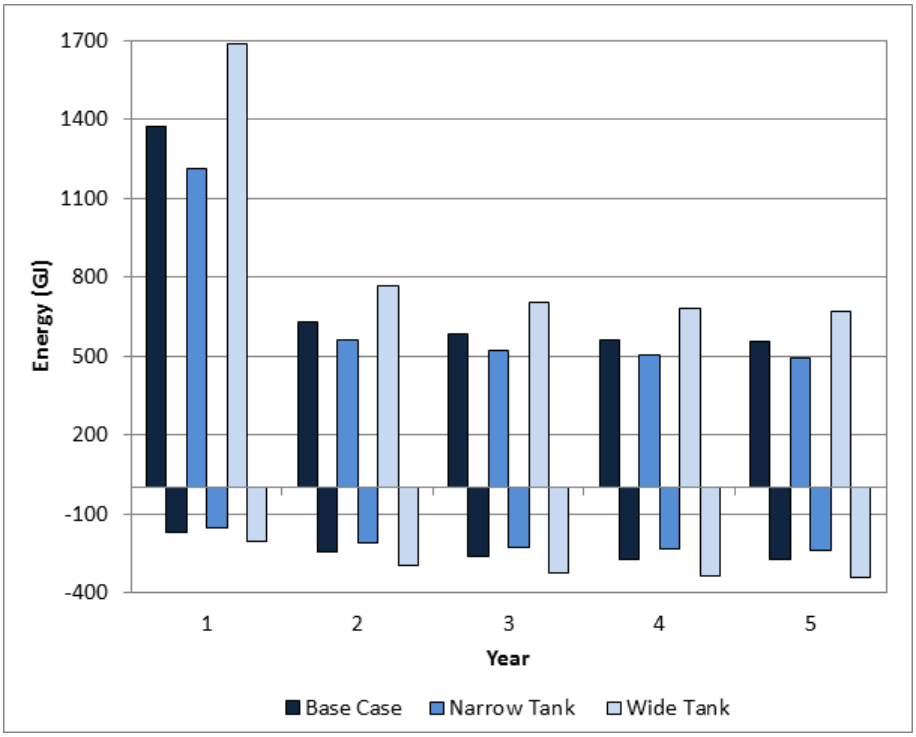

Figure 5.57: Energy injected and extracted for different aspect ratios over 5 years

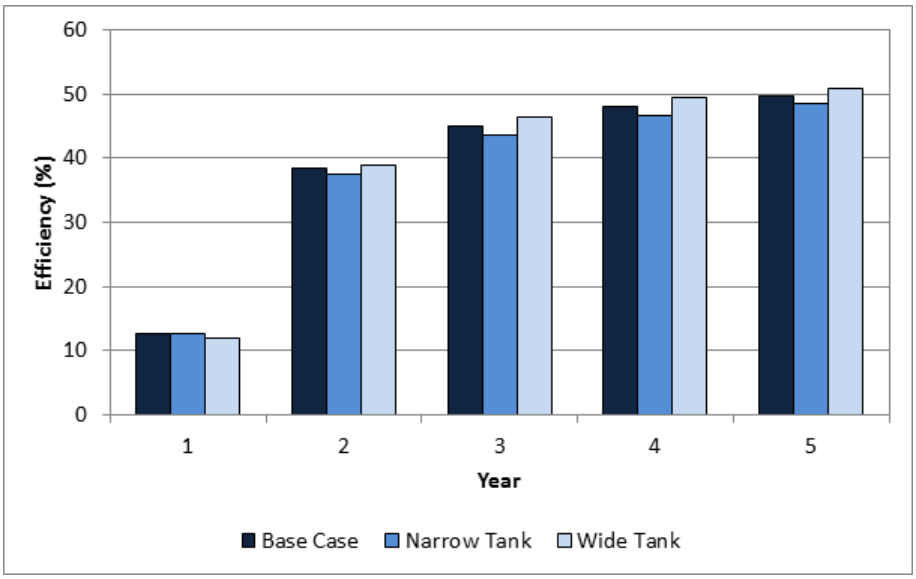

Figure 5.58: Efficiency of different aspect ratios over 5 years

Case	Energy Injected (GJ)	Energy Extracted (GJ)	Efficiency
Base Case	553.95	-274.89	49.62
Narrow Tank	495.49	-239.83	48.40
Wide Tank	671.35	-341.21	50.83

Table 5.10: Year 5 data for tank aspect ratio

Case	Surface Area (m^2)	% Increase in Surface Area	Energy Injected/ Surface Area (GJ/m^2)	Energy Extracted/ Surface Area (GJ/m^2)	Year 5 Efficiency	% Increase in Year 5 Efficiency
Base Case	687.55	N/A	0.8057	-0.3998	49.62	N/A
Narrow Tank	623.10	-9.37	0.7952	-0.3849	48.40	-2.46
Wide Tank	763.61	11.06	0.8046	-0.4089	50.83	2.42

Table 5.11: Comparison of efficiencies based on surface area of tank and boreholes

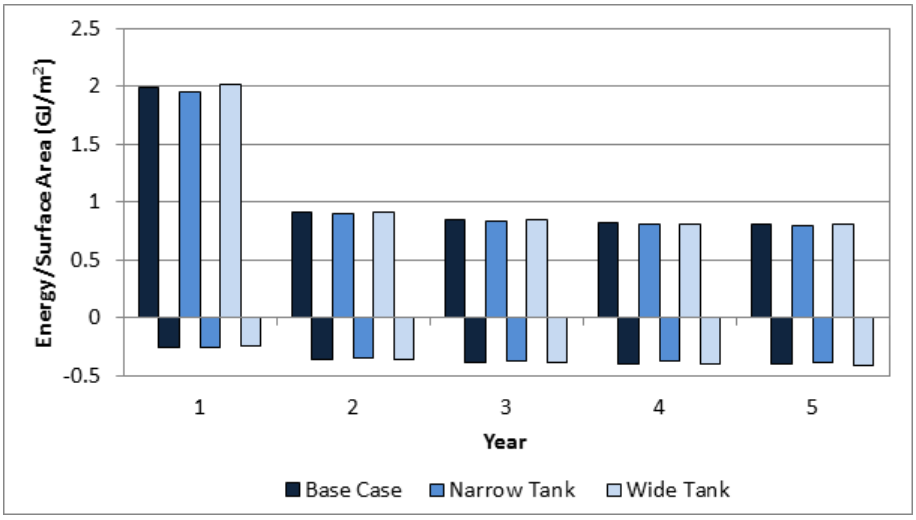

Figure 5.59: Energy injected and extracted per unit surface area for different aspect ratios over 5 years

From Figures 5.57 and 5.58 and Table 5.10, the initially surprising conclusion that the Wide Tank case outperforms the others is noticed. However, looking at this set of simulations in more detail shows that the Narrow Tank case has 40 boreholes, the

Base Case 45 and the Wide Tank 50. If we consider the energy injected and extracted by surface area, as seen in Table 5.11, it is apparent that though there is a significant difference in areas for the three cases, the efficiencies do not scale correspondingly. Figure 5.59 shows the energy injected and extracted per unit of surface area, which clearly shows that there is a limited difference in overall performance of the field due to tank aspect ratio.

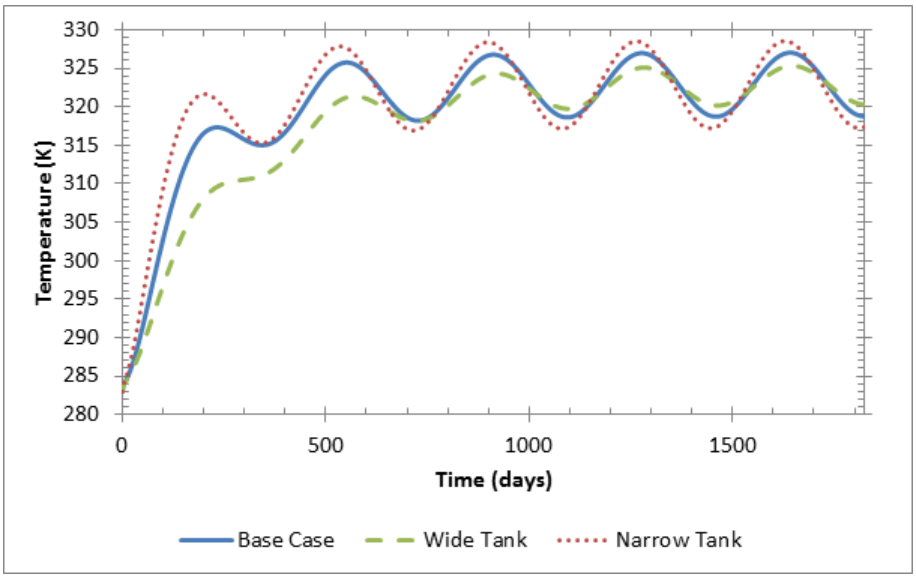

Figure 5.60: Temperature transients of the soil plug of different aspect ratios over 5 years

Figure 5.60 shows the differences in the temperatures of the three cases' soil plugs. Note that the Wide Tank case takes longer to reach a periodic state than the other two. This is because the Wide Tank has a greater distance for the heat to travel radially in order to heat the centre of the soil plug, and thus takes longer to reach a periodic state. This is of course consistent with the larger time constant for the Wide Tank. The graph also shows that the narrower the tank the higher average soil plug temperature, which is also consistent with a reduced time constant for the Narrow

Tank case.

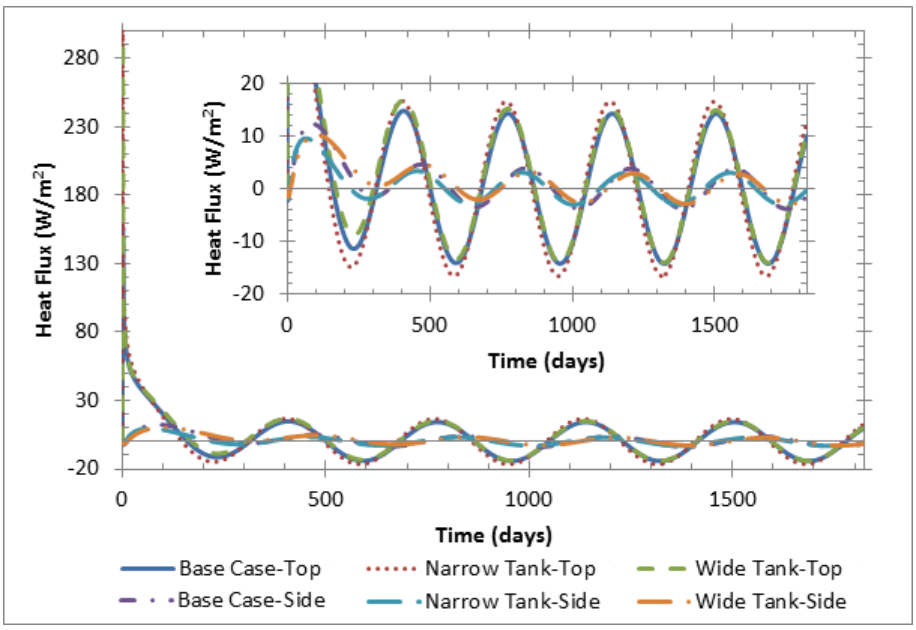

Figure 5.61: Heat fluxes to the soil plug for different aspect ratios over 5 years

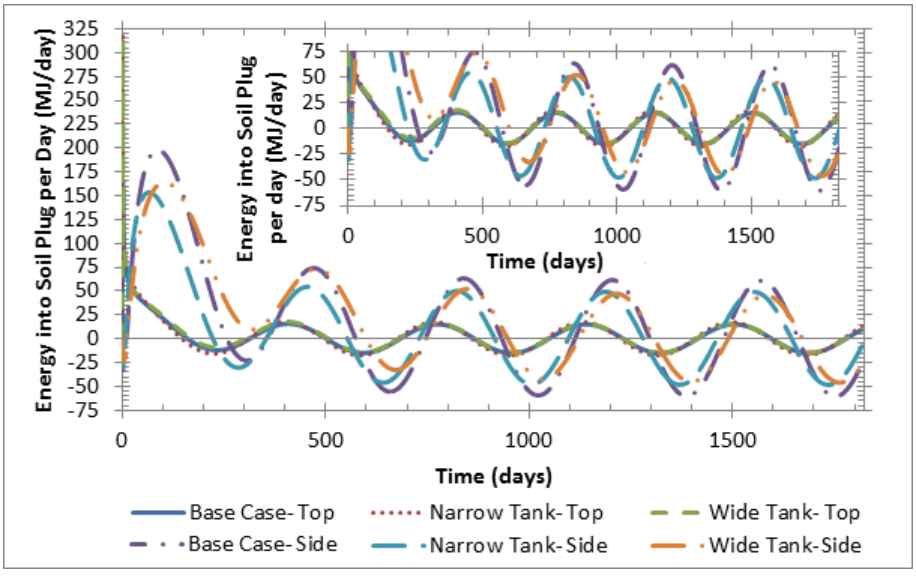

Figure 5.62: Energy injected and extracted from the soil plug for different aspect ratios over 5 years

Despite the differences in heat transfer area and volume of the soil plug, the graphs for heat flux and energy, Figures 5.61 and 5.62, show the same general trends. Both graphs show that there is relatively little difference in the heat flux and energy injected through the top of the soil plug, despite differing areas. The Wide Tank is again lagging behind the other two in terms of energy and takes longer to reach a periodic state.

5.9 Impact of Soil Type

This section describes the impact of different soil types on borehole field performance. The important material properties are thermal conductivity and the product of density and specific heat capacity. All of these simulations were run using the same initial and boundary conditions as the base case; however, the values of the material properties were changed according to Table 5.12 [39].

Soil Type	Conductivity, k (W/m)	Density, ρ (kg/m^3)	Specific Heat Capacity, C_p (kJ/kg·K)	ρC_p (kJ/m^3·K)	Thermal Diffusivity, α (m^2/day)
Base Case	2	1600	1.48	2368	0.07297
Calibrated	1.68	3406	1	3406	0.04262
Heavy Saturated	2.42	3205	0.84	2692	0.07766
Heavy Damp	1.3	2100	0.96	2016	0.05571
Heavy Dry	0.86	2000	0.84	1680	0.04423
Hybrid Base Case/Calibrated	2	3406	1	3406	0.05073
Dense Rock	3.5	3200	0.84	2688	0.1125
Light Dry	0.35	1440	0.84	1210	0.025

Table 5.12: Different soil properties considered in section 5.8

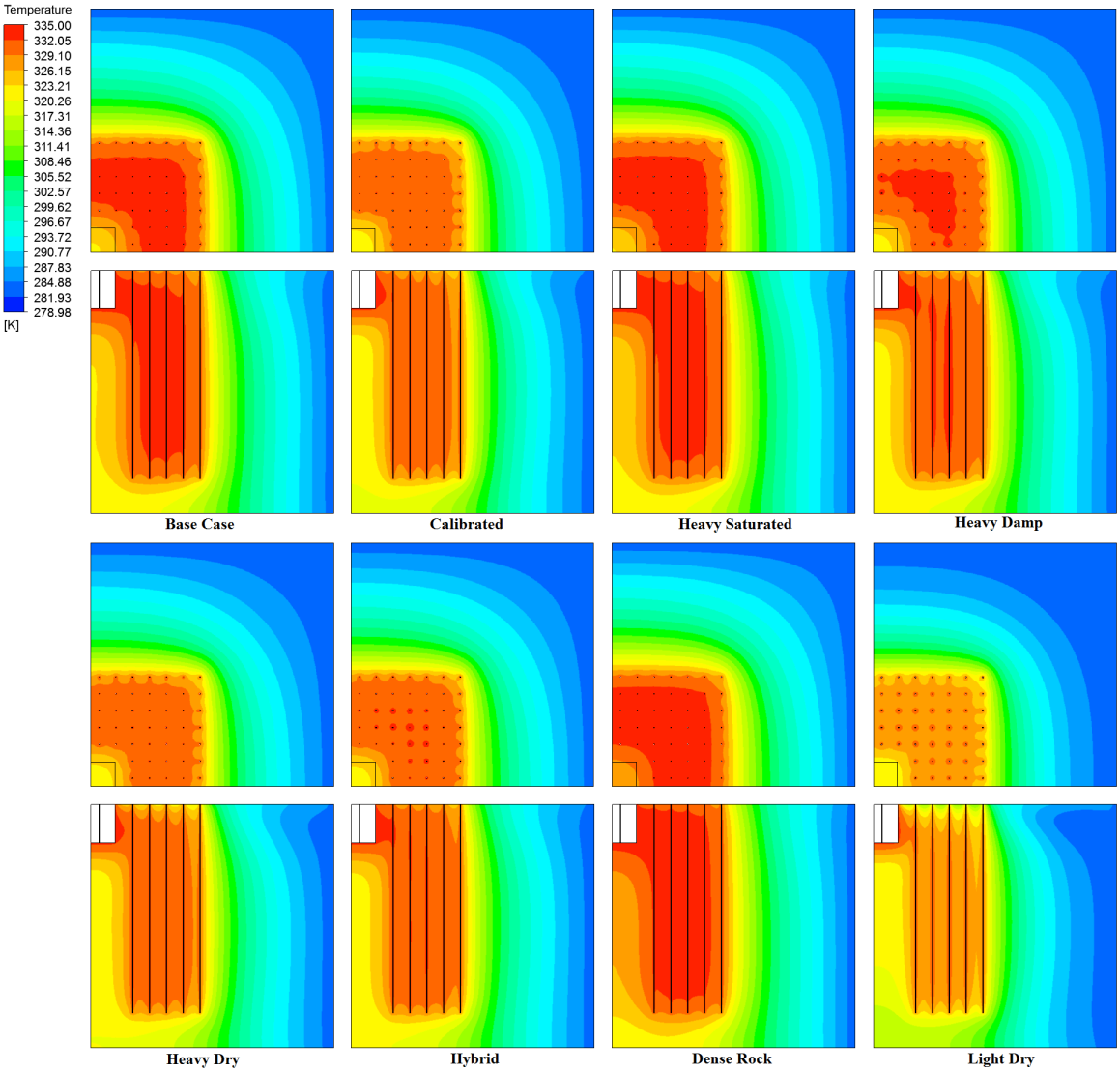

Figure 5.63: Temperature contours for different soil types at a fully charged state (1590 days) for the side view (plane containing boreholes, z=1.16 m) and top view (borehole half length, y=-15 m)

From Figure 5.63, it can be seen that the soils with the higher thermal diffusivity values (Base Case, Heavy Saturated and Dense Rock) all have higher temperatures near the boreholes. Light Dry charged the ground to a comparatively low temperature as compared to the rest.

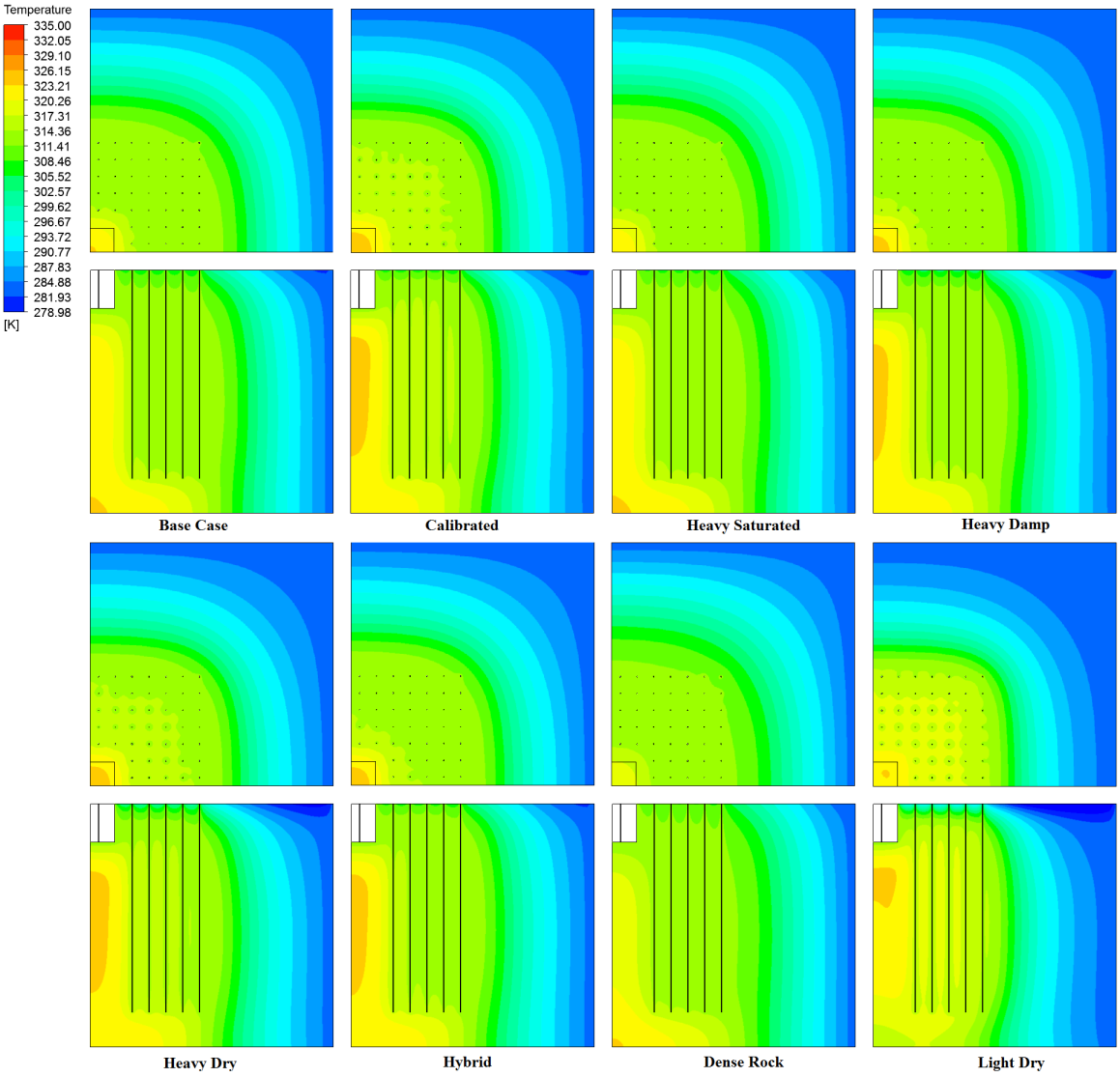

Figure 5.64: Temperature contours for different soil types at a fully discharged state (1770 days) for the side view (plane containing boreholes, z=1.16 m) and top view (borehole half length, y=-15 m)

Figure 5.64 shows that not all the of soils discharge as much heat. Calibrated, Heavy Damp, Heavy Dry, Hybrid and Light Dry all have a pocket of hot soil remaining under the tank. The other three cases have a higher thermal diffusivity, which is probably why they discharged better. It can also be observed that Heavy Dry and

Light Dry have colder regions near the top right corner of the domains, implying that they have higher losses to the air. These two cases have the lowest values of the product of density and specific heat capacity.

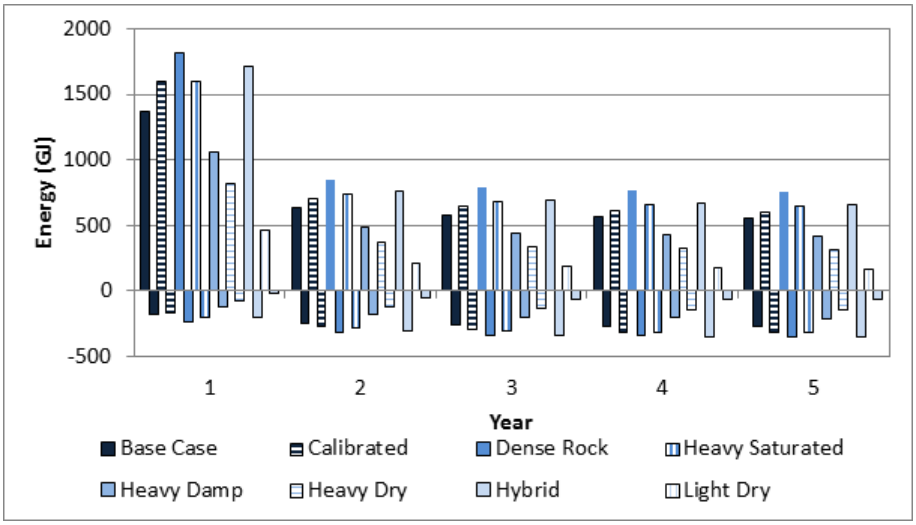

Figure 5.65: Energy injected and extracted for different soil types over 5 years

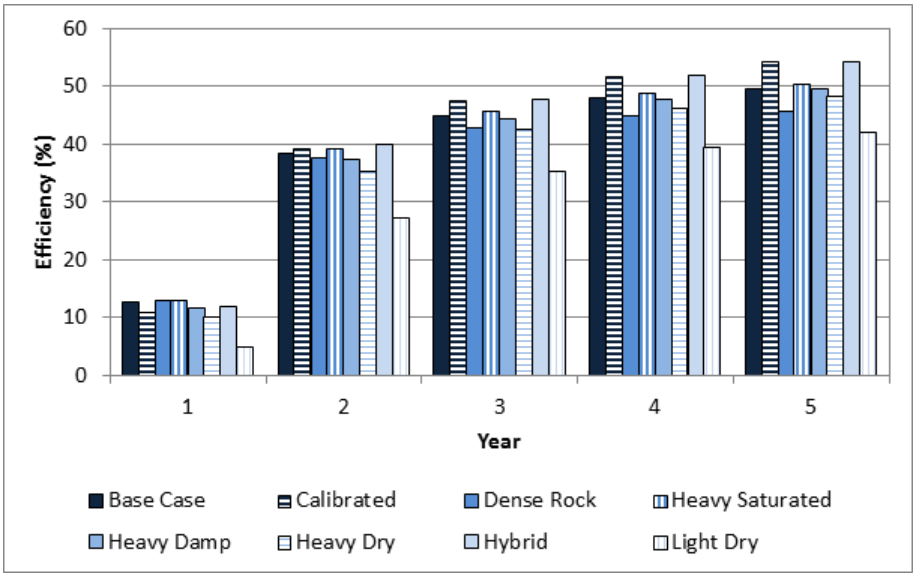

Figure 5.66: Efficiency of different soil types over 5 years

Case	Energy Injected (GJ)	Energy Extracted (GJ)	Efficiency
Base Case	553.95	-274.89	49.62
Calibrated	597.95	-323.86	40.59
Dense Rock	760.40	-347.20	45.66
Heavy Saturated	642.23	-322.10	50.15
Heavy Damp	419.49	-208.27	49.65
Heavy Dry	315.01	-151.59	48.12
Hybrid	654.81	-354.77	41.16
Light Dry	165.66	-69.57	29.70

Table 5.13: Year 5 data for different soil types

Table 5.13 presents the energies and efficiencies for the different cases in year five. From Figures 5.66 and 5.73, it can be observed that while dense rock injects the most amount of heat out of all the soil types, it also has one of the lower efficiencies. Due to the high conductivity of dense rock, a lot of the heat injected into the domain is lost to the surrounding soil. Meanwhile, the calibrated soil does not inject as much heat, but has the highest efficiency.

Note that the ranking of soil types changes slightly if you compare overall efficiency as opposed to the efficiency in year 5. This is because some soil types, such as dense rock, have much higher losses in the first year that skew the average. In general, the performance of all eight cases ranges from 10-13% between the highest (Calibrated) and the lowest (Light Dry).

5.9.1 Effect of Soil Properties on Efficiency

One of the key points to note from this set of simulations is that simply considering the thermal diffusivity is not enough to determine the effect of soil type on the performance of the field.

The performance of the systems depends on two things: the product of ρ and C_p, k. As such, the following graphs present the ranking of each type of soil as a function of each of these properties.

In order to asses the impact of the soil properties on the efficiency of the system, two sets of two cases were compared. The first set has a fixed value of thermal conductivity, and the second set has a fixed value of the product of specific heat and density.

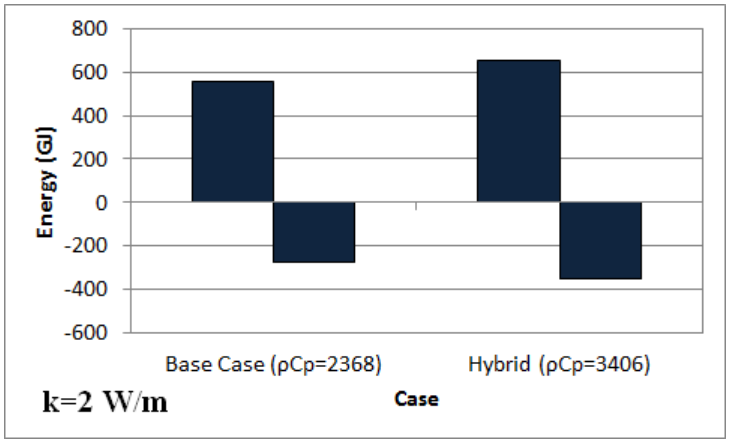

Figure 5.67: Effect of the product of density and specific heat capacity on year 5 energy

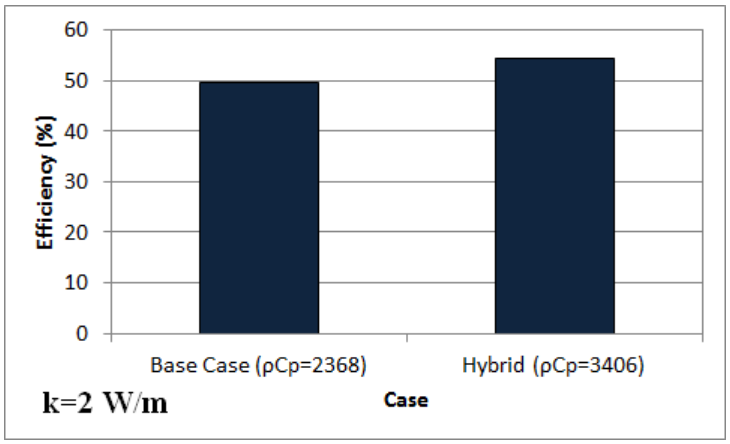

Figure 5.68: Effect of the product of density and specific heat capacity on year 5 efficiency

Figure 5.67 presents the energy injected and extracted for year 5 for two cases that have the same thermal conductivity, and it can be seen that the Hybrid case both injects and extracts more energy than the Base Case. Figure 5.68 presents the corresponding efficiencies. The Hybrid case, with the higher value of the product of density and specific heat capacity, has the higher efficiency, as expected.

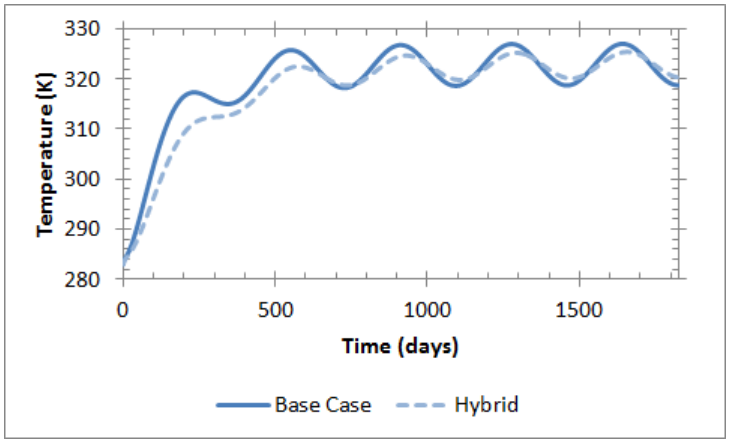

Figure 5.69: Effect of the product of density and specific heat capacity on soil plug temperature

From Figure 5.69, it can be seen that the Hybrid cases takes longer to reach a

periodic state and it has a smaller amplitude than the Base Case.

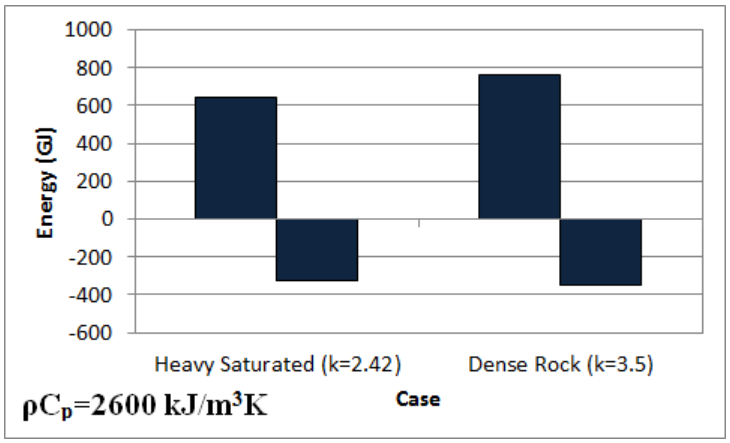

Figure 5.70: Effect of thermal conductivity on year 5 energy

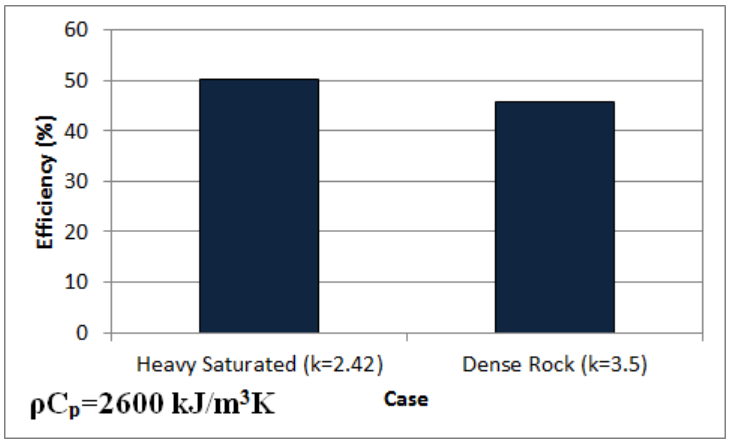

Figure 5.71: Effect of thermal conductivity on year 5 efficiency

Figure 5.70 presents the energy injected and extracted for two cases that have the same product of density and specific heat capacity and Figure 5.71 presents the corresponding efficiencies. The Heavy Saturated case has a lower value of thermal conductivity and higher efficiency, however, the Dense Rock case actually extracts slightly more energy. The higher thermal conductivity for the Dense Rock case results

in a lot of energy being lost out of the sides of the core region, which is why it has the lower efficiency of the two.

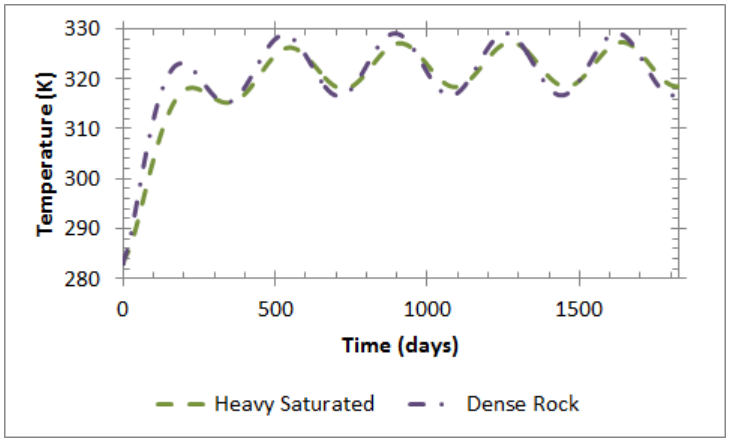

Figure 5.72: Effect of the product of density and specific heat capacity on soil plug temperature

From Figure 5.72, it can be seen that the Heavy Saturated case has a lower maximum temperature in the first charge, but that after the initial charge, the two show little difference.

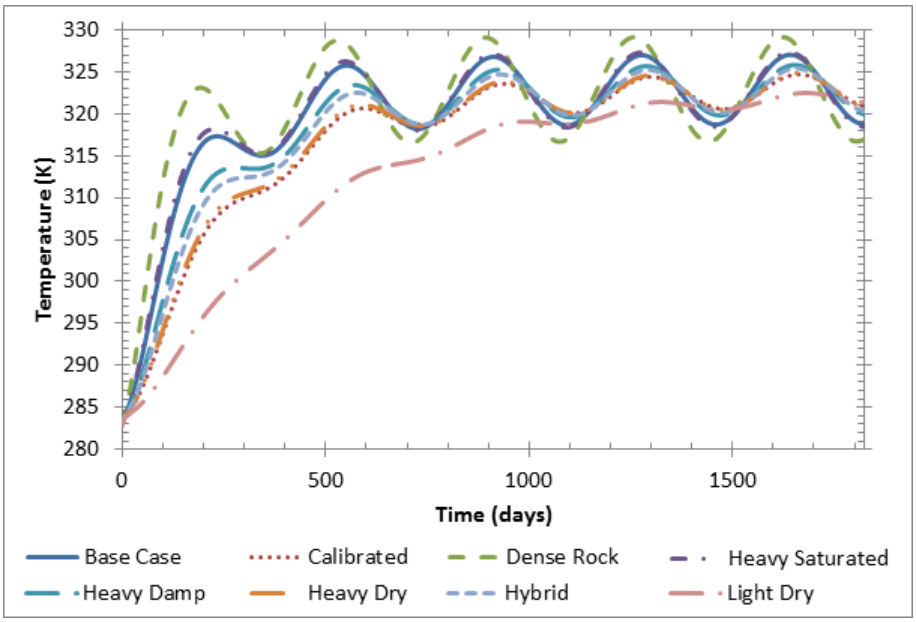

Figure 5.73: Temperature transients of the soil plug for different soil types over 5 years

From Figure 5.73, it can be seen that the highest temperatures correspond to the highest thermal diffusivities, and the lowest temperatures, the lowest thermal diffusivites, with the exception of the Calibrated case. The higher the thermal conductivity, the greater the amplitude of temperature (such as for Dense Rock) and the lowest thermal conductivity (Light Dry) barely sees any fluctuations at all. The Light Dry case also takes the longest to reach steady state.

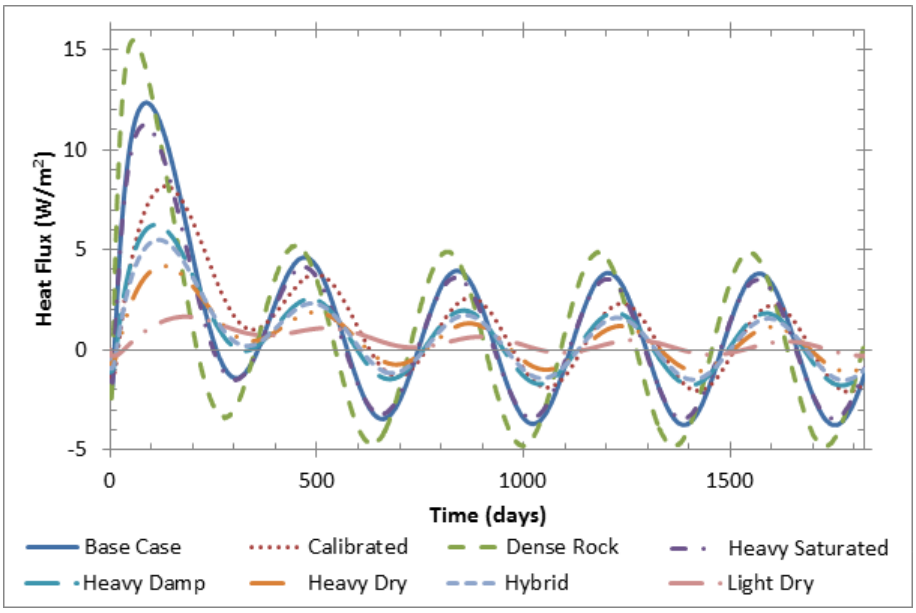

Figure 5.74: Heat fluxes to the side of the soil plug for different soil types over 5 years

From Figure 5.74, it can be seen that heat flux is approximately a function of thermal conductivity. With the exception of the Base Case, the higher the thermal conductivity, the higher the heat flux.

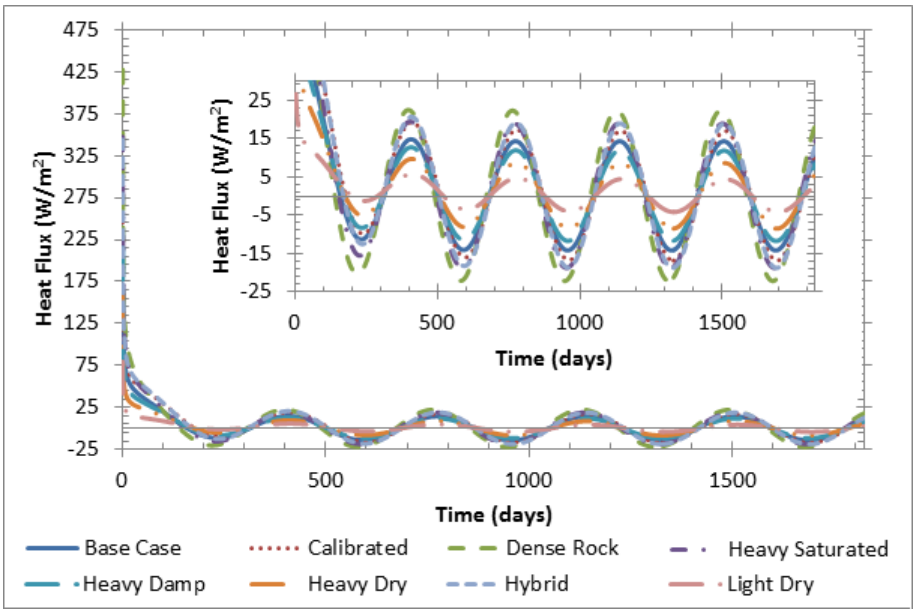

Figure 5.75: Heat fluxes to the top of the soil plug for different soil types over 5 years

The graph presented in Figure 5.75 is also roughly a function of thermal conductivity, with the exception of the Base Case again. The higher the thermal conductivity, the greater the heat flux into and out of the soil plug.

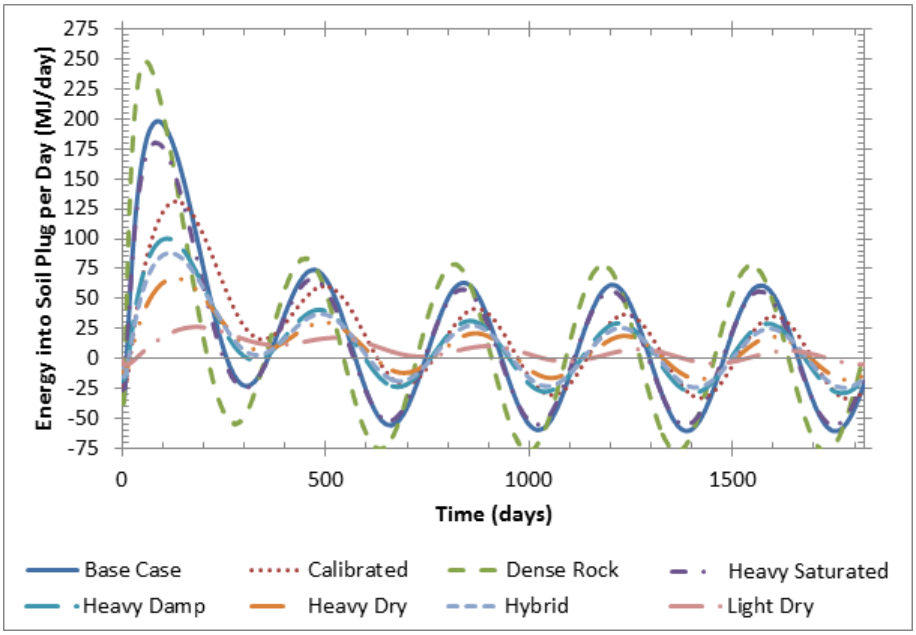

Figure 5.76: Energy injected and extracted from the side of the soil plug for different soil types over 5 years

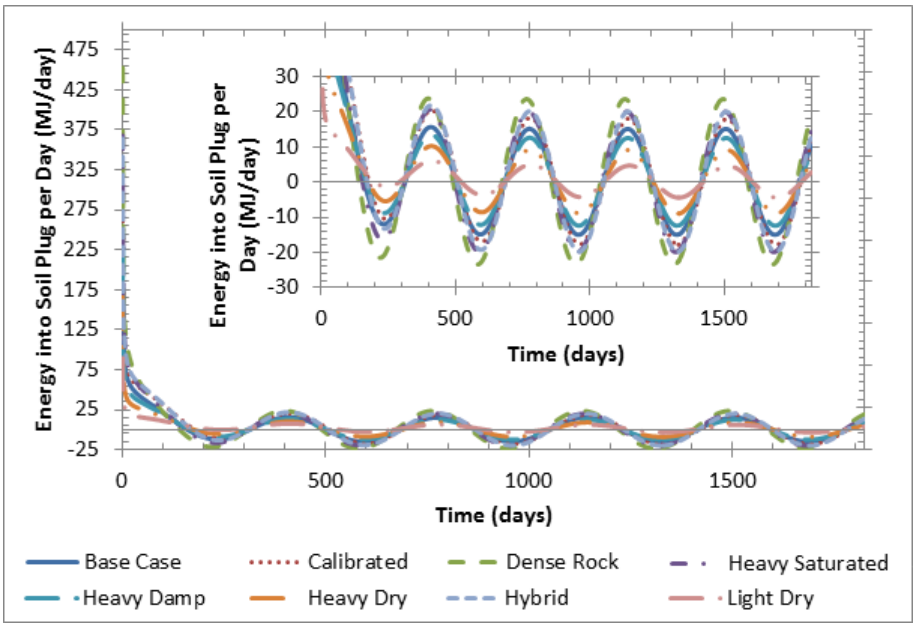

Figure 5.77: Energy injected and extracted from the top of the soil plug for different soil types over 5 years

Similar to the graphs for heat flux, Figures 5.76 and 5.77 follow the same trend.

5.10 Summary of Test Cases

Test cases were performed to assess the effect of different geometries, number of rings, radial and tank stratification, tank bottom insulation, aspect ratio of the tank and soil type. It was determined that some of these had more significant impacts on the solution than others. For example, Tank Stratification and Tank Bottom Insulation had little impact on the simulation as compared to the Base Case. The Alternate Geometries had more difference between the cases, but were still not as large of a difference as might be expected. Increasing the number of rings and adding radial stratification both improve efficiency significantly. Radial stratification showed the second largest difference in efficiencies as compared to the Base Case of around 8%. The Tank Aspect ratio changes saw some difference between cases, but did not gain efficiency proportionally to the heat transfer surface area. And finally, it was concluded that some soils are not suitable for borehole fields, such as Light Dry and Dense Rock. The soils that were not suitable performed up to 15% worse (Light Dry) than the Base Case, and the well suited soils performed around 9% better (Calibrated and Hybrid).

Chapter 6

Conclusions & Recommendations

6.1 Conclusions

A large portion of energy use in Canada goes towards space heating. As such, any measures to reduce the dependence on non-renewable resources has the potential to significantly reduce the carbon footprint. This makes technologies such as solar communities invaluable, and the continued work on improving their efficiency is important. Due to the difference in supply and demand of solar energy for heating purposes, seasonal storage must be employed. A survey of the literature covered typical performance by borehole fields and large tanks. Verification was performed on two dimensional simulations and verified using either an analytical solutions or existing solutions from the literature. This thesis has presented a three dimensional CFD study on the impact of burying a large tank within a borehole field. The goal was to assess the interactions between the buried tank and borehole field.

6.2 Impact of Changing Parameters for a Large Buried Tank within a Borehole Field

A series of simulations was performed to explore the performance of the borehole field for varying conditions. Firstly, a Base Case was established as a tank with five rings of boreholes surrounding it, and run using average soil properties. The second set of simulations compared the Base Case against a Typical BTES and the Base Case without the tank, and it was shown that inserting a tank within a borehole field did not significantly reduce the efficiency (decrease in efficiency of about 1.5%), which demonstrates the feasibility of this design. Radial stratification was then modelled, using both DLSC data and a weighted average profile that was the same as the Base Case. Radial stratification of the boreholes helps reduce losses across the domain which aids in increasing the thermal efficiency of the field by about 4%.

Insulating the bottom of the tank and stratifying the tank, however, do not significantly impact the performance of the field. However, insulation may be important from the tank's point of view, so further research may be required. The aspect ratio of the tank mainly impacts the "soil plug," defined as the column of soil below the tank; the narrower the tank, the quicker it heats up and reaches a periodic state. Investigating the impact of soil type demonstrated that certain types of soil (light dry, dense rock, etc) are not suitable for borehole fields. It also demonstrated that a lower thermal conductivity and high value of density and specific heat capacity yield a more efficient field. Higher thermal conductivities lead to better heat transfer from the boreholes to the ground, but it also causes higher losses from the field.

From these simulations, it can be concluded that radial stratification and soil

properties should be selected carefully to ensure optimal efficiency. Factors that primarily affect the tank, such as tank stratification and insulation do not need to be modelled, unless detailed work is needed to analyze the performance of the tank itself.

6.3 Recommendations for Future Work

Current work was simplified by assuming the temperature of the fluid within the boreholes was the same as the borehole wall temperature. The fluid behaviour within the boreholes was not considered, which resulted in the effect of the grout and the tube type not being considered. Future work should look at different types of boreholes (coaxial, U-tube, double U-tube, etc.) and the corresponding grout/thermal resistance associated with each.

System modelling would also be highly beneficial to see how burying the tank would impact overall system performance.

As mentioned in the previous section, further study on the tank will be necessary to fully understand the system. The current work has examined the impact of a tank on a borehole field, and now the impact of the boreholes on the tank must be considered. It has yet to be seen how insulation on the tank, tank geometry, tank wall conduction due to different tank materials amongst others will impact the tank. Factors such as the effect of heat exchange between tank and boreholes' impact on tank stratification, temperature will need to be investigated. Tank stratification is very important for the efficiency of the system. It is thus important to ensure that the heat from the borehole field will not mix the tank excessively.

The geometry of the borehole field should be investigated further. In particular,

the effect of soil type on borehole spacing and borehole depth compared to field size should be considered.

Lastly, the CFD simulations with and without tanks provide significant detail on the long term performance of borehole fields. Future work may include a comparison of these results to those from coarser models, such as that in TRNSYS to determine the capability of those models at predicting long term performance.

Bibliography

[1] Natural Resources Canada. Energy efficiency trends in Canada, 1990 to 2009, 2012. URL http://oee.rncan.gc.ca/publications/statistics/trends11/chapter3.cfm?attr=0.

[2] University of Oregon. Basics of solar energy, 2014. URL http://zebu.uoregon.edu/disted/ph162/l4.html.

[3] F.G.H. Koene. The e-hub challenge, June 2014. URL http://www.e-hub.org/the-challenge.html.

[4] A. Ucar and M. Inalli. A thermo-economical optimization of a domestic solar heating plant with seasonal storage. *Applied thermal engineering*, 27(2):450–456, 2007.

[5] Natural Resources Canada. Drake Landing Solar Community, 2012. URL http://www.dlsc.ca/index.htm.

[6] W.P. Wong, J.L. McClung, J.P. Kokko, O. Kitchener, and A.L. Snijders. First large-scale solar seasonal borehole thermal energy storage in Canada. In *Proceedings of Ecostock Conference, Stockton*, 2006.

[7] I. Dincer. The role of thermal energy storage systems in sustainable development. In *Proceedings of Ecostock Conference, Galloway, NJ, USA*, 2006.

[8] T. Schmidt, D. Mangold, and H. Müller-Steinhagen. Central solar heating plants with seasonal storage in Germany. *Solar energy*, 76(1):165–174, 2004.

[9] F. Ochs, W. Heidemann, and H. Müller-Steinhagen. Effective thermal conductivity of moistened insulation materials as a function of temperature. *International Journal of Heat and Mass Transfer*, 51(3):539–552, 2008.

[10] V. Liebel, M. Reuss, and Z.A.E. Bayern. PE-X borehole heat exchangers for high temperature UTES applications. In *Proceedings of Tenth International Conference on Thermal Energy Storage, Ecostock*, 2006.

[11] J.R. Philip and D.A. De Vries. Moisture movement in porous materials under temperature gradients. *Transactions, American Geophysical Union*, 38:222–232, 1957.

[12] M.F. Lightstone. A numerical study of thermal stratirfication in solar energy storage tanks. Master's thesis, University of Waterloo, 1987.

[13] B. Rezaie, B. Reddy, and M.A. Rosen. Seasonal stratified thermal energy storage exergy analysis. In *ESim 2012: Building Simulation Conference, May 1–4, 2012, Halifax, NS, Canada*, pages 352–365, 2012.

[14] T. Schmidt and D. Mangold. Conversion of Germany's first seasonal solar thermal energy storage into an innovative multifunctional storage. In *Eurosun 2010: International Conference on Solar Heating, Cooling and Buildings, September 28-October 1, 2010, Graz, Austria*, 2010.

[15] J. Steinweg, M. Stegmann, G. Rockendorf, I. Bellin, L. Schäfer, M. Lienhard, and E. Schomburg. Development of a cost-efficient buried hot water storage–concept and first results.

[16] G. Bandyopadhyay, W.D. Gosnold, and M. Mann. Thermal study of a large ground heat exchanger in clay soil in the cold weather environment of nothern USA: Some initial findings. In *Proceedings of Ecostock, Galloway, NJ, USA*, 2006.

[17] H. Schnürer, C. Sasse, and M.N. Fisch. Thermal energy storage in office buildings foundations. *Braunschweig: Institute for Building Services and Energy Design*, 2005.

[18] J. Desmedt, H. Hoes, and J. Van Bael. Status of underground thermal energy storage in Belgium. In *10th International Conference on Thermal Energy Storage, New Jersey, USA*, 2006.

[19] T. Kurevija, D. Vulin, and V. Krapec. Effect of borehole array geometry and thermal interferences on geothermal heat pump system. *Energy conversion and management*, 60:134–142, 2012.

[20] G. Florides and S. Kalogirou. Ground heat exchangersa review of systems, models and applications. *Renewable Energy*, 32(15):2461–2478, 2007.

[21] P. Platell. Developing work on ground heat exchangers. In *ECOSTOCK 2006 Conference Proceedings. New Jersey: ECOSTOCK*, 2006.

[22] S. Koohi-Fayegh and M.A. Rosen. Thermally interacting multiple boreholes

with variable heating strength. In *Proceedings of eSim Conference, Halifax, NS, Canada*, pages 2–3, 2012.

[23] F.B. Cruickshanks, O. Anderson, and J. Bardsley. Borehole sealing in a coaxial heat exchanger by bentonite treatment. *Report Prepared for Environment Canada, Climate Change Division (Atlantic Region), Halifax*, 2007.

[24] K. Sekine, S. Hwang, Y. Nam, and Y. Shiba. Development of a ground-source heat pump system with ground heat exchanger utilizing the cast-in-place concrete pile foundations of buildings. In *ECOSTOCK 2006 Conference Proceedings. New Jersey: ECOSTOCK*, 2006.

[25] D. Pahud, M. Belliardi, and P. Caputo. Geocooling potential of borehole heat exchangers' systems applied to low energy office buildings. *Renewable Energy*, 45:197–204, 2012.

[26] F. Ochs, W. Heidemann, and H. Müller-Steinhagen. Modelling buried hot water thermal energy stores. In *Eurosun 2010: International Conference on Solar Heating, Cooling and Buildings, September 28-October 1, 2010, Graz, Austria*, 2010.

[27] M. Bernier. Geothermal boreholes 101: Basic calculation methods. SNEBERN AGM 2013 Workshop, 2013.

[28] T.V. Bandos, Á. Montero, E. Fernández, J.L.G. Santander, J.M. Isidro, J. Pérez, P.J. Córdoba, and J.F. Urchueguía. Finite line-source model for borehole heat exchangers: effect of vertical temperature variations. *Geothermics*, 38(2):263–270, 2009.

[29] S. Koohi-Fayegh and M.A. Rosen. A review of the modelling of thermally interacting multiple boreholes. *Sustainability*, 5(6):2519–2536, 2013.

[30] P. Eskilson. *Thermal analysis of heat extraction boreholes*. Lund University, 1987.

[31] L. Lamarche. Analytical g-function for inclined boreholes in ground-source heat pump systems. *Geothermics*, 40:241–249, 2011.

[32] M. Cimmino, M. Bernier, and F. Adams. A contribution towards the determination of g-functions using the finite line source. *Applied Thermal Engineering*, 51(1):401–412, 2013.

[33] B. Bouhacina, R. Saim, H. Benzenine, and H.F. Oztop. Analysis of thermal and dynamic comportment of a geothermal vertical U-tube heat exchanger. *Energy and Buildings*, 58:37–43, 2013.

[34] R.A. Beier, M.D. Smith, and J.D. Spitler. Reference data sets for vertical borehole ground heat exchanger models and thermal response test analysis. *Geothermics*, 40(1):79–85, 2011.

[35] M. Philippe, M. Bernier, and D. Marchio. Validity ranges of three analytical solutions to heat transfer in the vicinity of single boreholes. *Geothermics*, 38(4): 407–413, 2009.

[36] Y.A Çengel and A.J. Ghajar. *Heat and mass transfer: fundamentals & applications*. McGraw-Hill, 2011.

[37] L. Appleby. Okotoks, Alberta, Canada, March 2014. URL `http://lanceappleby.com/OkotoksWeather/GraphsFolder/Graph2012_temp.gif`.

[38] H.N. Pollack, S.J. Hurter, and J.R. Johnson. Heat flow from the earth's interior: analysis of the global data set. *Reviews of Geophysics*, 31(3):267–280, 1993.

[39] B. Sibbitt. Personal communication, 2013.

[40] P. Pinel, C.A. Cruickshank, I. Beausoleil-Morrison, and A. Wills. A review of available methods for seasonal storage of solar thermal energy in residential applications. *Renewable and Sustainable Energy Reviews*, 15(7):3341–3359, 2011.

[41] M. Inalli, M. Ünsal, and V. Tanyildizi. A computational model of a domestic solar heating system with underground spherical thermal storage. *Energy*, 22 (12):1163–1172, 1997.

[42] M. Inalli. Design parameters for a solar heating system with an underground cylindrical tank. *Energy*, 23(12):1015–1027, 1998.

[43] B. Karacavus and A. Can. Thermal and economical analysis of an underground seasonal storage heating system in Thrace. *Energy and Buildings*, 41(1):1–10, 2009.

[44] M. Chung, J.-U. Park, and H.-K. Yoon. Simulation of a central solar heating system with seasonal storage in Korea. *Solar Energy*, 64(4):163–178, 1998.

[45] M. Meliß and F. Späte. The solar heating system with seasonal storage at the solar-campus Jülich. *Solar Energy*, 69(6):525–533, 2000.

[46] A. Heller. 15 years of R&D in central solar heating in Denmark. *Solar Energy*, 69(6):437–447, 2000.

[47] P.D. Lund and M.T. Kangas. Net energy analysis of district solar heating with seasonal heat storage. *Energy*, 8(10):813–819, 1983.

[48] A. Ucar and M. Inalli. Thermal and economic comparisons of solar heating systems with seasonal storage used in building heating. *Renewable Energy*, 33 (12):2532–2539, 2008.

[49] W.B. Yang, M.H. Shi, and H. Dong. Numerical simulation of the performance of a solar-earth source heat pump system. *Applied Thermal Engineering*, 26(17): 2367–2376, 2006.

[50] T.P. Bokhoven, J. Van Dam, and P. Kratz. Recent experience with large solar thermal systems in the Netherlands. *Solar energy*, 71(5):347–352, 2001.

[51] Envrionment Canada. Calgary historical wind speed, February 2014. URL `http://calgary.weatherstats.ca/metrics/wind_speed.html`.

[52] Engineering Toolbox. Thermal conductivity of some common materials and gases, February 2014. URL `http://www.engineeringtoolbox.com/thermal-conductivity-d_429.html`.

Appendix A

Tank Table

Appendix A presents the tank table compiled from the literature review. SST stands for seasonal storage tank.

The table presents facts about tank geometry and material, loads, and solar fractions. It can be observed that the size of tanks varies significantly, depending if the application is for a single family or a solar community. From this table, it can be seen that the tanks can be as large as 12000 m^3, with an average value of around 5200 m^3. Most of the tanks are cylindrical, vertical tanks and are often made of concrete, sometimes with liners and insulation to prevent heat and moisture transfer. The solar fraction ranges from 39% to 96%. These values provide some general guidelines for the simulations.

Purpose	Volume (m^3)	Tank Details	Location	Load	Collector Area (m^2)	Solar fraction	Years of Operation	Ref
SST (Single family home)	1 tank, V=68		Massachusetts (MIT), USA		34		1939	[40]
SST (Single family home)	1 tank, V=277		Toronto, Canada			60%	1976	[40]
Duplex	1 tank, V=17		Edmonton, Canada			64% heat, 93% hot water	1970's	[40]
Energy & Hot Water (550 Houses)	1 tank, V=10^5	Rock cavern	Lyckebo, Sweden		4320		1983-2001	[41]
SST (Heating) (50 Houses)	1 tank, V=5000	Cylindrical tank	Tashkent, Uzbekistan	1000 MWh /year	1150	50%		[41]
Heating & SST (25 or 100 houses)	1 tank, V=785	Cylindrical tank	Istanbul, Turkey (Simulation)	10 kW /house	30 m^2 /house	up to 96%		[42]
SST (conversion) (124 row houses)	1 tank, V=4500	Concrete tank	Germany		2920		1996	[14]

Purpose	Volume (m^3)	Tank Details	Location	Load	Collector Area (m^2)	Solar fraction	Years of Operation	Ref
Heat storage (domestic, experiment)	1 tank, V=0.23	H=0.7 m, d=0.65 m, Double shell steel with 50 mm thick, k=0.038 W/m·K insulation	Edirne, Turkey		4	69% of heat requirement		[43]
Heat storage	1 tank, V=600	Simulation	Korea	884965 MJ/year	184			[43]
SST (office building & greenhouse)	1 tank, V=600	H=13 m, d=4.5 m, 5 mm, Stainless steel with glass wool, 0.5 m, k=0.026 W/m·K and/or urethane foam insulation						[44]
SST (23 university housing buildings)	1 tank, V=2500	Stainless steel + polypropylene liners (pit)	SDHPSS Solar-Campus Jülich, Germany	2124 GJ /year total energy	1200	50-60% of heat demand (planned)		[45]
SST	1 tank, V=500	Prefab concrete with bentonite for sealing	Hoerby, Sweden				1990	[46]
SST	1 tank, V=3000	Concrete sheet pile	Herlev I, Denmark		1025		1991	[46]

Purpose	Volume (m^3)	Tank Details	Location	Load	Collector Area (m^2)	Solar fraction	Years of Operation	Ref
SST	1 tank, V=1500		Ottrupgaard, Denmark		560		1995	[46]
3 days' heat demand (summer)	1 tank, V=2100	H=16 m, with 300 mm mineral wool insulation	Marstal I, Denmark		8064		1996	[46]
SST (40-50 houses)	3 tanks, V=500, 1500, and 3000	Buried, with 22 m deep, d=10 cm boreholes, excavated into rock	Finland					[47]
SST	2100 m^3 water tank + 4000 m^3 sand-water store + 10,000 water pit		Marstal, Denmark	28 GW /year	18300		1996	[8]
SST	1 tank, V=1000		Kungälv, Sweden	90 GW/year	10000		2000	[8]
SST	1 tank, V=1500		Nykvarn, Sweden	30 GW/year	7500		1985	[8]
SST	1 tank, V=1100		Falkenberg, Sweden	30 GW/year	5500		1989	[8]
SST	1 tank, V=1200		Aerøskøping, Denmark	13 GW/year	4900		1998	[8]

Purpose	Volume (m^3)	Tank Details	Location	Load	Collector Area (m^2)	Solar fraction	Years of Operation	Ref
SST	1 tank, V=4000		Rise, Denmark	3.7 GW /year	3575		2001	[8]
SST (planned) (8 multi-family houses with 570 apartments)	1 tank, V= 12000	Concrete tank	Friedrichshafen, Germany	2.4 GW /year	3500 (original), 5600 (planned expansion)	47%	1996	[8]
SST (124 houses)	1 tank, V=4500	Concrete tank	Hamburg, Germany	1.6 GW /year	3000	49%	1996	[8]
SST (106 houses)	1 tank, V=2750		Hannover, Germany	694 MW /year	1350	39%		[8]
SST (30 apartments in single family houses)	1 tank, V=500 + duct		Attenkirchen, Germany	487 MW /year	800	55%		[8]
Heat storage (domestic)	1 tank, V=80 m^3/house	Cylindrical tank, simulation	Elâzğ, Turkey	10 kW /house	22 m^2/house			[48]

Purpose	Volume (m^3)	Tank Details	Location	Load	Collector Area (m^2)	Solar fraction	Years of Operation	Ref
20 day heating season sim	1 tank, V=0.5	Simulation, borehole: H=55 m, d=110 mm	Qingdao, China		6			[49]
SST	1 tank, V=1000	Rect. prism (20×20×3.5 m), concrete+steel with HDPE film+open cell polystyrene (original), glass foam+rubber sealent (mod)	Lisse		1200		1995/1996	[50]
SST	1 tank, V=95	Concrete tank +steel liner	Breda, Netherlands	26 MJ/day	2400		1996/1997	[50]
Single family home	1 tank, V=5.5	Cylindrical, H=3.15 m, d=2.74 m, prefab concrete with 18 cm of enhanced polystyrene foam insulation+foil liner +heat exchanger inside tank	Simulation					[15]

Appendix B

Timestep and Grid Independence Tests for Chapter 3

Appendix B presents the timestep and grid independence test for the simulations in Chapter 3 in the form of temperature profiles. As can be seen in all graphs in this chapter, the coarse and fine mesh solutions, or the coarse and fine timestep solutions overlap. This indicates that all simulations are both timestep and grid independent.

B.1 Steady State Heat Transfer through Hollow Steel Rod

The maximum error between the CFD and analytical solution originally was 0.070%. In the grid independence test, it dropped to 0.048%, however this is not a significant

increase in accuracy, which indicates the coarse mesh is sufficient. As this simulation was run at steady state, there is only a grid independence test, which can be seen in Figure B.2.

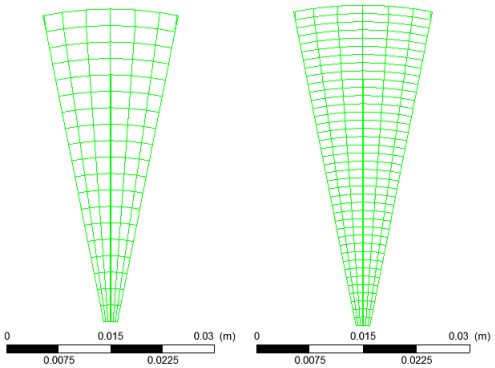

Figure B.1: Coarse mesh (left) with 20 nodes in radial direction and fine mesh (right) with 40 nodes in the radial direction

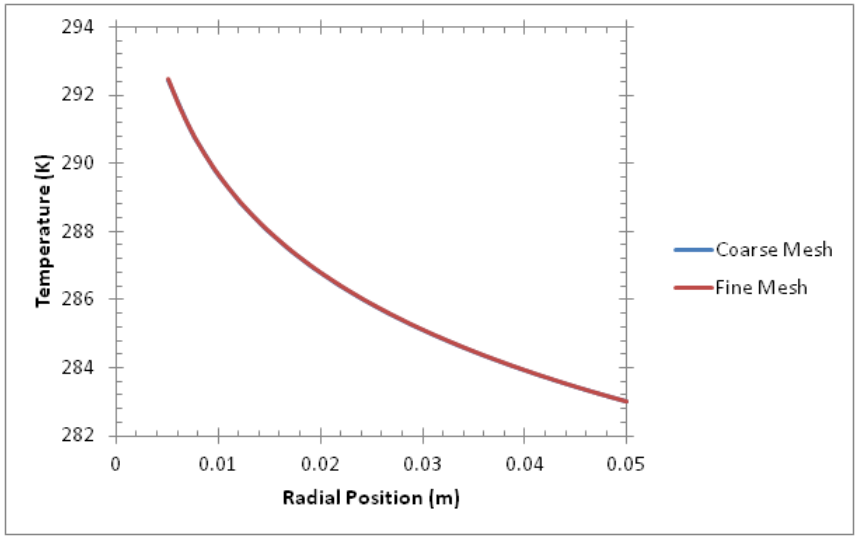

Figure B.2: Grid independence test for a steady state temperature distribution in a steel wedge

B.2 Transient Semi-Infinite Steel Rod

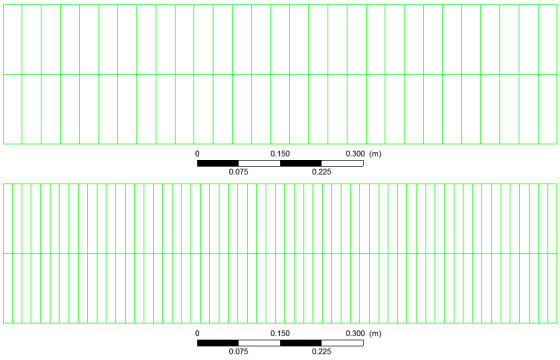

Figure B.3: Coarse mesh (top) with 30 nodes in axial direction and fine mesh (bottom) with 60 nodes in the axial direction

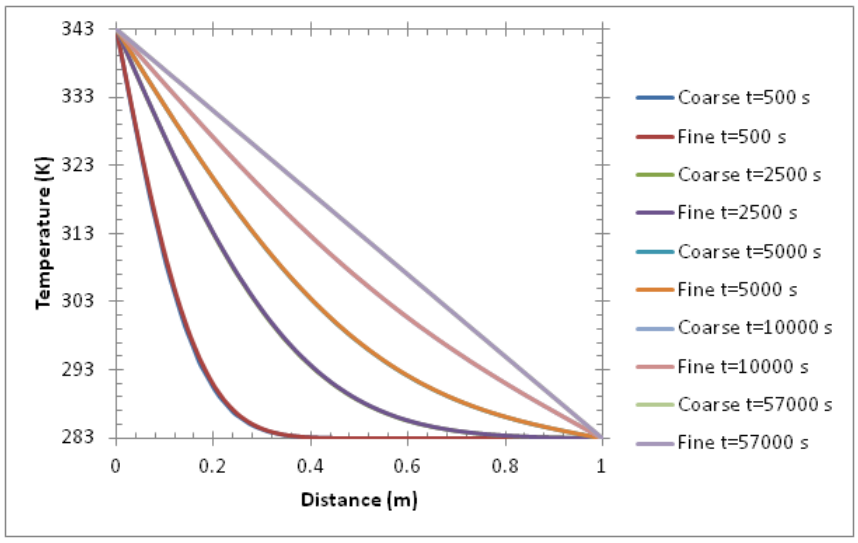

Figure B.4: Grid independence test for a transient steel rod with a semi-infinite plate solution

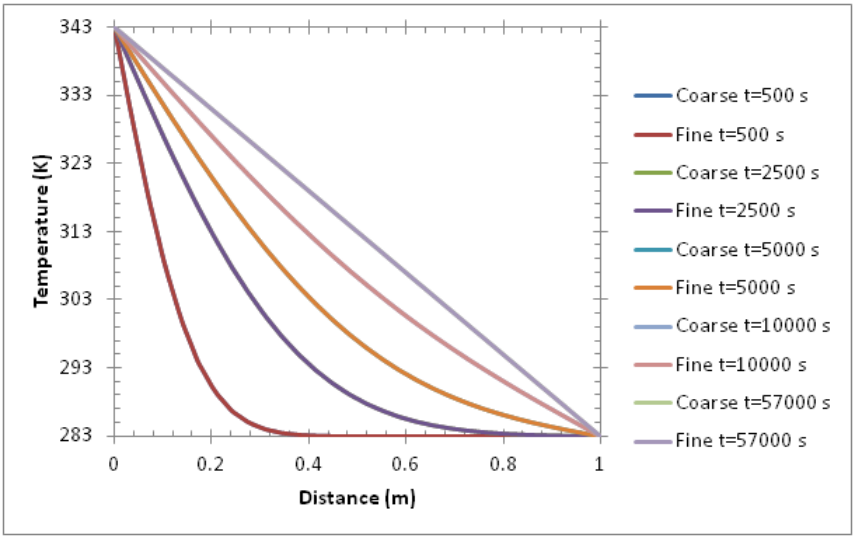

Figure B.5: Timestep independence test for a transient steel rod with a semi-infinite plate solution, where the coarse timesteps are 10 seconds and the fine 5 s.

B.3 Effect of Borehole Shape

This section presents the timestep and grid independence tests for both the square and circular boreholes.

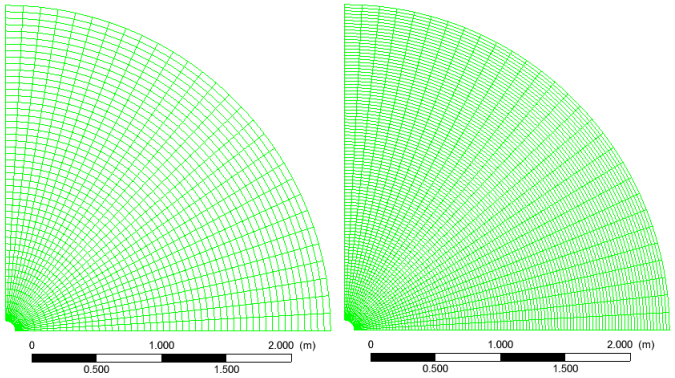

Figure B.6: Coarse mesh (left) with 50 nodes in radial direction and fine mesh (right) with 100 nodes in the radial direction

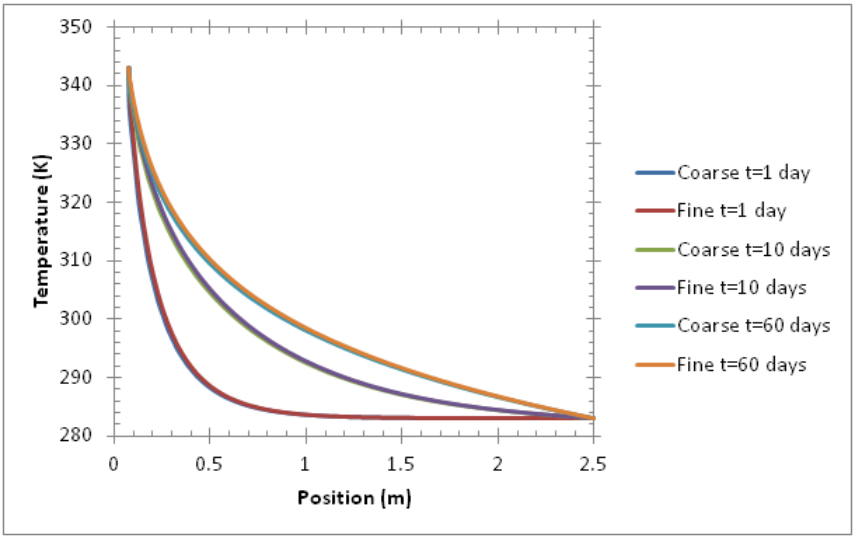

Figure B.7: Grid independence test for a circular borehole in the radial direction

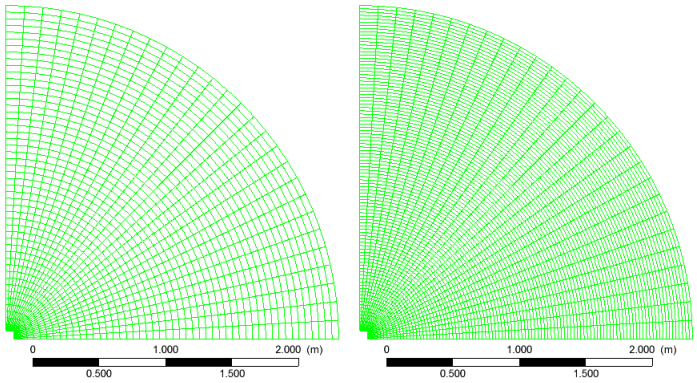

Figure B.8: Coarse mesh (left) with 50 nodes in radial direction and fine mesh (right) with 100 nodes in the radial direction

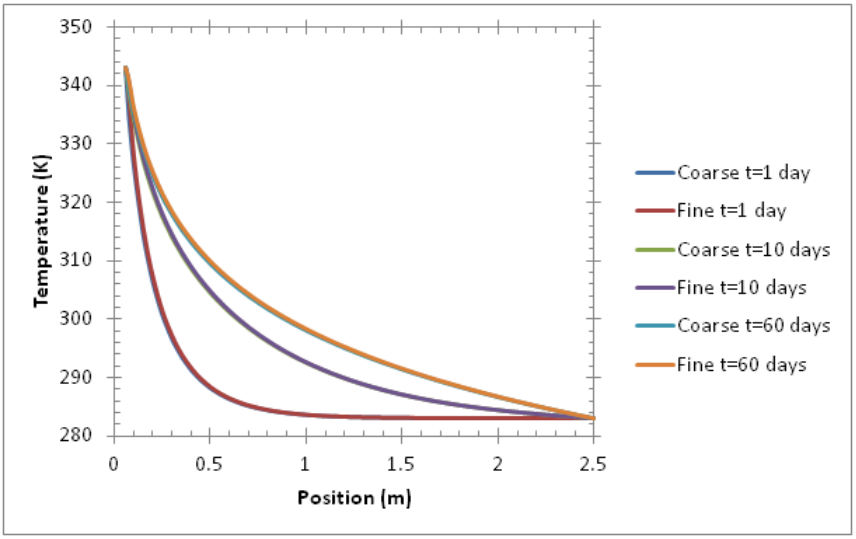

Figure B.9: Grid independence test for a square borehole in the vertical direction

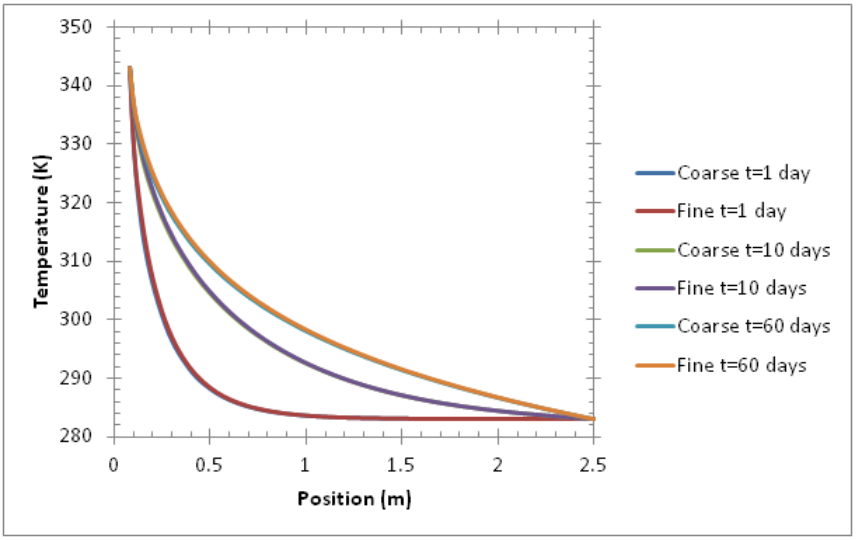

Figure B.10: Grid independence test for a square borehole in the diagonal direction

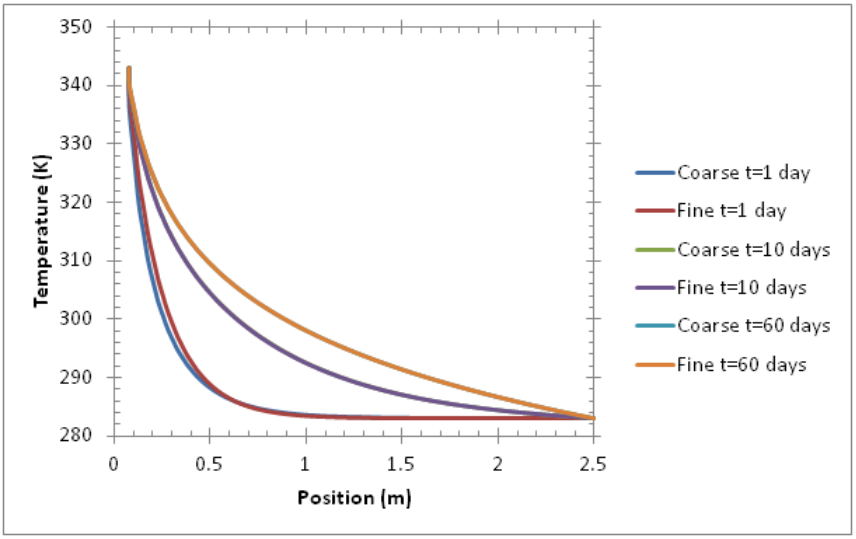

Figure B.11: Timestep independence test for a circular borehole in the radial direction, where the coarse timesteps are 24 hours and the fine 12 hours

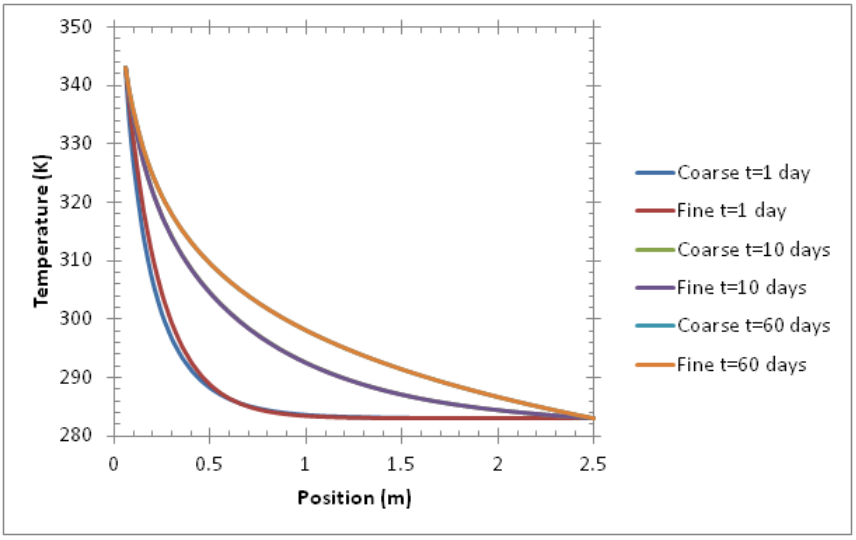

Figure B.12: Timestep independence test for a square borehole in the vertical direction, where the coarse timesteps are 24 hours and the fine 12 hours

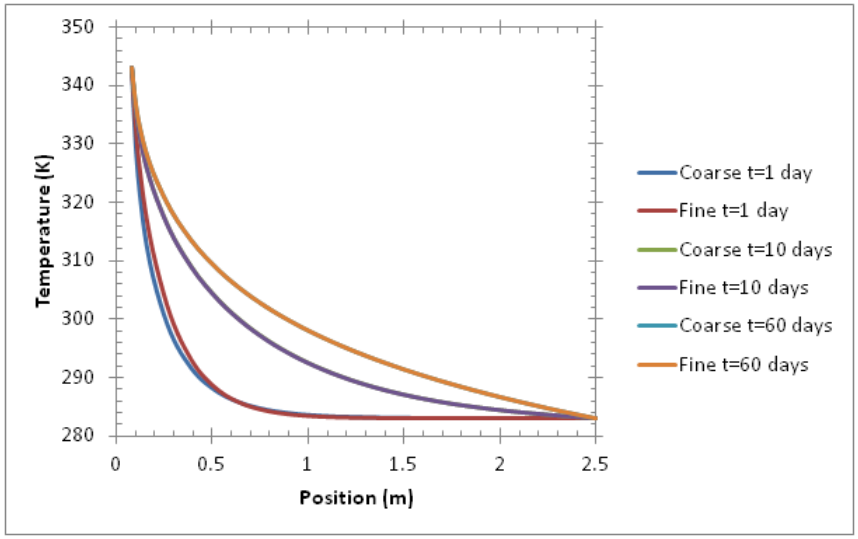

Figure B.13: Timestep independence test for a square borehole in the diagonal direction, where the coarse timesteps are 24 hours and the fine 12 hours

B.4 Effect of Tank & Domain Shape

This section presents the timestep and grid independence tests for the circular tank in a circular domain, the square tank within the circular domain, and the square tank within the square domain. Note that while an orthogonal mesh could have been selected for Figure B.19, a radial mesh was used instead in order to ensure the meshes were similar for all three cases.

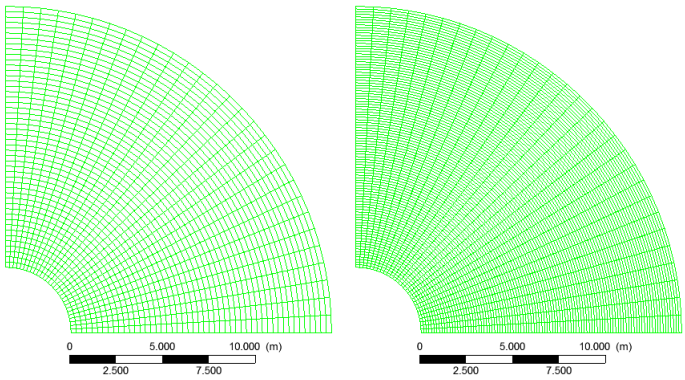

Figure B.14: Coarse mesh (left) with 50 nodes in radial direction and fine mesh (right) with 100 nodes in the radial direction

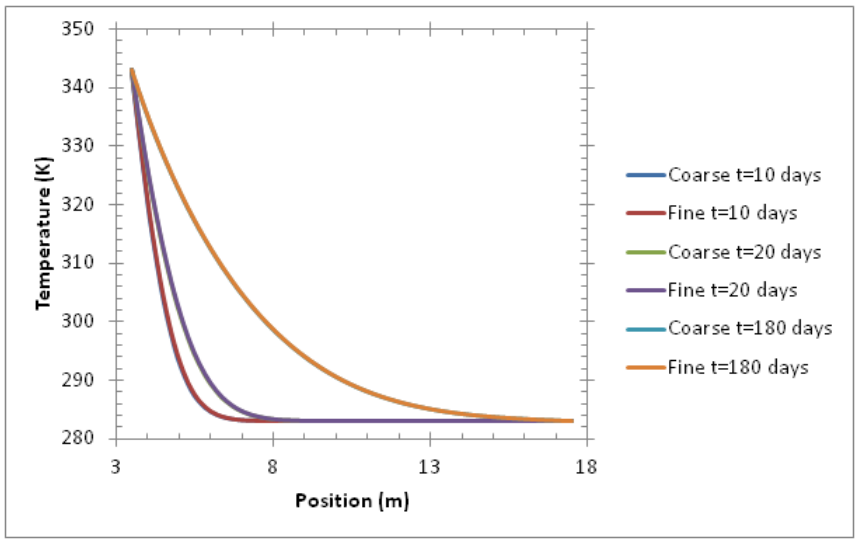

Figure B.15: Grid independence for a circular tank within a circular domain in the radial direction

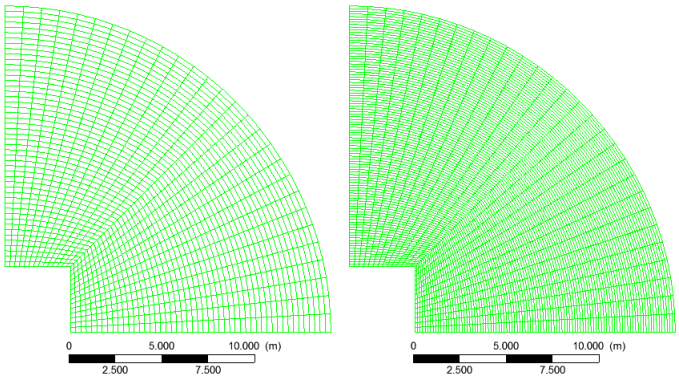

Figure B.16: Coarse mesh (left) with 50 nodes in radial direction and fine mesh (right) with 100 nodes in the radial direction

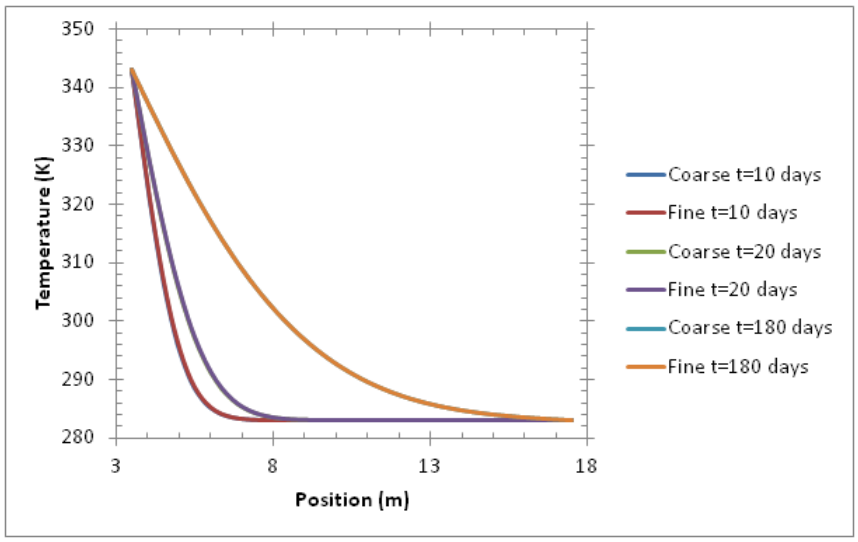

Figure B.17: Grid independence for a square tank within a circular domain in the vertical direction

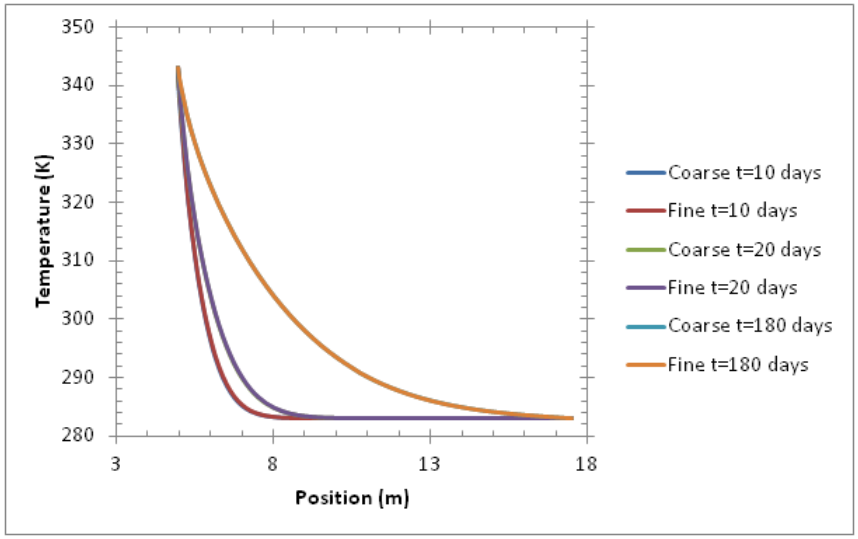

Figure B.18: Grid independence for a square tank within a circular domain in the diagonal direction

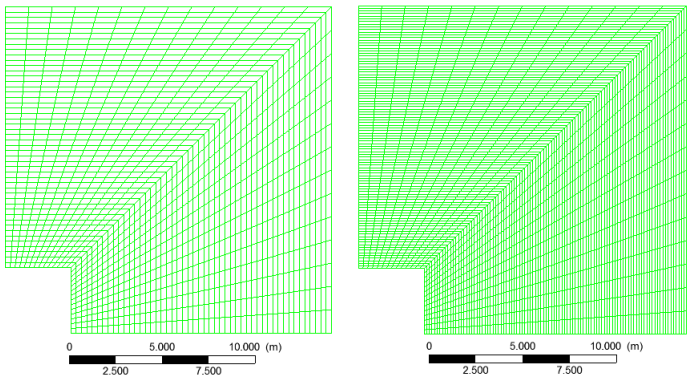

Figure B.19: Coarse mesh (left) with 50 nodes in radial direction and fine mesh (right) with 100 nodes in the radial direction

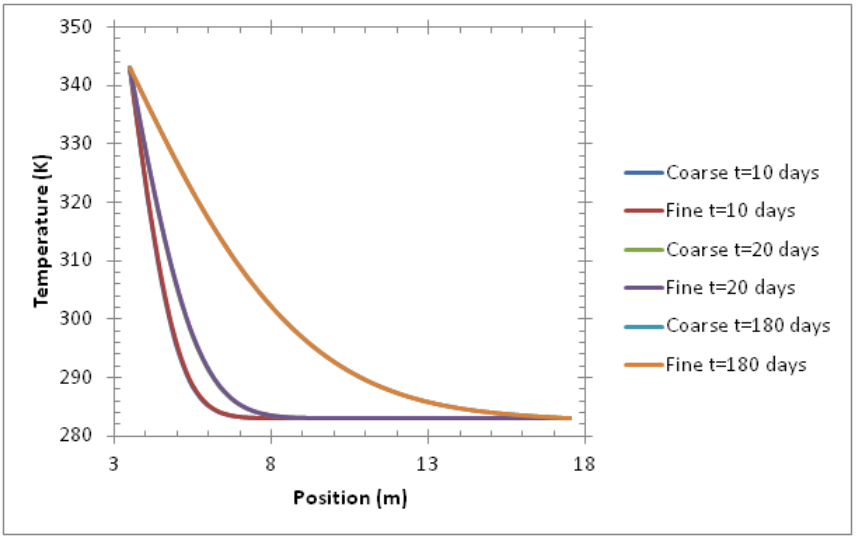

Figure B.20: Grid independence for a square tank within a square domain in the vertical direction

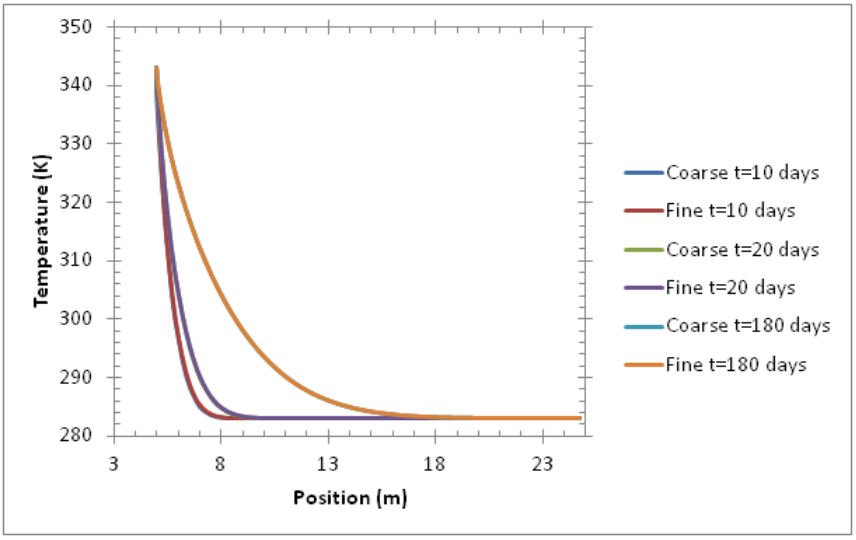

Figure B.21: Grid independence for a square tank within a square domain in the diagonal direction

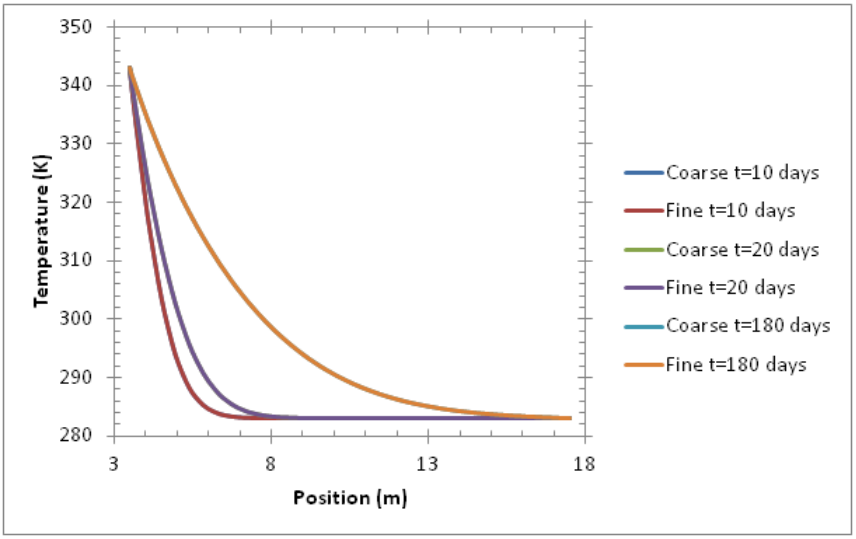

Figure B.22: Timestep independence for a circular tank within a circular domain in the radial direction, where the coarse timesteps are 24 hours and the fine 12 hours

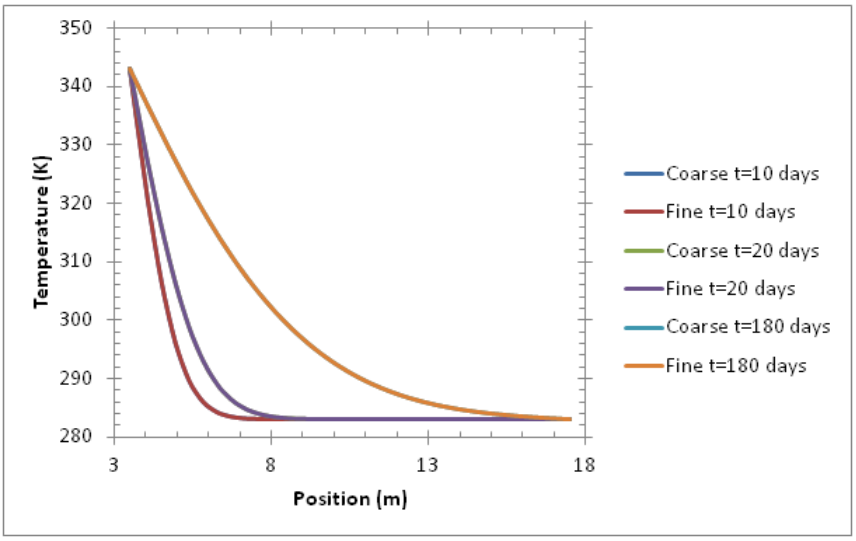

Figure B.23: Timestep independence for a square tank within a circular domain in the vertical direction, where the coarse timesteps are 24 hours and the fine 12 hours

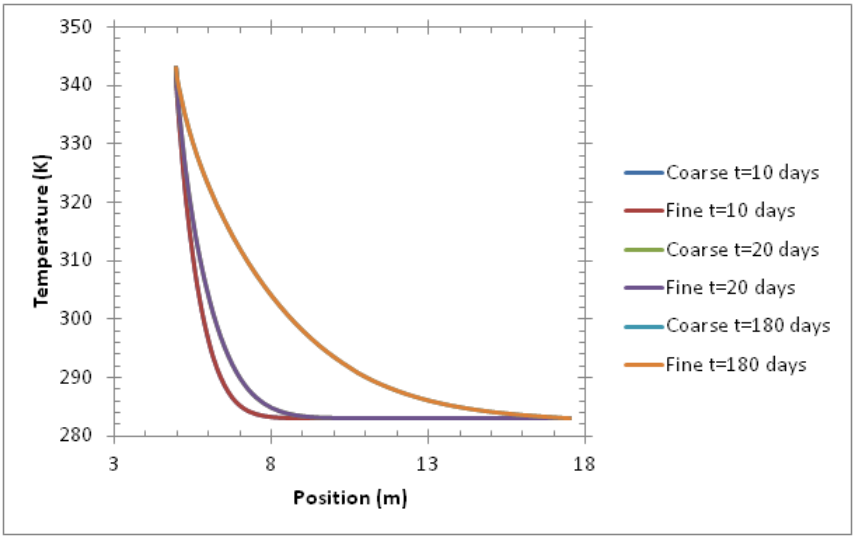

Figure B.24: Timestep independence for a square tank within a circular domain in the diagonal direction, where the coarse timesteps are 24 hours and the fine 12 hours

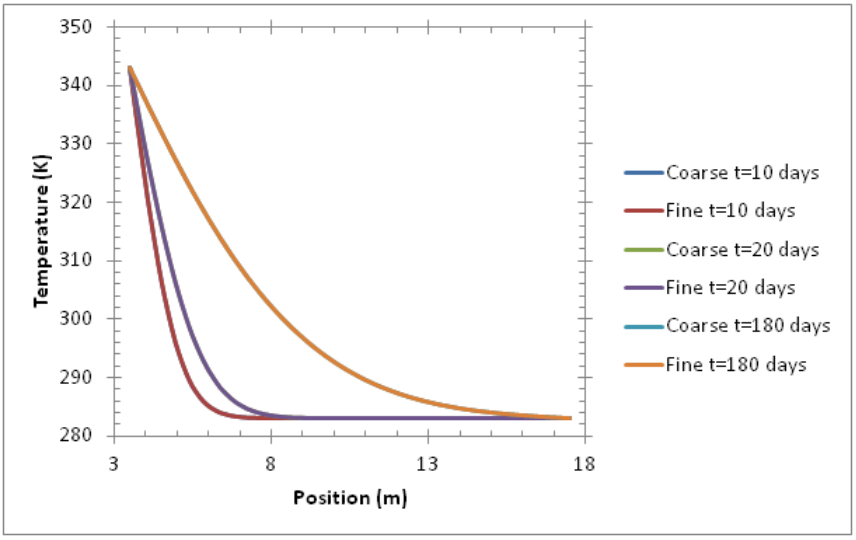

Figure B.25: Timestep independence for a square tank within a square domain in the vertical direction, where the coarse timesteps are 24 hours and the fine 12 hours

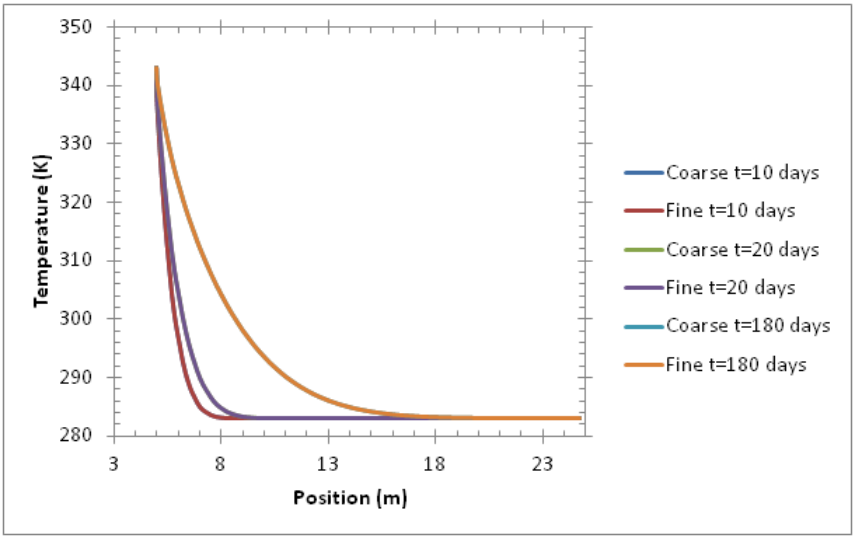

Figure B.26: Timestep independence for a square tank within a square domain in the diagonal direction, where the coarse timesteps are 24 hours and the fine 12 hours

B.5 Effect of Domain Size

This section presents the grid and timestep independence test for the different domain sizes. Note that while geometry presented in Figures B.19 and B.27 is the same, the mesh has been changed to an orthogonal mesh which removes the skewed cells and improves mesh quality.

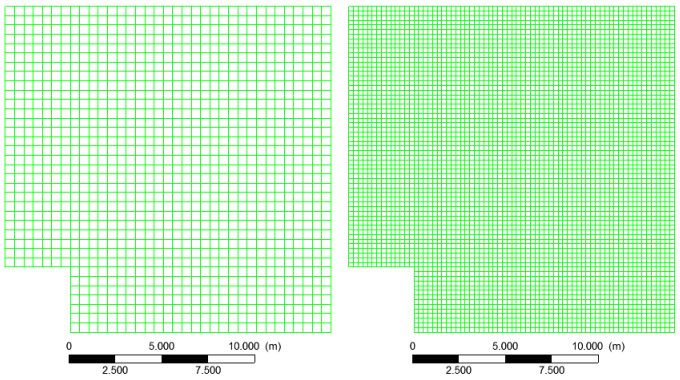

Figure B.27: Coarse mesh (left) with 35 nodes along each edge and fine mesh (right) with 70 nodes along each edge

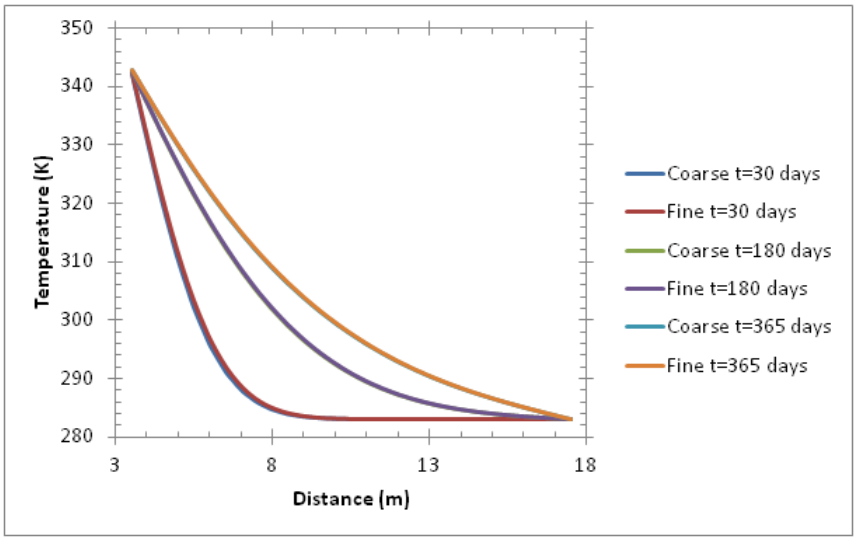

Figure B.28: Grid independence for the small (17.5 by 17.5 m) domain

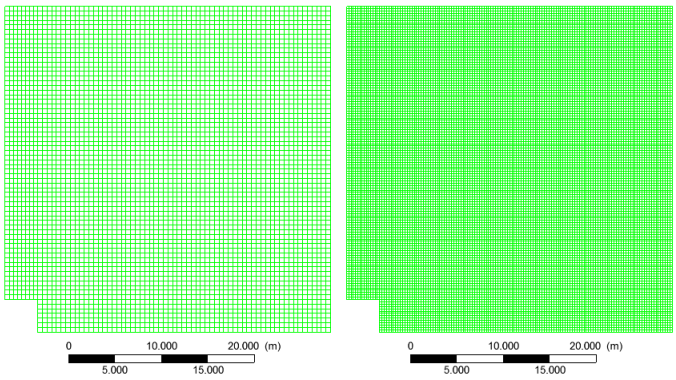

Figure B.29: Coarse mesh (left) with 70 nodes along each edge and fine mesh (right) with 140 nodes along each edge

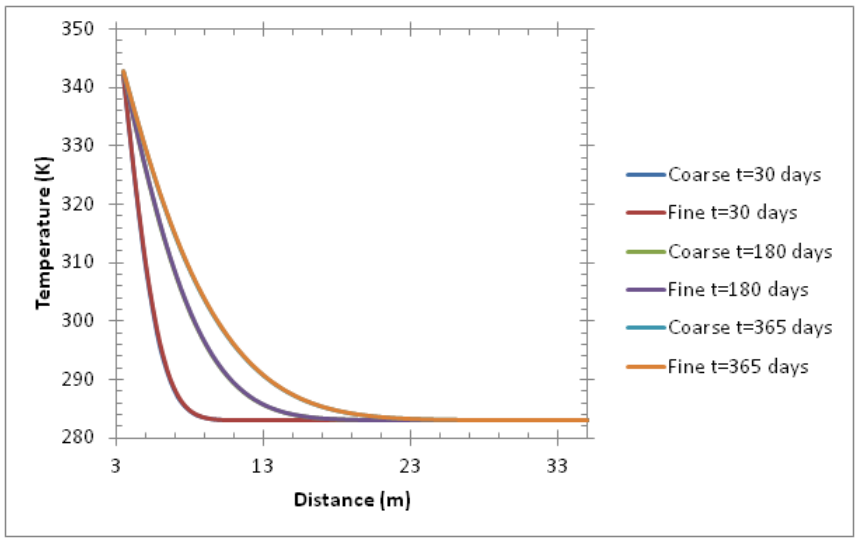

Figure B.30: Grid independence for the large (35 by 35 m) domain

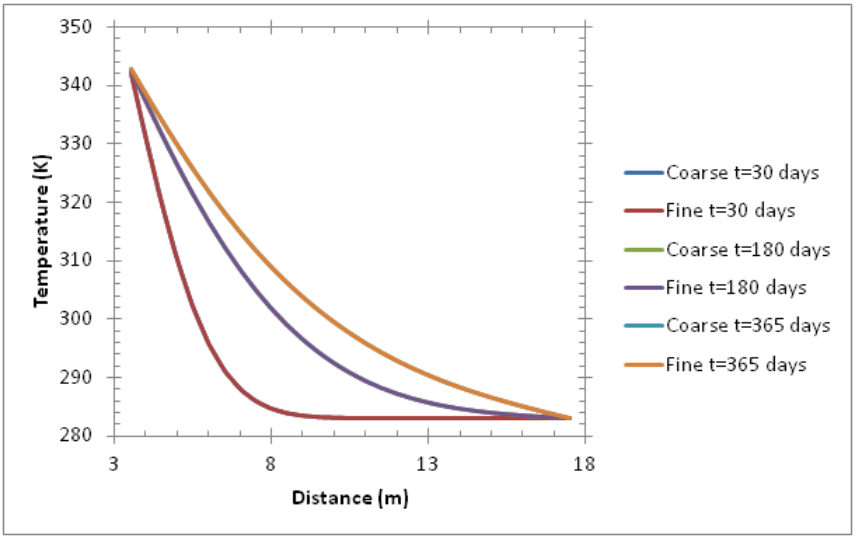

Figure B.31: Timestep independence for the small (17.5 by 17.5 m) domain, where the coarse timesteps are 24 hours and the fine 12 hours

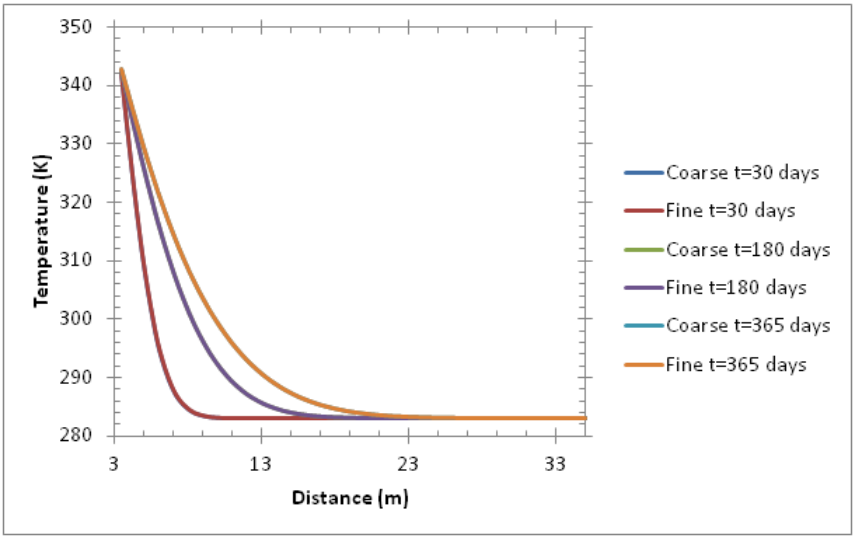

Figure B.32: Timestep independence for the large (35 by 35 m) domain, where the coarse timesteps are 24 hours and the fine 12 hours

B.6 Superposition of Two Rods

All three simulations in this case share the same geometry and mesh, which can been seen in Figure B.33.

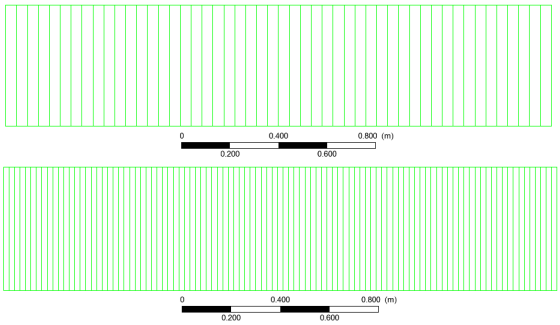

Figure B.33: Coarse mesh (left) with 51 nodes in the axial direction and fine mesh (right) with 102 nodes in the axial direction

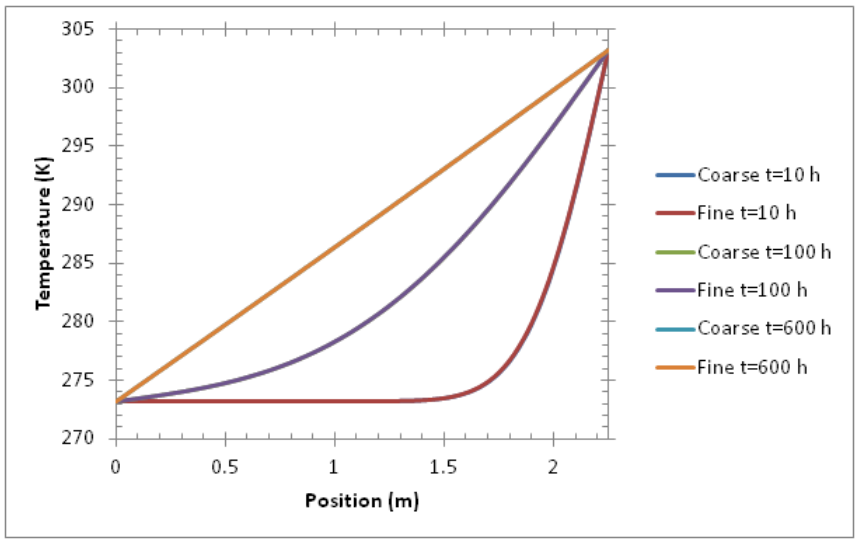

Figure B.34: Grid independence for the hot rod

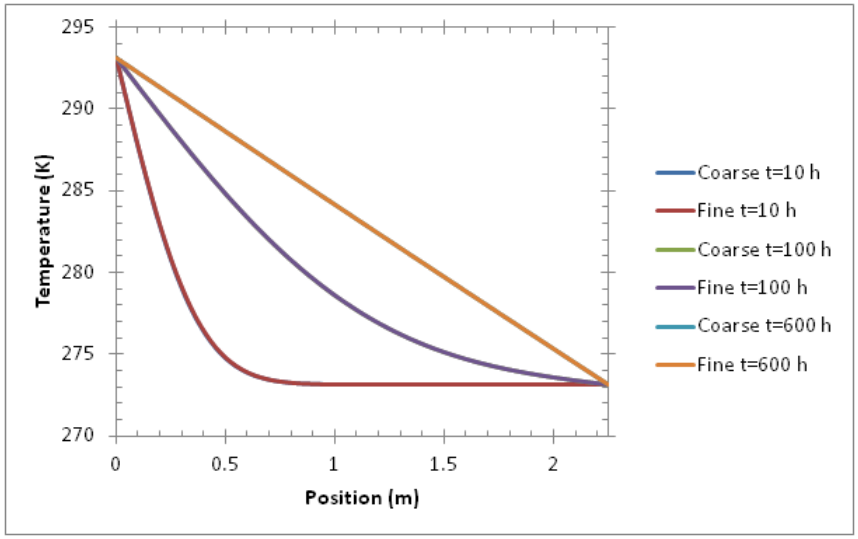

Figure B.35: Grid independence for the cold rod

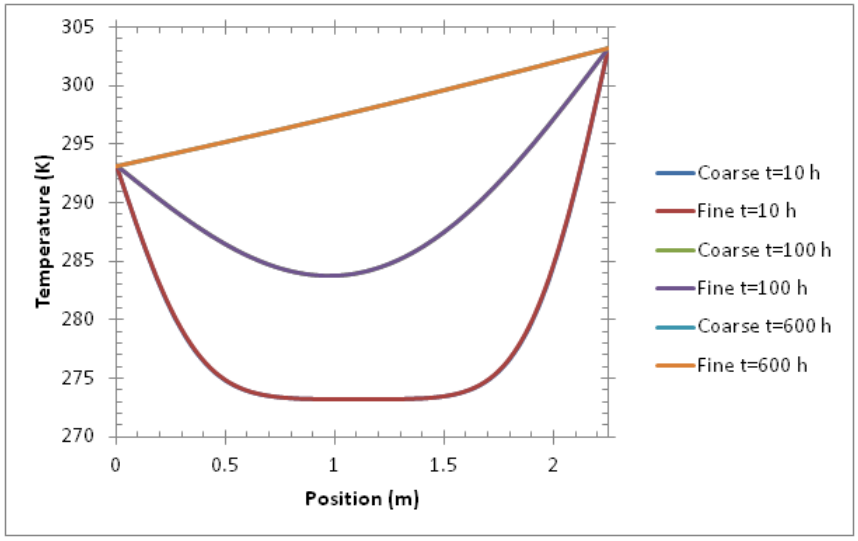

Figure B.36: Grid independence for the hot and cold rod

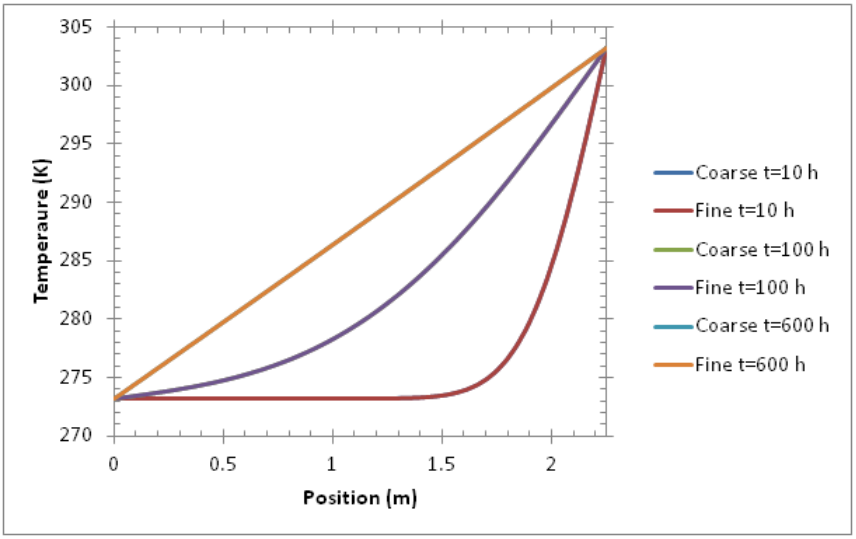

Figure B.37: Timestep independence for the hot rod, where the coarse timesteps are 15 minutes and the fine 30 minutes

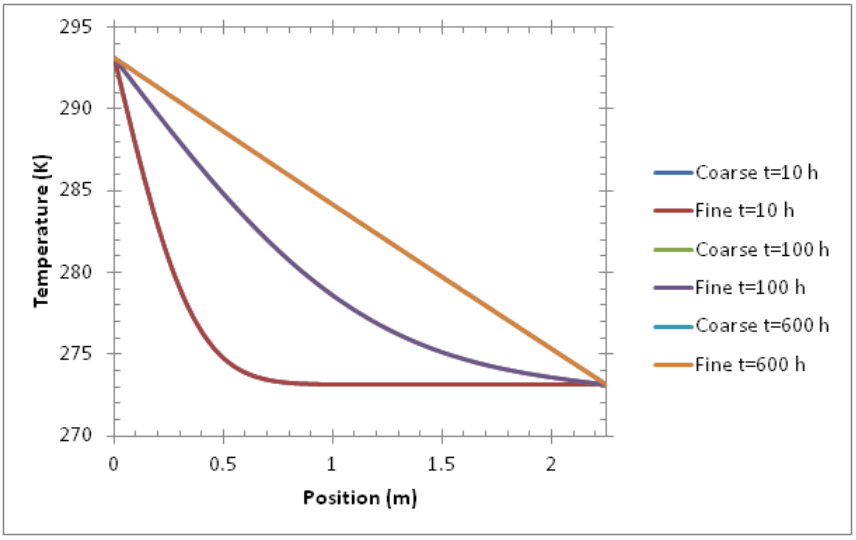

Figure B.38: Timestep independence for the cold rod, where the coarse timesteps are 15 minutes and the fine 30 minutes

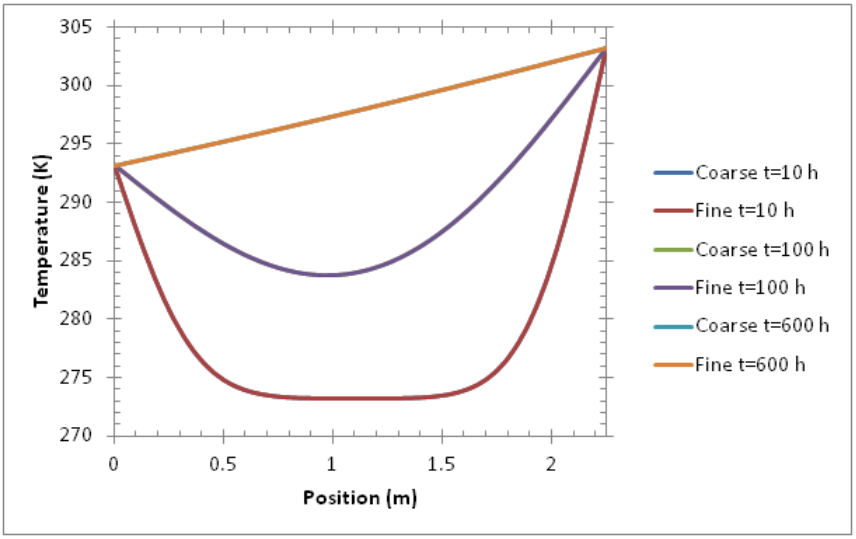

Figure B.39: Timestep independence for the hot and cold rod, where the coarse timesteps are 15 minutes and the fine 30 minutes

B.7 Superposition of Two Boreholes in a Large Domain

For the superposition of two boreholes, the grid was refined considerably to become grid independent. As it is difficult to visualize, the fine meshes in Figures B.40 and B.42 had the number of nodes doubled in the horizontal direction.

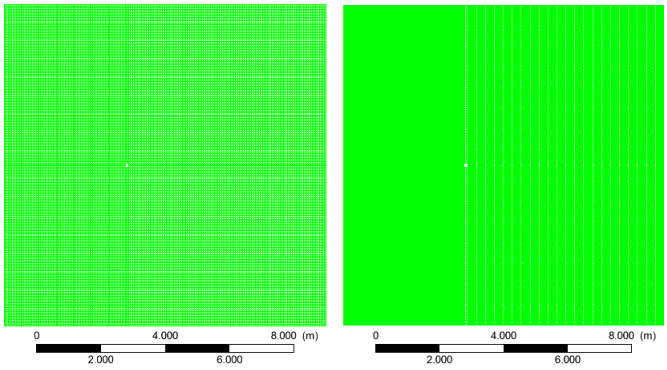

Figure B.40: Coarse mesh (left) with 192 nodes along both the horizontal and vertical edges and fine mesh (right) with 430 nodes along the horizontal edge and 192 nodes along the vertical

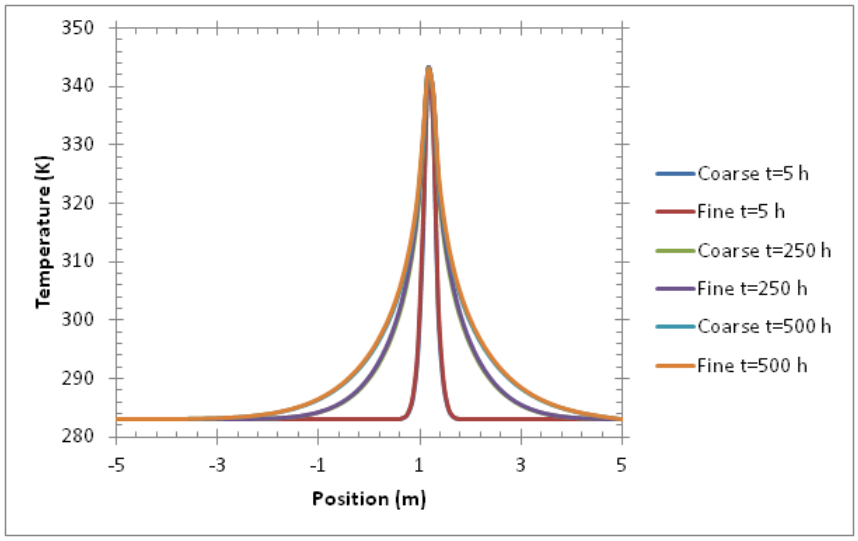

Figure B.41: Grid independence of a single borehole

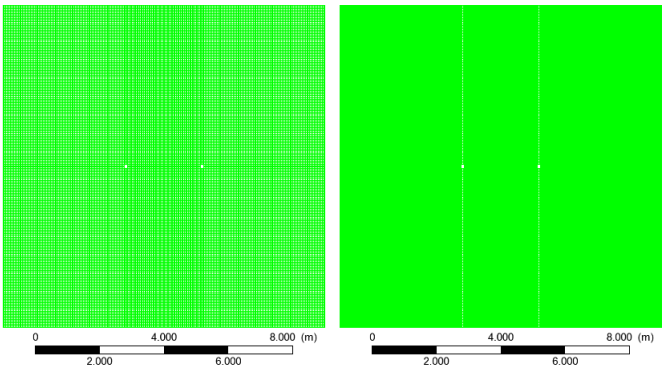

Figure B.42: Coarse mesh (left) with 192 nodes along both the horizontal and vertical edges and fine mesh (right) with 430 nodes along the horizontal edge and 192 nodes along the vertical

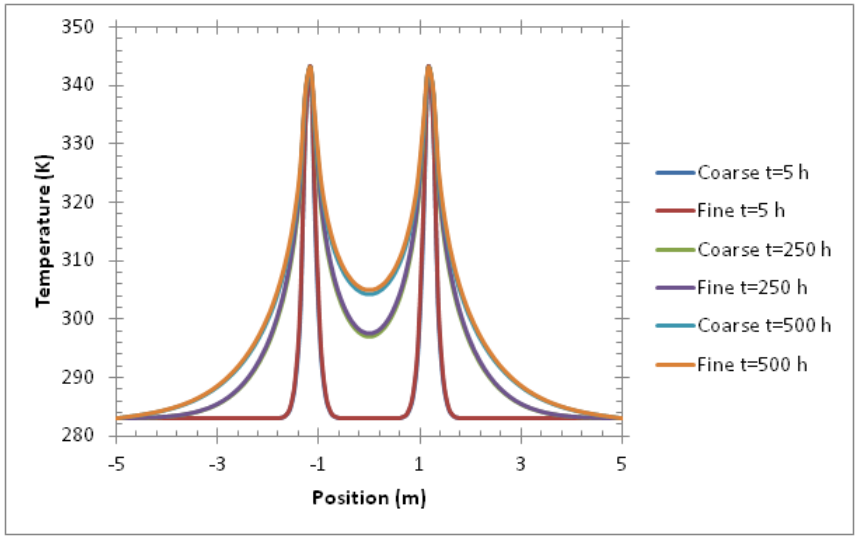

Figure B.43: Grid independence of two boreholes

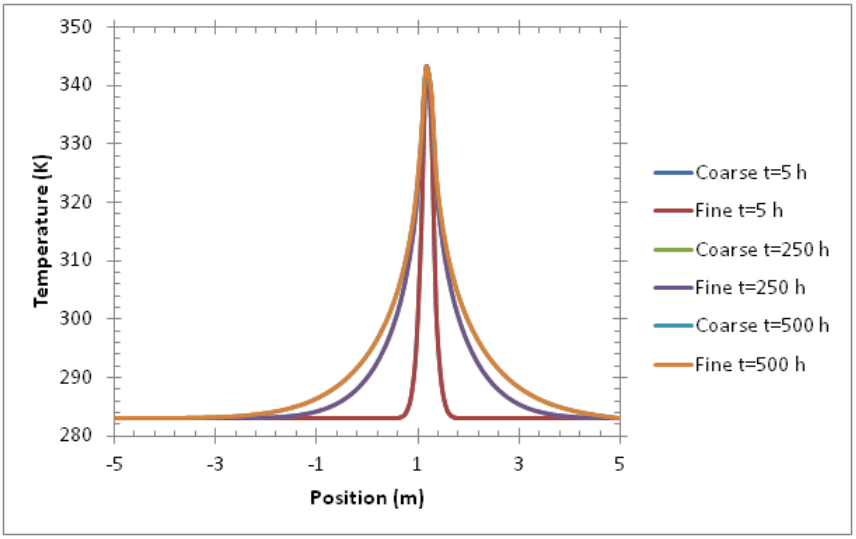

Figure B.44: Timestep independence of a single borehole, where the coarse timesteps are 15 minutes and the fine 30 minutes

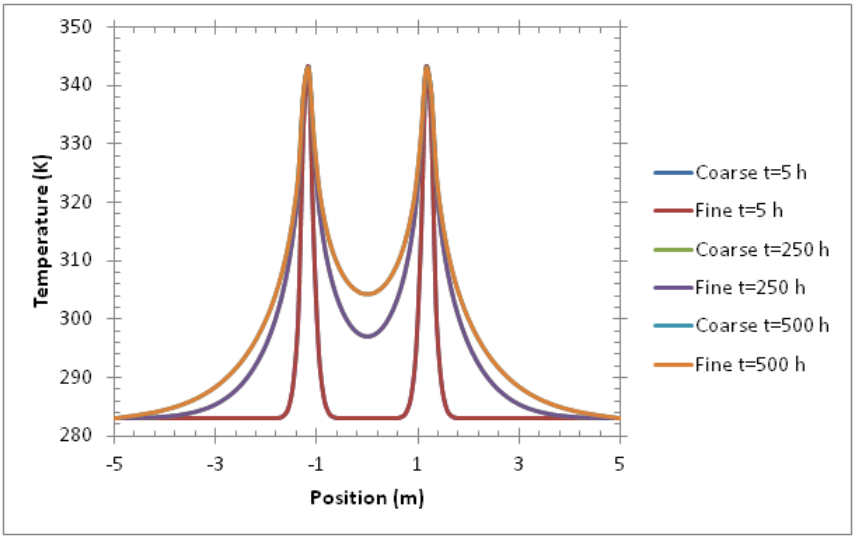

Figure B.45: Timestep independence of two boreholes, where the coarse timesteps are 15 minutes and the fine 30 minutes

B.8 Verification of Borehole Transient Temperature Profile

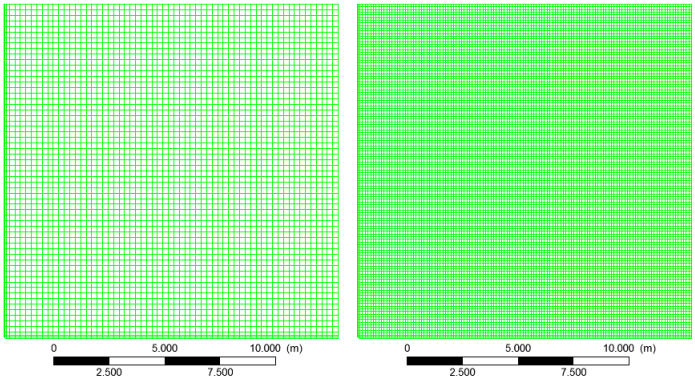

Figure B.46: Coarse mesh (left) with 65 nodes along each edge and fine mesh (right) with 130 nodes along each edge

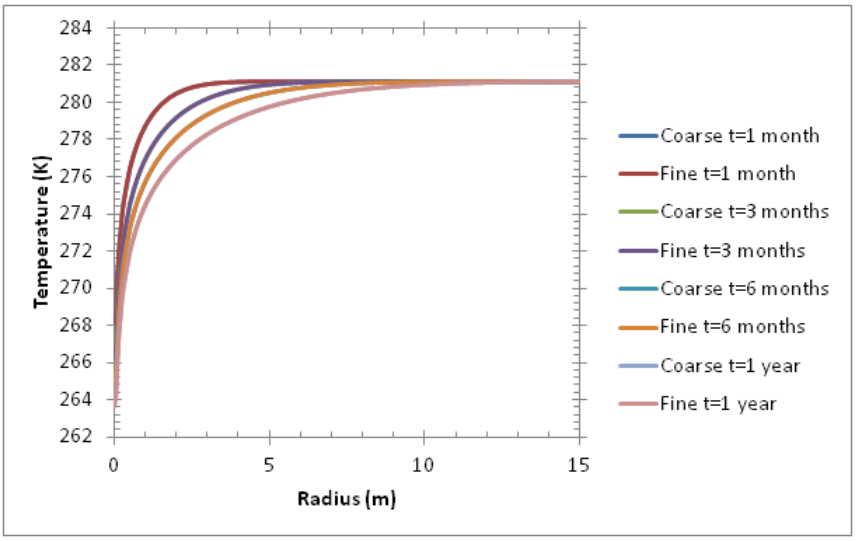

Figure B.47: Grid independence of verification simulation

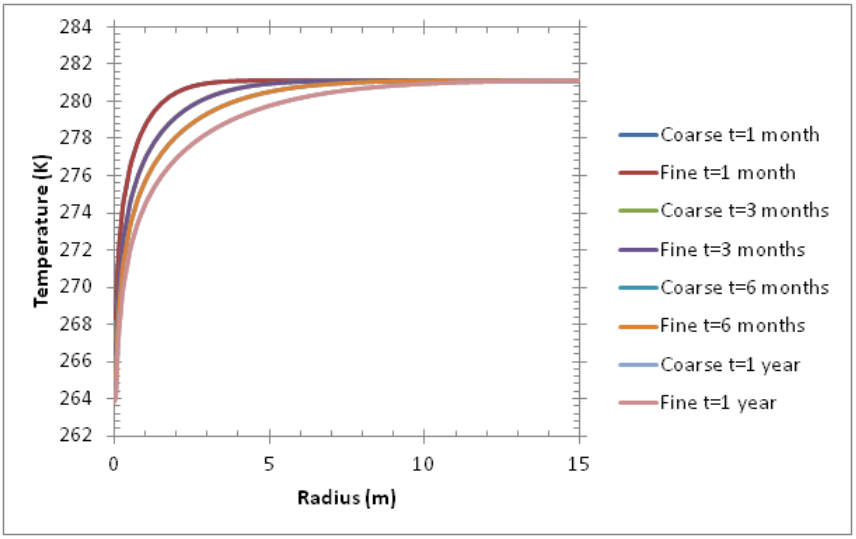

Figure B.48: Timestep independence of verification simulation, where the coarse timesteps are 24 hours and the fine 12 hours

Appendix C

Boundary Condition Selection for Chapter 4

Appendix C details the selection of the boundary conditions for the base case, more specifically, the process used to select the top and bottom boundaries.

C.1 Top Boundary Condition: Heat Transfer Coefficient Calculations

In order to calculate the heat transfer coefficient, we first need to determine the Reynolds number. At a temperature of 10°C, which is the average temperature between the summer and winter conditions, the properties of air are ρ=1.246 kg/m^3, μ=1.778$\times$ 10^{-5} kg/m·s, Pr$_{air}$=0.7336 and k=0.02439 W/m·K. The length in Reynolds

number was taken as 17.5 m which is the distance across the boreholes. The average wind speed for Calgary is around 15 km/h [51] which is 4.17 m/s.

$$Re_L = \frac{\rho v L}{\mu} \tag{C.1}$$

$$Re_L = \frac{1.246 \times 4.17 \times 17.5}{1.778 \times 10^{-}5} = 5113996 \tag{C.2}$$

This determines that the flow is turbulent. Even a mild breeze of 5 km/h will yield a turbulent flow. From Cengel [36], the correlation for the Nuesselt number for flow over a flat plate is as follows:

$$Nu = \frac{hL}{k} = 0.037 Re_L^{0.8} Pr^{1/3} \tag{C.3}$$

Re-arranging and substituting yields h=10.83 W/m^{2}K. Solving again for temperatures of 20°C and -10°C gives h=11.147 W/m^{2}K and 10.181 W/m^{2}K respectively which indicates that h does not vary significantly with temperature.

In order to add in the effect of insulation, an effective heat transfer coefficient must be calculated. For this, a thermal resistance diagram was drawn, as seen in Figure C.1.

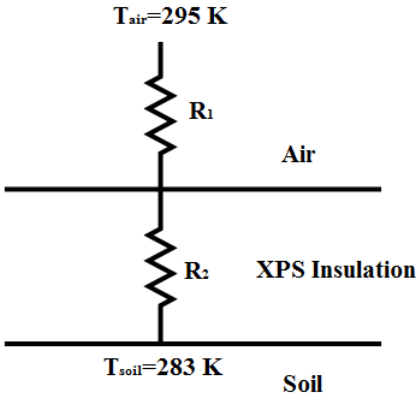

Figure C.1: Resistance diagram of the insulation on top of the borehole field

$$\dot{Q} = \frac{T_i - T_\infty}{R_1 + R_2} \tag{C.4}$$

$$R_1 = \frac{1}{h_1 \times A} \tag{C.5}$$

$$R_2 = \frac{L_1}{k_1 \times A} \tag{C.6}$$

Where the area of the plate is the area on top of the boreholes (17.5 m by 17.5 m), L_1=200 mm, which is the thickness of insulation at DLSC, and k_1=0.035 W/m·K, which is the thermal conductivity of XPS insulation [52].

$$R_{total} = R_1 + R_2 \tag{C.7}$$

$$R_{total} = \frac{1}{h_1 \times A} + \frac{L_1}{k_1 \times A} \tag{C.8}$$

Substituting the appropriate values:

$$R_{total} = \frac{1}{11.147\ \frac{W}{m^2K} \times 17.5\ m \times 17.5\ m} + \frac{0.2\ m}{0.035\ \frac{W}{m \cdot K} \times 17.5\ m \times 17.5\ m} = 0.01895\ \frac{K}{W} \tag{C.9}$$

Substituting into equation C.4:

$$\dot{Q} = \frac{295\ K - 283\ K}{0.01895\ \frac{K}{W}} = 633\ W \tag{C.10}$$

To determine the new heat transfer coefficient:

$$R_{total} = \frac{1}{h_{eff} \times A} \tag{C.11}$$

$$h_{\text{eff}} = \frac{1}{0.01895\ \frac{K}{W} \times 17.5\ m \times 17.5\ m} = 0.1723\ W/m^2K \tag{C.12}$$

This value, along with the ambient air temperature were used in order to specify the boundary condition on the top surface.

C.2 Bottom Boundary Condition

The impact of the bottom boundary condition was investigated by checking the location as well as the difference between a set temperature and a set heat flux.

C.2.1 Bottom Boundary Location

The bottom boundary was originally set to be 5 m below the bottom of the boreholes. However, in order to determine if this boundary is far enough away as to not impact the solution, it was moved to 2.5 m and 15 m below the bottom of the boreholes.

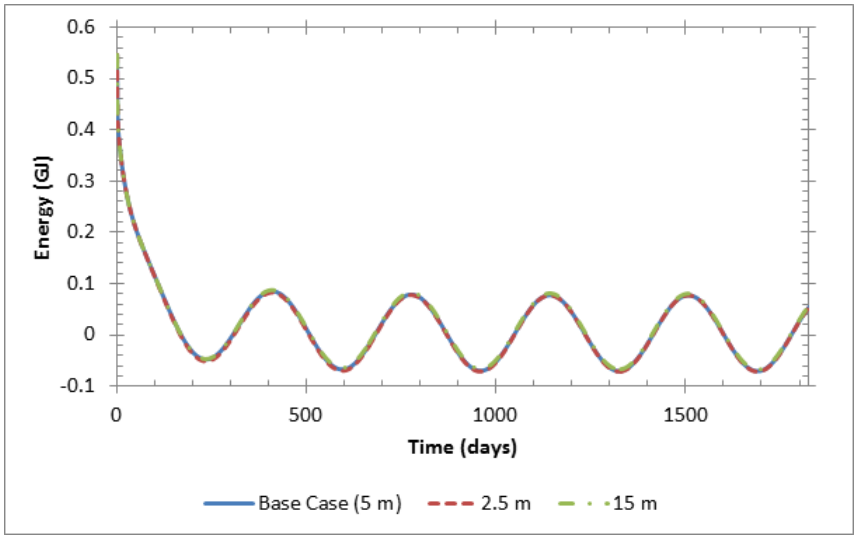

Figure C.2: Impact of the location of the bottom boundary at 5, 2.5 and 15 m below the bottom of the boreholes on borehole energy injection and extraction

Figure C.2 presents the energy injected and extracted by one borehole. It can be observed that the difference in performance is minimal. The tank and all other boreholes show a similar performance.

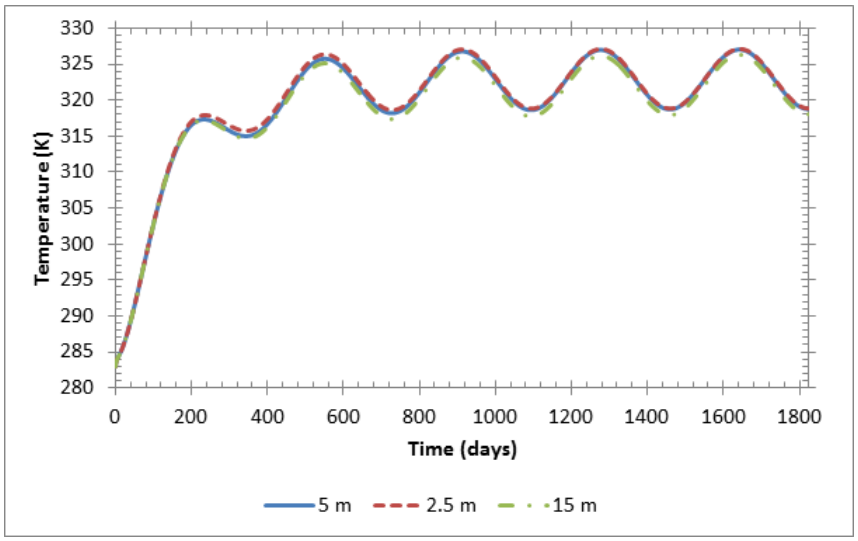

Figure C.3: Impact of the location of the bottom boundary at 5, 2.5 and 15 m below the bottom of the boreholes on the soil plug temperature

While both the base case and the 2.5 m cases ran in roughly the same amount of time, the 15 m case took about 25% longer to run due to the additional computational expense. All three simulations had approximately the heat flux profiles for the tank and boreholes. The 5 m case was selected over the 2.5 m case as it accumulated less heat under the boreholes. This was not an issue for the current energy injection rate, but for the cases that had higher temperatures set at the boreholes, there is a reduced possibility that the bottom boundary may interact with the solution.

C.2.2 Impact of a Set Heat Flux Compared to a Set Temperature

The simulations tested the impact of the type of the bottom boundary condition while keeping all other boundaries the same as those described in the base case. The one difference was that the bottom boundary was located 15 m below the bottom

of the boreholes as opposed to 5 m in the base case. The bottom boundary initially had a boundary condition of T=283 K, which is the far field temperature (the same boundary condition as the two vertical sides). However, further research suggested a heat flux would be a more appropriate choice. As such, the boundary condition was changed to q"=0.058 W/m^2 entering the domain [38]. This did not result in a significant change in performance of the borehole field.

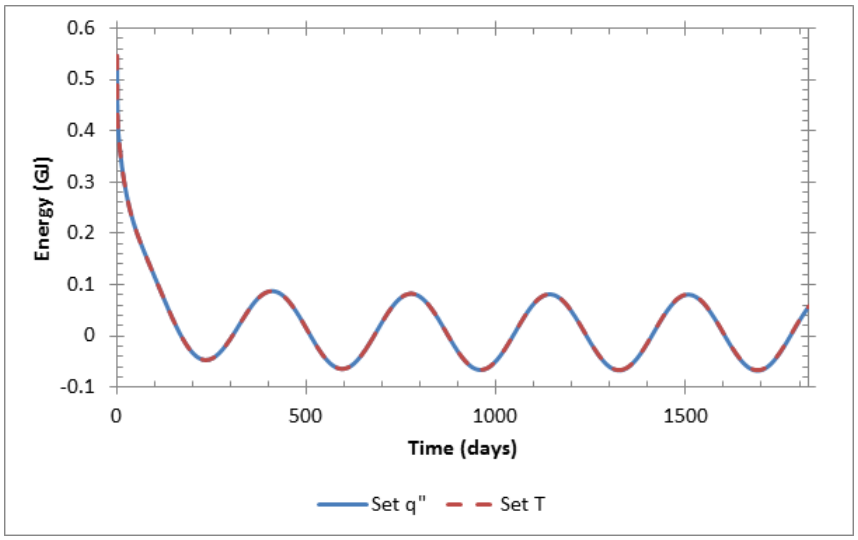

Figure C.4: Impact of a set temperature compared to a set heat flux for the bottom boundary condition on borehole energy injection and extraction

Figure C.4 depicts the energy injected and extracted from one borehole and similarly to the previous case, there is little difference between the set temperature and set heat fluxes cases.

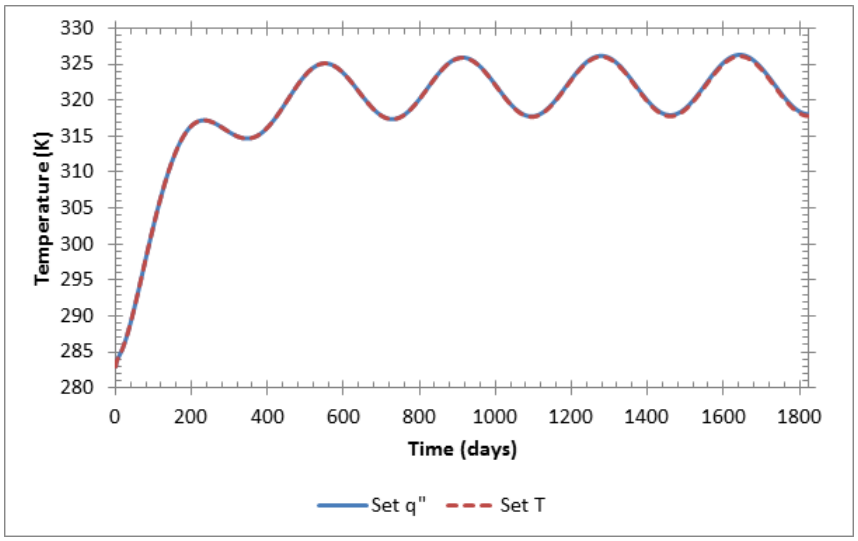

Figure C.5: Impact of a set temperature compared to a set heat flux for the bottom boundary condition on soil plug temperature

The soil plug temperature can been seen in Figure C.5, and it also does not show any difference between the simulations. As such, it was concluded that either boundary condition is acceptable, however, the heat flux condition better represents the physical phenomenon, so it was selected as the more accurate condition.

Appendix D

Residual Check

The residual check was performed on a geometry with a tank and one ring of boreholes set to T_bh=343 K and all other boundary conditions the same as the Base Case. It had results checked at 7, 14 and 30 days which is when the gradients are highest for the six month initial charge from the undisturbed ground temperature of 283 K. Presented in Figure D.1 below is a temperature profile in the horizontal direction. As can be seen in the figure, there is negligible difference between the three cases. However, there is a larger difference between the 10^{-4} and 10^{-5} cases than the 10^{-5} and 10^{-6} cases. The 10^{-4} took 58 seconds, the 10^{-5} 1:20 minutes and the 10^{-6} took 2:30 minutes. There is a larger difference in computational time for the 10^{-6} compared to 10^{-5}, and while the difference may be small here, as the domain and run time increases, this will amount to a much larger time difference so 10^{-5} was chosen as the residual.

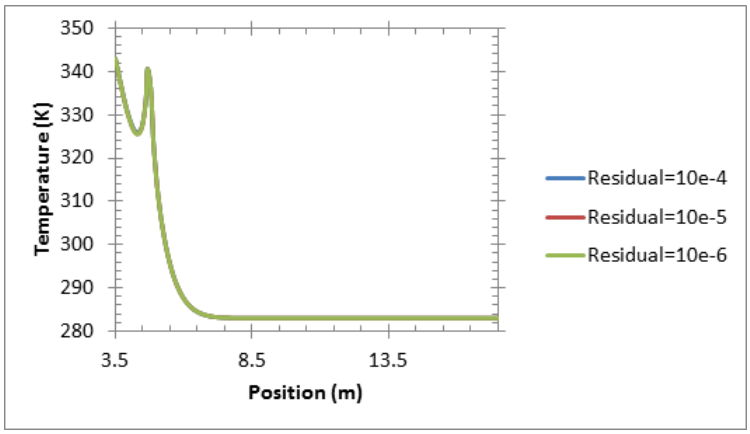

Figure D.1: Horizontal temperature profile at y=-6 m at t=7 days